ABSTRACT

Title of Document: PLASMA ETCHING OF DIELECTIRC MATERIALS USING INDUCTIVELY AND CAPACITIVELY COUPLED FLUOROCARBON DISCHARGES: MECHANISTIC STUDIES OF THE SURFACE CHEMISTRY

Li Ling, Doctor of Philosophy, 2006

Directed By: Professor Gottlieb S. Oehrlein, Department of Material Science and Engineering

Fluorocarbon (FC) plasmas are commonly used for dielectric materials etching. Our initial work was performed using an inductively coupled plasma (ICP) system to produce FC discharges. We first examined the effect of CO addition to C_4F_8 or C_4F_8/Ar plasmas for selective etching of organosilicate glass (OSG), which is a typical low k (LK) material over etch stop layers. The chemical activity of CO when added to either C_4F_8 or C_4F_8/80% Ar can be understood in terms of the CO dissociation energy threshold relative to energies of inelastic electron collision processes of the dominant feedgas component. We also studied the plasma etching behavior of 193 nm and 248 nm photoresist in FC discharges used for dielectric

etching. We showed that ion-enhanced selective volatilization of carbonyl groups of the 193 nm photoresist polymer backbone which is absent for the 248 nm material, along with modulation of the ion-interaction with the photoresist material by fluorocarbon surface passivation, may be responsible for the introduction of pronounced surface roughness of 193 nm photoresists.

Current industrial efforts are aimed primarily at capacitively coupled plasma (CCP) systems. A home-built dual frequency CCP reactor was used to investigate additional aspects of dielectric materials plasma etching. We designed a gap structure to simulate sidewall surface processes occurring during high aspect ratio trench etching. In particular, we showed that the FC film deposition rates measured using the gap structure qualitatively correlate with the trench sidewall angles produced in LK dielectrics in both C_4F_8/Ar and CF_4/H_2 based gas chemistries: The lower the FC deposition rate on the sidewall, the more vertical the trench sidewall. This approach was used to study surface chemistry aspects of FC film deposition with and without ion bombardment. For the gap structure film deposition takes place without ion bombardment and we observed a novel FC film growth phenomenon in pure C_4F_8 plasmas at high pressure: Two distinct chemical surface portions were shown to exist simultaneously, one consisting primarily of C-F_2 and C-F_3 bonding, and the other of C-C/C-H bonding. An explanation consistent with all of our data is localized CF_2 attachment to growing FC chains.

PLASMA ETCHING OF DIELECTIRC MATERIALS USING INDUCTIVELY AND CAPACITIVELY COUPLED FLUOROCARBON DISCHARGES: MECHANISTIC STUDIES OF THE SURFACE CHEMISTRY

By

Li Ling

Dissertation submitted to the Faculty of the Graduate School of the
University of Maryland, College Park, in partial fulfillment
of the requirements for the degree of
Doctor of Philosophy
2006

Advisory Committee:
Professor Gottlieb S. Oehrlein, Chair
Professor Gary W. Rubloff
Professor Ichiro Takeuchi
Professor Jon Orloff
Professor John Melngailis

Acknowledgements

I would like to begin my thanking by thesis advisor, Professor Gottlieb S. Oehrlein, who introduced me to the exciting field of plasma etching. This research work would not have been realized without his academic and financial support over the years of my graduate study. His enthusiasm and collaborative spirit helped to create a great work environment, and his amazingly broad knowledge and experience gave my research both direction and inspiration.

I would especially like to thank all the members of my committee for their efforts on my behalf: Professor Gottlieb S. Oehrlein, Professor Gary W. Rubloff**,** Professor Ichiro Takeuchi, Professor John Melngailis and Professor Jon Orloff.

I would like to acknowledge my various research financial supports: Semiconductor Research Corporation (SRC) Center for Advanced Interconnect Science and Technology (CAIST), Department of Energy (DOE), National Science Foundation (NSF), SEMATECH and Lam Research Corporation. I would also like to acknowledge the collaboration with companies and other research groups. I thank Ping Jiang (Texas Instruments) who collaborated on scanning electron microscopy (SEM) characterizations of structures in this thesis, Paolo Lazzeri, Erica Iacob and Mariano Anderle (ITC-irst, Center for Scientific and Technological Research, Italy) for collaboration on characterization of photoresist materials using time of flight secondary ion mass spectroscopy (TOF SIMS), Louis Frees (Inficon) who contributed to the mass spectrometric (MS) studies, Yicheng Wang and Eric Benck (National Institute of Standards and Technology) who collaborated with our group on ion sampling measurements.

I appreciate those friends and colleagues Xuefeng Hua, Xi Li, Ling Zheng, Bryan Orf, Sebastian Engelmann, Ming-shu Kuo, Robert L. Bruce and Guido J. Stueber for helpful discussion and assistance in the work present in this thesis and maintenance of the lab. Particular and heartfelt thanks go to Jay Pyle and John Rodgers (IREAP) for selfless help in these years of study. I apologize in advance to those whose important contributions have been overlooked here because of my own unfamiliarity with them or my inability to fully appreciate their significance.

Finally, I would like to thank my parents, Ying Gao and Jiayu Ling, for their love, hope, encouragement, selfless support, and prayer. Without them, I would not be here. Thanks to my brother, Qing, and sister-in-law, Haiyan Zhao. I love you all.

Table of Contents

List of Tables

List of Figures

Fig. 2.4: Dependence of (a) deposition rate and (b) refractive index on CO additive to C_4F_8 and C_4F_8/Ar. The other experimental parameters were: 600 W inductive power, 40 sccm gas flow rate, and 6 and 20 mTorr pressure.

Fig. 2.5: C (1s) and O (1s) photoemission spectra of passively deposited films produced in C_4F_8, C_4F_8/50%CO, C_4F_8/Ar:2/8 and (C_4F_8/Ar:2/8)/50%CO discharge. The other experimental parameters were: 600 W inductive power, 40 sccm gas flow and 6 mTorr.

Fig. 2.6: Dependence of etch rates and selectivity on CO additive to (a) C_4F_8 and (b) C_4F_8/Ar measured using *in-situ* ellipsometry. The other experimental parameters were: 600 W inductive power, 40 sccm gas flow, 6 mTorr and –100 V bias voltage.

Fig. 2.7: Measured oxygen intensity (OI), F/C ratio, and steady-state thickness (SST) on the OSG, Si_3N_4 and SiC.

Fig. 2.8: Si (2p) photoemission spectra of partially etched SiC films produced in C_4F_8/70%CO and (C_4F_8/Ar:2/8)/70%CO discharge. The other experimental parameters were: 600 W inductive power, 40 sccm gas flow and 6 mTorr.

Fig. 2.9: Etching selectivity as a function of the steady state film thickness on (a) Si_3N_4 and (b) SiC etched by C_4F_8/CO and C_4F_8/Ar/CO. The other experimental parameters were: 600 W inductive power, 40 sccm gas flow and 6 mTorr.

Fig. 2.10: Electron impact energy thresholds for Ar, CO and C_4F_8 dissociation and ionization. Ar^M: argon metastable. The 11.11 eV is the thermal dissociation threshold for CO, and that average electron impact dissociation energy is12.94 eV according to Liu et.al[2.18].

optical model. The other experimental parameters were: C_4F_8/90%Ar, 600 W inductive power, 40 sccm gas flow, 10 mTorr and –100 V bias voltage.

Fig. 3.6: Dependence of (a) damaged layer refractive index and (b) damaged layer thickness and etch rates of 248 nm photoresist on time and analyzed by two layer optical model. The other experimental parameters were: C_4F_8/90%Ar, 600 W inductive power, 40 sccm gas flow, 10 mTorr and –100 V bias voltage.

Fig. 3.7: AFM photographs of blanket (a) 193 nm and (b) 248 nm photoresist partially etched in C_4F_8/90%Ar. The other experimental parameters were: 600 W inductive power, 40 sccm gas flow, 10 mTorr and –100 V bias voltage.

Fig. 3.8: RMS, R_a and R_{max} of partially etched blanket 193 nm and 248 nm photoresist measured by AFM. The other experimental parameters were: 600 W inductive power, 40 sccm gas flow, 10 mTorr and –100 V bias voltage.

Fig. 3.9: C (1s) photoemission spectra of (a) untreated and partially etched 193 nm and 248 nm photoresist films produced in (b) Ar and (c) C_4F_8/90%Ar discharge. The other experimental parameters were: For Ar discharge, 400 W inductive power, 40 sccm gas flow, 6 mTorr and –100 V bias voltage; for C_4F_8/90%Ar discharge, 600 W inductive power, 40 sccm gas flow, 10 mTorr and –100 V bias voltage.

Fig. 3.10: O (1s) photoemission spectra of (a) untreated and partially etched 193 nm and 248 nm photoresist films produced in (b) Ar and (c) C_4F_8/90%Ar discharge. The other experimental parameters were: For Ar discharge, 400 W inductive power, 40 sccm gas flow, 6 mTorr and –100 V bias voltage; for C_4F_8/90%Ar discharge, 600 W inductive power, 40 sccm gas flow, 10 mTorr and –100 V bias voltage.

Fig. 3.11: Dependence of CO intensity on processing time in C_4F_8/90%Ar produced by 193 nm, 248 nm photoresist and by background. The other experimental parameters were: 600 W inductive power, 40 sccm gas flow, 10 mTorr and –100 V bias voltage.

Fig. 3.12: Dependence of (a) CO intensity and (b) etch rates and refractive index of 193 nm photoresist on time in C_4F_8/90%Ar discharge. The other experimental parameters were: 600 W inductive power, 40 sccm gas flow, 10 mTorr.

Fig. 3.13: Negative SSIMS spectra of (a) untreated, (b) O_2 plasma exposed and (c) pure C_4F_8 etched, (d) C_4F_8/90%Ar etched 193 nm photoresist. The other experimental parameters were: for C_4F_8 and C_4F_8/90%Ar plasma, 600 W inductive power, 40 sccm gas flow, 10 mTorr and –100 V bias voltage; for O_2 plasma, 400 W inductive power, 40 sccm gas flow, 6 mTorr and without bias.

Chapter 4:

Fig. 4.1: (a) Schematic of small gap structure used in this work and comparison with (b) the high aspect ratio feature.

Fig. 4.2: (a) Schematic of dominant processes that are expected to control sidewall profiles and comparison with (b) the profile of an actual etched trench in OSG.

Fig. 4.3: Schematic diagram of the Capacitively Coupled Plasma system.

Fig. 4.4: (a) Measured ion current densities for Ar ( ), O_2 (O) and C_4F_8/90%Ar (Δ) plasmas as a function of bias power at both 100 W (void) and 300 W (solid) source power. (b) Normalized ion current densities for Ar ( ), O_2 (O) and C_4F_8/90%Ar (Δ) plasmas as a function of ratio between source power and bias power at 30 mTorr.

Fig. 4.5: Deposition rates of FC film both in the (a) exposed region and (b) completely shadowed region (solid bar) with and (open bar) without application of RF bias power for C_4F_8/90%Ar, (C_4F_8/90%Ar)/5%O_2, and (C_4F_8/90%Ar)/10%N_2 at 30 mTorr pressure, 200 W capacitive source power and 100 W bias power.

Fig. 4.6: Time dependent (a) FC film thickness and (b) Normalized FC deposition rates completely shadowed region for C_4F_8/90%Ar ( ), (C_4F_8/90%Ar)/5%O_2 (O), and (C_4F_8/90%Ar)/10%N_2 (Δ) measured at 30 mTorr pressure, 200 W capacitive power.

Fig. 4.7: Correlation $DR_{gap}/ER_{blanket}$ ratio with N_2 addition in (C_4F_8/90%Ar)/N_2 plasma at both 30 ( ) and 80 mTorr (O). The other experimental parameters were: 200 W capacitive power and 100 W bias power for etching and without bias for deposition.

Fig. 4.8: Si (2p) photoemission spectra of FC layer in the completely shadowed region on both (a) Si and (b) OSG substrates in C_4F_8/90%Ar, (C_4F_8/90%Ar)/10%N_2 and (C_4F_8/90%Ar)/5%O_2 plasmas at 30 mTorr pressure and 200 W capacitive power.

Fig. 4.9: C (1s) photoemission spectra of FC layer in the completely shadowed region on both (a) Si and (b) OSG substrates in C_4F_8/90%Ar, (C_4F_8/90%Ar)/10%N_2 and (C_4F_8/90%Ar)/5%O_2 plasmas measured at same conditions in Fig. 4.8. .

Fig. 4.10: N (1s) photoemission spectra of FC layer in the completely shadowed region on both (a) Si and (b) OSG substrates in C_4F_8/90%Ar, (C_4F_8/90%Ar)/10%N_2 and (C_4F_8/90%Ar)/5%O_2 plasmas measured at same conditions in Fig. 4.8.

Fig. 4.11: O (1s) photoemission spectra of FC layer in the completely shadowed region on both (a) Si and (b) OSG substrates in C_4F_8/90%Ar, (C_4F_8/90%Ar)/10%N_2 and (C_4F_8/90%Ar)/5%O_2 plasmas measured at same conditions in Fig. 4.8.

Fig. 4.12: F (1s) photoemission spectra of FC layer in the completely shadowed region on both (a) Si and (b) OSG substrates in C_4F_8/90%Ar, (C_4F_8/90%Ar)/10%N_2 and (C_4F_8/90%Ar)/5%O_2 plasmas measured at same conditions in Fig. 4.8.

Fig. 4.13: Cross-sectional SEM photographs of patterned photoresist partially etched in C_4F_8/90%Ar plasmas (a) before and (b) after O_2 plasma ashing. The other experimental parameters were: 200 W capacitive power, 30 mTorr and 100 W bias power for etching and without bias for O_2 ashing. The average deposition rate underneath the roof in 5 minutes is 0.3 nm/min.

Fig. 4.14: Cross-sectional SEM photographs of patterned photoresist partially etched in (a) (C_4F_8/90%Ar)/10%N_2 and (b) (C_4F_8/90%Ar)/5%O_2 plasmas after O_2 plasma ashing. The experimental parameters were same as in Fig. 15. The average deposition rates underneath the roof in 5 minutes are 0.2 and 0.18 nm/min for N_2 and O_2 addition, respectively.

Fig. 4.15: Correlation DR_{gap}/ER_{trench} ratio with "90 degrees minus the sidewall angle", which is the film deposition induced change in the sidewall angle from vertical.

Chapter 5:

Fig. 5.1: Time dependent FC film thickness obtained in the completely shadowed region for CF_4 ( ), CF_4/40%H_2 (O) and C_4F_8/90%Ar (Δ). The other experimental parameters were: 200 W capacitive power, 20 mTorr for CF_4, CF_4/40%H_2 and 30 mTorr for C_4F_8/90%Ar.

Fig. 5.2: C (1s) photoemission spectra of FC layer in the completely shadowed region on Si substrate in CF_4, CF_4/40%H_2 and C_4F_8/90%Ar plasmas. The experimental parameters were same as Fig. 5.1.

Fig. 5.3: C (1s) photoemission spectra of FC layer in the completely shadowed region on Si substrate in CF_4 and CF_4/40%H_2 plasmas. The experimental parameters were same as Fig. 5.1.

Fig. 5.4: Cross-sectional SEM photographs of patterned photoresist partially etched in CF_4 plasma (a) before and (b) after O_2 plasma ashing and in C_4F_8/90%Ar plasma (c) before and (d) after O_2 plasma ashing. The experimental parameters for plasma etching were same as Fig. 5.1, except that 100 W bias power is applied. For O_2 ashing, the experimental conditions are 30 mTorr, 200 W capacitive power and without bias.

Fig. 5.5: Cross-sectional SEM photographs of patterned photoresist partially etched in (a) CF_4/20%H_2 and (b) CF_4/40%H_2 plasma. The experimental parameters were same as those for pure CF_4 experiment in Fig. 5.4.

Fig. 5.6: Correlation DR_{gap}/ER_{trench} ratio with "90 degrees minus the sidewall angle", which is the film deposition induced change in the sidewall angle from vertical.

Chapter 6:

Fig. 6.1: Schematic of small gap structure used in this work.

Fig. 6.2: FC deposition rate at both 30 ( ) and 80 (O) mTorr and ICD at 30 mTorr (■) measured as a function of Ar addition. The source power is 200 W for deposition measurement and 300 W for ICD measurement.

Fig. 6.3: (a) The calculated average energy required to produce each ion and (b) to deposit each CF_2 group in the FC film as a function of gas composition are compared in both capacitively (■) and inductively ( ) coupled plasma.

Fig. 6.4: Deposition rates of FC film both (a) in the exposed region and (b) completely shadowed region for C_4F_8 and C_4F_8/90%Ar at both 30 and 80 mTorr pressure. The other experimental parameters were: 200 W capacitive power, 40 sccm gas flow, without bias (All the experimental parameters in the following figures are same unless otherwise indicated.).

Fig. 6.5: Time dependent (a) FC film thickness and (b) Normalized FC deposition rates in the completely shadowed region for C_4F_8 ( ) and C_4F_8/90%Ar at both 30 (solid) and 80 (void) mTorr pressure.

Fig. 6.6: C (1s) photoemission spectra of FC layer in the exposed region for C_4F_8 and C_4F_8/90%Ar plasmas at both 30 and 80 mTorr pressure.

Fig. 6.7: C (1s) photoemission spectra of FC layer in the completely shadowed region for C_4F_8 and C_4F_8/90%Ar plasmas at both 30 and 80 mTorr pressure.

Fig. 6.8: AFM images obtained on the surface of FC film deposited in the a) completely shadowed region and b) exposed region in pure C_4F_8 plasma at 80 mTorr. The time scale used for deposition was 5 minutes.

Fig. 6.9: Time dependent (1, 5 and 15 minutes deposition) C (1s) photoemission spectra of FC layer in the completely shadowed region in pure C_4F_8 plasma at 80 mTorr.

Fig. 6.10: Time dependent (1 and 5 minutes deposition) C (1s) photoemission spectra of FC layer in the completely shadowed region in pure C_4F_8. The other experimental

parameters were: 1000 W inductive power, 50 sccm gas flow, 150 mTorr, without bias.

Fig. 6.11: Schematic of FC film growth (a) in the exposed region and (b) in the completely shadowed region.

Fig. 6.12: Ar dependent C (1s) photoemission spectra of FC layer in the completely shadowed region deposited in C_4F_8/Ar plasma at 80 mTorr. The time scale used for deposition was 5 minutes.

Fig. 6.13: Power dependent C (1s) photoemission spectra of FC layer in the completely shadowed region in pure C_4F_8 at 80 mTorr. The time scale used for deposition was 5 minutes.

Fig. 6.14: Power dependent C (1s) photoemission spectra of FC layer in the completely shadowed region in pure C_4F_8. The other experimental parameters were: inductive power, 50 sccm gas flow, 150 mTorr, without bias.

Fig. 6.15: (a) C (1s) photoemission spectra and (b) corresponding change of C-F_2 and C-F_3 bonding of FC layer deposited in the completely shadowed region using different height gap structures in pure C_4F_8. The other experimental parameters were: 1000 W inductive power, 50 sccm gas flow, 150 mTorr, without bias, 5 minutes deposition.

Fig. 6.16: Optical microscopic images obtained on the surface of FC film deposited in the completely shadowed region in pure C_4F_8 plasma. The experimental parameters were same as in Fig. 6.15.

Chapter 1 Introduction

1.1 Plasma Processing of Advanced Electronic Materials

Plasma is a partially ionized gas containing an equal number of positive and negative ions, as well as non-ionized gas particles. The plasma state can exist over a broad temperature range (10^{2}~10^{9} K) and plasma densities (10^{3}~10^{33} m^{-3})[1.1-1.2]. It can be cool and tenuous like aurora, or very hot and dense like the central core of a star. This thesis deals with weakly ionized plasma discharges, which are characterized by $T_e \approx$1-10 eV, $T_i << T_e$ and $n \approx 10^{8}$-10^{13} cm^{-3} [1.3-1.5]. The advantage of this kind of plasma is that plasma and surface chemical reactions can take place under nonequilibrium conditions and the reactions can occur while the gas or substrates exposed to the plasma remain at low temperature[1.3-1.5]. Because of these characteristics, glow discharges are used extensively in the semiconductor industry for thin film processing applications including plasma enhanced chemical vapor deposition, surface modifications and pattern transfer by plasma etching[1.2-1.7].

An ongoing trend in the semiconductor industry has been a need to fabricate integrated circuits with more transistors on a smaller area. Another trend in the semiconductor industry has been to move away from Al interconnects and a SiO_2 interlayer dielectric to Cu metal and low-k dielectric materials. These new materials lead to the introduction of the "dual damascene" process, which is used to create the multi-level, high-density metal interconnections[1.8]. Fig. 1.1 shows the schematic of a completed dual damascene structure. It is clear that a series of difficult process integration steps must be successfully completed, especially if porous low k materials are utilized. As an example, achieving high etching selectivity of the low k material

with respect to the mask and the etch stop layer is an important objective. Furthermore, one must ensure that the plasma etching process does not adversely affect the dielectric constant of the film. Achieving these objectives required a better understanding of etch mechanisms of low k materials, photoresists and trench and via structures. In this thesis, we describe results of our research on etch mechanisms of these materials.

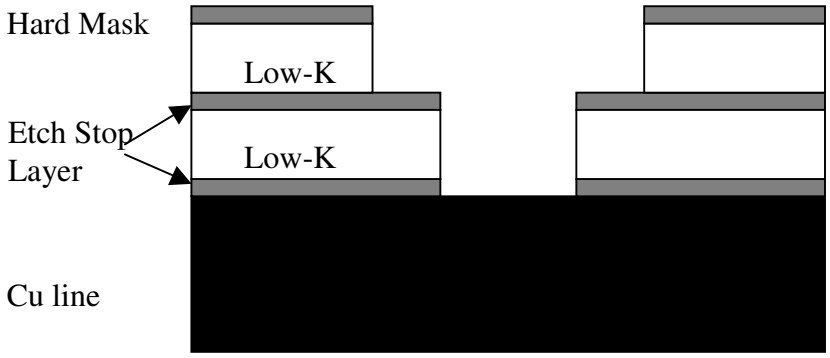

Fig.1.1: schematic of a completed dual damascene structure.

1.2 Introduction to Plasma Sources

Since the 1970s, capacitively coupled plasma sources excited at a frequency of 13.56 MHz have been commonly used in etch and deposition tools. The relatively low plasma density, $n_e \approx 10^9$-10^{10} cm^{-3}, which is typical for this type of source, is one of the major factors that limited plasma processing of complex structures. Therefore, several kinds of high-density plasma sources, including inductive sources, electron cyclotron resonance (ECR), and helicon resonance sources have been used for semiconductor fabrication[1.2, 1.9, 1.10]. Of these, the inductive source has achieved widespread use in the semiconductor industry due to its simplicity.

Low k material and especially porous low k materials are more susceptible to damage than conventional SiO_2. Also, etching selectivity of these materials relative to photoresist is poor in inductively coupled plasma sources. Therefore, there has been renewed interest in capacitively coupled plasma sources by the semiconductor industry. One serious limitation of the conventional capacitively coupled plasma source is that both ion energy and ion density are controlled by the same power source. To overcome this limitation, novel capacitively coupled plasma systems using two power sources operating at different RF frequencies have been introduced: The source power supply operating at higher frequency is used to control plasma generation, whereas the bias power supply operating at lower frequency is used to control ion bombardment energies.

In the following, we briefly review the basic principles of inductively coupled plasma and dual frequency capacitively coupled plasma sources. These principles will be illustrated using the reactors employed for this work.

1.2.1. Inductively Coupled Plasma

Inductively coupled plasma (ICP) is the simplest type of high-density plasma source. Fig. 1.2 shows the schematic layout of the ICP reactor used in this work. A planar coil, placed on top of a quartz coupling window, is used to generate the plasma. When an rf current is driven through the coil, this rf current induces an opposing rf current in the plasma. The plasma currents are concentrated primarily within a skin depth from the window, which for our conditions is typically a few centimeters. Therefore, the plasma acts as the secondary of a transformer with the

ICP coil as the primary. This explains the name transformer coupled plasma (TCP), which is sometimes used.

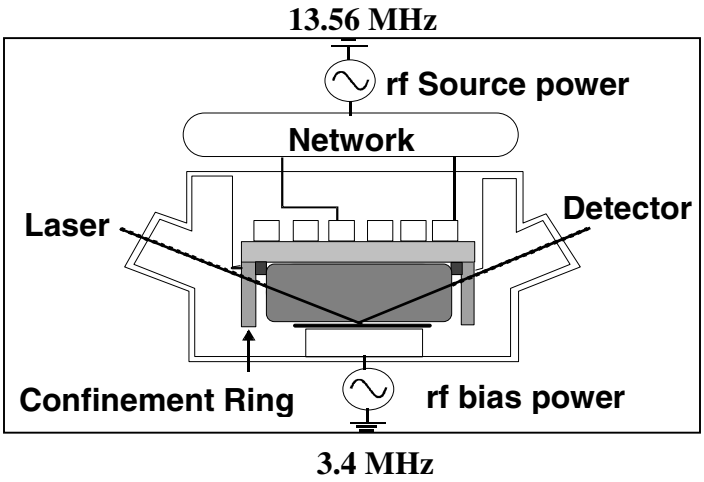

Fig. 1.2: Schematic diagram of the ICP reactor used in this work.

The rf current in the plasma is carried primarily by the thermal electrons due to their low mass and high mobility. Low energy electrons in this current cannot efficiently transfer their kinetic energy to the much heavier neutrals. Hence, electrons are heated by the electromagnetic fields while their direction is randomized by neutral collisions. The electron temperature is 3 to 5 eV for typical processing conditions, much higher than the ion and neutral temperatures, which are of the order of 0.05 eV. Energetic electrons can transfer their energies to neutrals through inelastic collisions which leads to ionization, dissociation, excitation, or a combination of these. In addition, attachment and recombination reactions take place. The electron energies required for these processes is in the range 1 to 20 eV. The electron temperature is adjusted so that electron generation through ionization balances the electron losses

from the plasma. Electrons are also lost due to ambipolar diffusion. Since the plasma is generated just below the window, electrons diffuse towards the quartz window, chamber walls, and the substrate. As electrons diffuse from the plasma generation area, an electric field builds up between the electrons and ions that accelerates the ions but slows down the electrons. This electric field increases the potential of the plasma generation area and assures that the flux of ions balances the flux of electrons. The diffusion of electrons is thus enhanced by the relatively high electron temperature, but is impeded by the ions. Additionally, all floating surfaces in contact with the plasma charge up negatively while a positive space charge builds up near the surface. This space charge is referred to as a sheath. The sheath thickness is on the order of 1 mm and is the only region where charge separation exists. All other areas can be considered quasi-neutral over a length scale larger than ~15 μm. The potential across the sheath relative a floating surface (the floating potential) is typically 10-30 V and accelerates ions that enter the sheath towards the floating surface. The fluxes of ions and electrons are governed by ambipolar diffusion, not by the floating potential (which is a result of the electron loss to the surface).

The energy of the ions bombarding the substrate can be increased by applying an rf bias to the substrate, which is achieved by employing an additional capacitive source. Generally, the flux of electrons and ions to the substrate is not affected by the rf bias. However, during the first rf cycles electrons are collected faster at the electrode which charges up more negatively while the positive sheath near the substrate expands. The repetition of this process increases the sheath voltage and, consequently, the average energy of impacting ions. The ability to control ion

energies independently from the control of plasma density is an important feature of high-density plasma systems.

1.2.2. Dual Frequency Capacitively Coupled Plasma

Capacitive sources, especially as implemented in the reactive ion etching (RIE) configuration, have been the most widely used plasma source for the semiconductor industry. Capacitively coupled plasmas employ one or more driven electrodes to produce the plasma. Fig. 1.3 shows the schematic of the dual frequency capacitively coupled plasma reactor used in this work. It features two internal electrodes driven at different RF frequencies. The high frequency source power supplied with a typical power level of 100-2000 W is used for ion generation. The bias power source operating at lower frequency, is used to control the energies of ions bombarding the substrate.

For the capacitively coupled plasma (CCP), the rf current and voltage sustaining the discharge is applied directly to an electrode immersed in the plasma. Therefore, the rf currents flowing across the sheath and through the bulk plasma lead to stochastic or collisionless heating in the sheath due to the oscillation of the sheath and ohmic heating in the bulk due to the collisions between electrons and other particles. Energetic electrons are also created at the cathode because of secondary emission from ion bombardment. These electrons are accelerated by the sheath into the body of the plasma. This secondary electron emission mechanism becomes important when the electrode is made of a material with high secondary electron emission coefficient.

For the CCP, an increase in plasma density requires an increase of the rf power, which increases the voltage on the driven electrode. A high sheath voltage leads to damage of the substrate and erosion of the electrode due to the strong ion bombardment. Typically, plasma densities of capacitively coupled plasma are kept relatively low and are mostly in the range of 10^{9}-10^{11} cm^{-3}. The pressure used in capacitively coupled plasma reactors, typical range is 20-300 mTorr, is usually higher than used in inductively coupled high-density plasma reactors. The plasma potential and the floating potential can be very high in capacitively coupled plasma reactors, ranging from tens to hundreds of Volts.

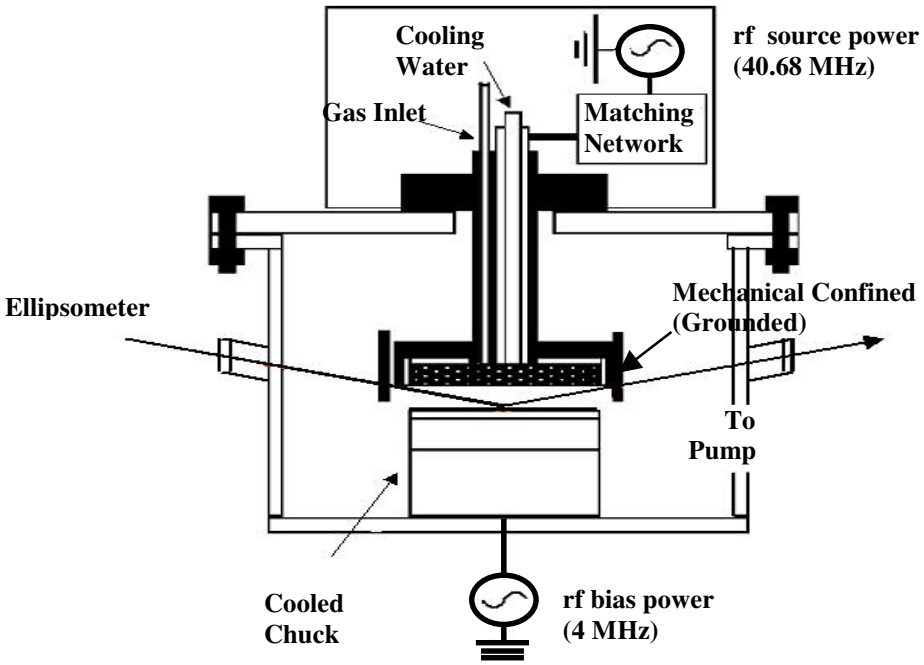

Fig. 1.3: Schematic diagram of the CCP reactor used in this work.

1.3. University of Maryland Laboratory for Plasma Processing of Materials

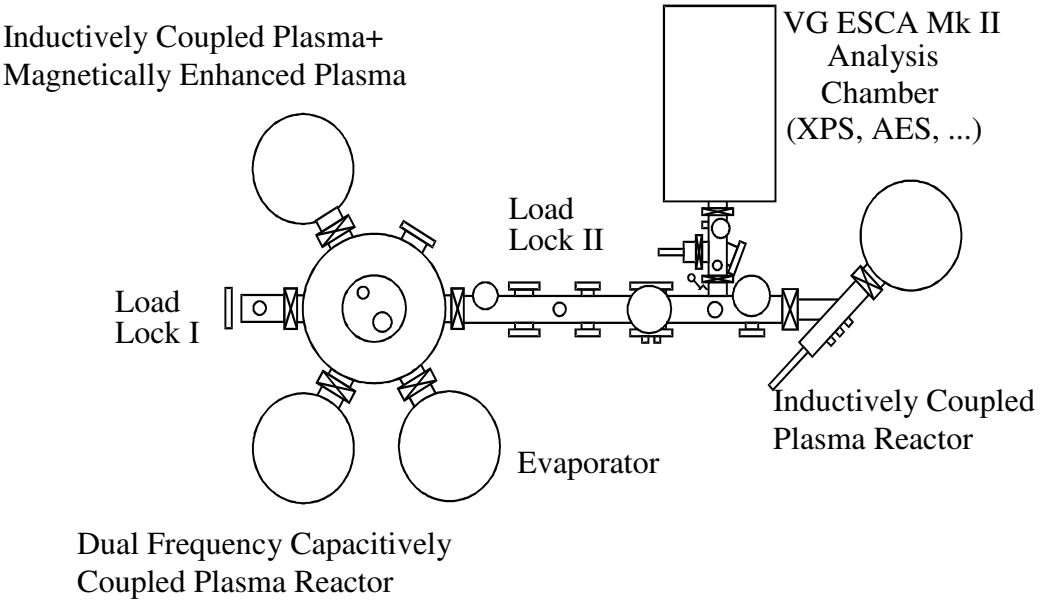

Fig. 1.4: University of Maryland cluster system for plasma processing.

Fig. 1.4 shows the cluster system for plasma processing of materials in our lab. Various plasma reactors, including the inductively coupled plasma reactor and the dual frequency capacitively coupled plasma reactor described above, are interconnected using this cluster system. In addition, a surface analysis chamber (Vacuum Generator ESCA Mk II) is also connected with these plasma processing chambers. Vacuum transfer of plasma treated samples to the surface analysis chamber is possible, and eliminates surface modification due to the air exposure.

To provide a comprehensive characterization of plasma properties, a variety of complementary measurements were conducted to obtain information of radical or ionic species. The applied techniques included mass spectroscopy, ion sampling, and

optical emission spectroscopy. These tools provide real time information on plasma properties and enhance process control. Furthermore, *in situ* ellipsometers are installed in each reactor to monitor the surface modification of the sample. After plasma processing, the sample can be characterized by X-ray photoelectron spectroscopy (XPS), atomic force microscopy (AFM), scanning electron microscopy (SEM) and secondary ion mass spectroscopy (SIMS). Our studies involved many collaborative efforts with industrial laboratories and universities throughout the world. I am grateful to these collaborators. To emphasize their contributions, a summary of the overall measurements involved in this thesis is shown in Table 1.1.

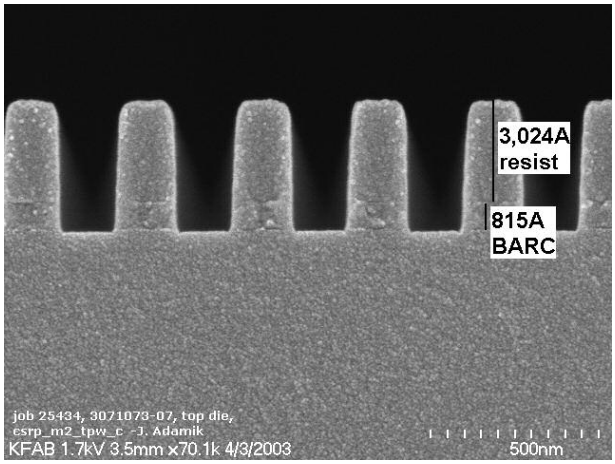

Fig. 1.5: Cross-sectional SEM photographs of trench structure of post BARC etch.

In this study, all patterned samples were prepared by the typical 193 nm photolighogrphy. For trench patterned wafers, 193 nm BARC of 82 nm thickness was coated, followed by 300 nm of 193nm photoresist. The wafers were exposed in a

Nikon step and scan system with a numerical aperture (NA) of 0.68. The BARC etching was carried out in a TEL DRM. The trench structure of post BARC etch is shown in the Fig. 1.5.

Measurement	**Method**	**Location**	**Information**
Ellipsometry	*In situ/ex situ*	UMD	Etch/deposition rates, optical properties
Langmuir probe	*In situ*	UMD	Ion current density, plasma potential
Mass spectrometry	*In situ*	UMD collaboration with Inficon	Radical species
Ion sampling system	*In situ*	UMD collaboration with NIST	Ion species and energies
X-ray photoelectron spectroscopy	*Vacuum transfer*	UMD	Chemical information
Atomic force microscopy	*Ex situ*	ITC-irst (Paolo Lazzeri, Erica Iacob and Mariano Anderle)	Surface morphology
Time of flight secondary ion mass spectroscopy	*Ex situ*	ITC-irst (Paolo Lazzeri, Erica Iacob and Mariano Anderle)	Chemical information
Scanning electron microscopy	*Ex situ*	Texas Instruments (Ping Jiang)	Characterizations of structures

Table 1.1: Plasma diagnostics and sample characterization tools used for this work.

1.4 Outline of Thesis

This thesis summarizes results of mechanistic studies of fluorocarbon-based plasma etching of advanced electronic materials using both inductively and

capacitively coupled discharges. Therefore, this thesis is divided in two parts: The first part, described in chapters 2 and 3, summarizes the work performed using the inductively coupled plasma reactor. The second part, presented in chapters 4, 5 and 6 summarizes the work undertaken using the capacitively coupled plasma tool.

Current inorganic low k material etch technology utilizes fluorocarbon plasmas to achieve required etching profile control and etch selectivity to mask and etch stop layers. The effect of CO addition to fluorocarbon-based plasmas for selective etching of organosilicate glass (OSG) over SiC or Si_3N_4 etch stop layers is discussed in chapter 2. Additionally, the contribution of Ar additives on the ionization of molecular gases such as C_4F_8 and CO, is addressed.

Plasma-based pattern transfer of lithographically produced nanoscale patterns in advanced photoresist materials is often accompanied by photoresist surface roughening and line edge roughening due to factors which are not well understood. In chapter 3, we studied the evolution of surface roughening in prototypical 193 nm and 248 nm photoresist materials during plasma processing as a function of plasma operating parameters.

The dual frequency power source provides enhanced process flexibility and allows for the etching of different materials, such as organic low k and silicon dioxide, in one chamber. In first part of chapter 4, we introduce a recently completed dual frequency capacitively coupled plasma system and discuss its characterization. The second part of chapter 4 introduces the concept of a gap structure designed to simulate FC film deposition on high-aspect ratio trench sidewalls during pattern transfer and then summarizes the results obtained in C_4F_8 based plasma, which

mainly concerns how the FC deposition on the sidewall affects the etching profile during the pattern transfer process. The corresponding results obtained in CF_4/H_2 based plasmas are summarized in chapter 5 and compared with the results obtained with C_4F_8 based plasmas.

The small gap structure provides a completely shadowed region without direct ion bombardment. The lack of ion bombardment for the shielded deposition increases the retention of the chemical structure of the FC film precursors in the deposited films. Studies of FC film growth in this condition and characterization of deposited films are summarized in chapter 6. This work clarifies the relative roles of neutrals and ions in the FC film growth process and the main mechanistic factors controlling the FC film growth process.

Finally, chapter 7 summarizes the main conclusions of this PhD thesis.

Chapter 2: Study of C_4F_8/CO and C_4F_8/Ar/CO Plasmas For Highly Selective Etching of Organosilicate Glass (OSG) over Si_3N_4 and SiC

J. Vac. Sci. Technol. A., 22,236 (2004)

Li Ling, X. Hua, X. Li, G. S. Oehrlein F. G. Celii, K. H. R. Kirmse, P. Jiang, Yicheng Wang and H. M. Anderson

Abstract:

We have examined the effect of CO addition to C_4F_8 or C_4F_8/Ar plasmas for selective etching of organosilicate glass (OSG) over SiC etch stop layers. The variation of important gas phase species, thin film etching rates and surface chemistry with feedgas composition was determined. CO addition exhibits dramatically different consequences on OSG/SiC etching selectivity when added to C_4F_8 or C_4F_8/Ar plasmas containing a high proportion of Ar. An improvement of the OSG/SiC etching selectivity results from CO addition to C_4F_8. We observe little CO dissociation in this case, which is plausible considering the lower dissociation energy threshold of C_4F_8 relative to CO. X-ray photoelectron spectroscopy (XPS) analysis of OSG and SiC surfaces shows that the etching selectivity improvement for C_4F_8/CO may be explained not only by an increase of the thickness and a reduction of the F/C ratio of the steady-state fluorocarbon surface layer on the SiC surface during etching, but little incorporation of CO into deposited fluorocarbon films. Adding CO to C_4F_8/Ar discharges with a high proportion of Ar leads to a reduction of the OSG/SiC etching selectivity. Significant dissociation of CO in Ar-rich C_4F_8/Ar/CO discharges is observed, consistent with the fact that the dissociation energy threshold of CO is

lower than the Ar ionization and metastable energies. Oxygen incorporation in deposited fluorocarbon films and a reduction of the steady-state fluorocarbon surface layer thickness on SiC are observed by XPS in this case, explaining the loss of OSG/SiC etching selectivity for C_4F_8/Ar/CO discharges.

2.1. INTRODUCTION

As ultralarge scale integrated (ULSI) circuits are scaled down, interconnect structures with two or more metal levels have become common for the production of high-density circuits and enhanced device performance. In these designs, the linewidth and spacings between metal interconnects are also made smaller. The speed-limiting factor is no longer the transistor delay, but the resistance capacitance (RC) delays associated with the metal interconnect system. The conventional dielectric material, silicon dioxide, has a dielectric constant (k) of ~4.0 and will no longer be adequate for advanced ICs. Therefore new low dielectric constant materials have been identified with good thermal stability (stable to above 400 °C), low coefficient of thermal expansion (CTE), low moisture uptake, high glass transition temperature (T_g), good mechanical properties, high dielectric breakdown field, good thermal conductivity and good adhesion to various substrates. In the past few years, one promising low-k dielectric, organosilicate glass (OSG) with a dielectric constant ranging from 2.6 to 3.1 was introduced, which meets the above requirements. This application requires plasma etching of OSG.

Fluorocarbon (FC) gases such as c-C_4F_8 are widely used in the microelectronics industry for etching traditional low dielectric constant thin films. Recently, CO addition to fluorocarbon gases has been extensively studied as a means to increase the etching selectivity of SiO_2 relative to other materials[2.1-2.7]. For instance, N. Omori et al.[2.5] report the achievement of high SiO_2/Si selectivity in reactive ion etching by adding a high percentage of CO to CHF_3. Hyun-Ho Doh et al.[2.2] studied both SiO_2/Si and SiO_2/photoresist etching selectivity using these gas

mixtures. They also found improved SiO_2/Si etching selectivity when a high proportion of CO was used. Hayashi et al.[2.3] investigated the mechanism of high SiO_2 to Si_3N_4 etching selectivity using C_4F_8 and CO in their magnetron plasma system. Their results showed a high SiO_2/Si_3N_4 etching selectivity was achieved when the CO gas-mixture ratio exceeded 75%.

In this work, we studied the plasma etching behavior of OSG, Si_3N_4, and SiC in C_4F_8/CO and C_4F_8/Ar/CO plasmas in order to establish the impact of CO addition to the OSG etch processes. The current work is also motivated by previous studies of this group aimed at achieving high etching selectivity of OSG relative to Si_3N_4 and SiC etch stop layers by N_2 addition to C_4F_8 and C_4F_8/Ar [2.8]. In that work we found that the effect of N_2 addition to C_4F_8 on etching behavior of OSG, Si_3N_4 and SiC is weak because of the high stability of N_2 relative to C_4F_8. Similar effects may be expected when adding CO to a fluorocarbon gas. CO is very stable and its thermal dissociation energy threshold of 11.1 eV and its average electron impact dissociation energy is 12.94 eV, which is greater than that of N_2 (9.8 eV). When Ar was simultaneously present at a high concentration, i.e. for $C_4F_8/Ar/N_2$ gas mixtures, a completely different behavior was observed which could be explained by N_2 dissociation. Although the addition of Ar is thought to increase the importance of ion bombardment relative to neutral and direct reactive ion etching[2.9, 2.10], the predominant effect of Ar on C_4F_8/Ar/CO discharge chemistry is likely to be due to changes in the CO dissociation relative to C_4F_8/CO. In this work we performed gas phase and surface studies, along with etch rate studies to establish these effects, and to establish

the role of CO addition to C_4F_8 or C_4F_8/Ar:2/8 on the etching selectivity of OSG relative to Si_3N_4 and SiC etch stop layers.

2.2. EXPERIMENTAL

The transformer coupled plasma (TCP) reactor used in this work has been described in earlier articles of this group[2.11]. All experiments described here were carried out in discharges at pressures ranging from 6 to 20 mTorr, fed with 40 sccm (standard cubic centimeters per minute) total gas flow, and maintained using 600 W source power at 13.56 MHz. For the etching experiments, blanket films of OSG, SiO_2, Si_3N_4, SiC and poly-Si on Si chips of approximately 2 cm × 2 cm in size were positioned at the center of a 125 mm electrode. We employed C_4F_8/CO and (C_4F_8/Ar:2/8)/CO plasmas for these studies. For the C_4F_8/Ar/CO experiments, the C_4F_8/Ar flow rate ratio was fixed at 2:8. The C_4F_8, Ar, and CO flows were adjusted to maintain this constant C_4F_8/Ar ratio and a total flow of 40 sccm. The ion energy at the wafer can be controlled independently of the plasma generation by a variable frequency (0.4-40 MHz) rf power supply (0-300 W). For this study the rf frequency was fixed at 3.7 MHz, and the rf bias power varied up to 250 W. For all etching experiments in which the gas composition was varied, the self-bias voltage was fixed at –100 volts. A rotating compensator ellipsometer in the polarizer-compensator-sample-analyzer (PCSA) configuration with a 638.2 nm He/Ne laser was used to determine thin film etching rates and the introduction of surface modifications in real time. The absolute gas phase densities of CF, CF_2 and COF_2 were determined by Infrared Laser Absorption Spectroscopy (IRLAS). A Langmuir probe was used to

determine the ion current density at a distance of 2 cm above the wafer surface, as a function of feedgas composition. The current densities at the electrode are about 30% samller than this value. A quadrupole mass spectrometer with an energy filter was used to determine the ion composition at the same position. X-ray photoelectron spectroscopy (XPS) measurements were performed with partially etched thin films to determine changes in surface composition. These measurements were performed at a 90^{o} take-off angle using a nonmonochromatized Mg K-alpha X-ray source (1253.6 eV).

2.3. RESULTS AND DISCUSSION

2.3.1. Ion Current Density (ICD)

Fig. 2.1 shows the variation of the ion current density with the percentage of CO added to C_4F_8 and C_4F_8/Ar:2/8 plasmas at 600 W inductive power, and a total gas flow rate of 40 sccm at pressures of 6 or 20 mTorr. Overall a trend to lower ion current density is observed as CO is added, except for the 6 mTorr data in the case of C_4F_8/CO. For the (C_4F_8/Ar:2/8)/CO discharges the ion current density is much higher than for the C_4F_8/CO discharges. This can be explained by the strongly increased ionization and dissociation of (C_4F_8/Ar:2/8)/CO discharges[2.12]. When CO is added to C_4F_8/Ar:2/8, a strong reduction of the ion current density is observed (by 50 to 66%), which is the result of CO dissociation competing with the ionization of the feed gas mixture. The decrease of the ion current density is much smaller when CO is added to C_4F_8.

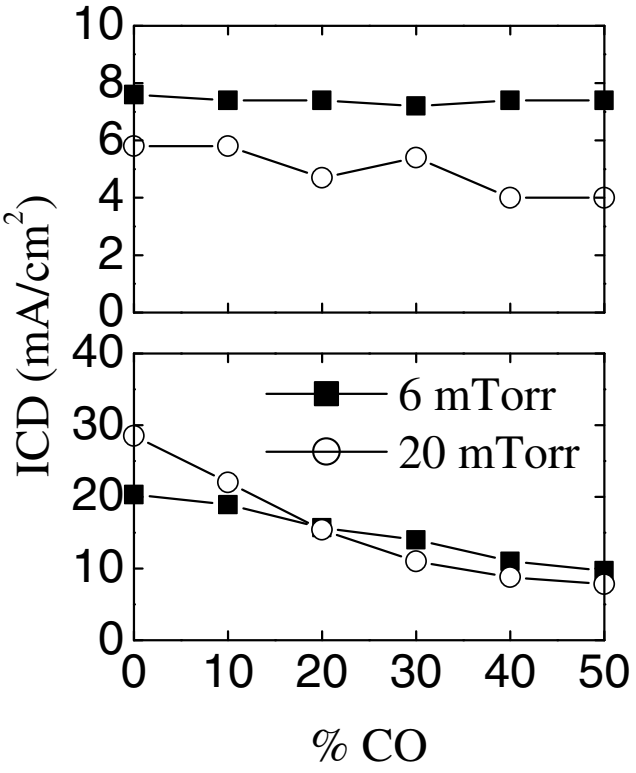

Fig. 2.1: Dependence of ion current density on the percentage of CO added to (a) C_4F_8 and (b) C_4F_8/Ar:2/8 measured using a Langmuir Probe. The other experimental parameters were: 600 W inductive power, 40 sccm gas flow rate, and 6 and 20 mTorr pressure.

2.3.2. Ion Composition

A compositional analysis of an ion flux as a function of feedgas composition was performed using the ion sampling system consisting of a quadrupole mass spectrometer with an energy filter. Fig. 2.2 compares the ion flux composition for C_4F_8 and C_4F_8/Ar:2/8 plasmas before and after adding 50% CO. The plasma was

operated at 600 W inductive power and a pressure of 6 mTorr and a total gas flow of 40 sccm. Similar data were obtained at 20 mTorr pressure.

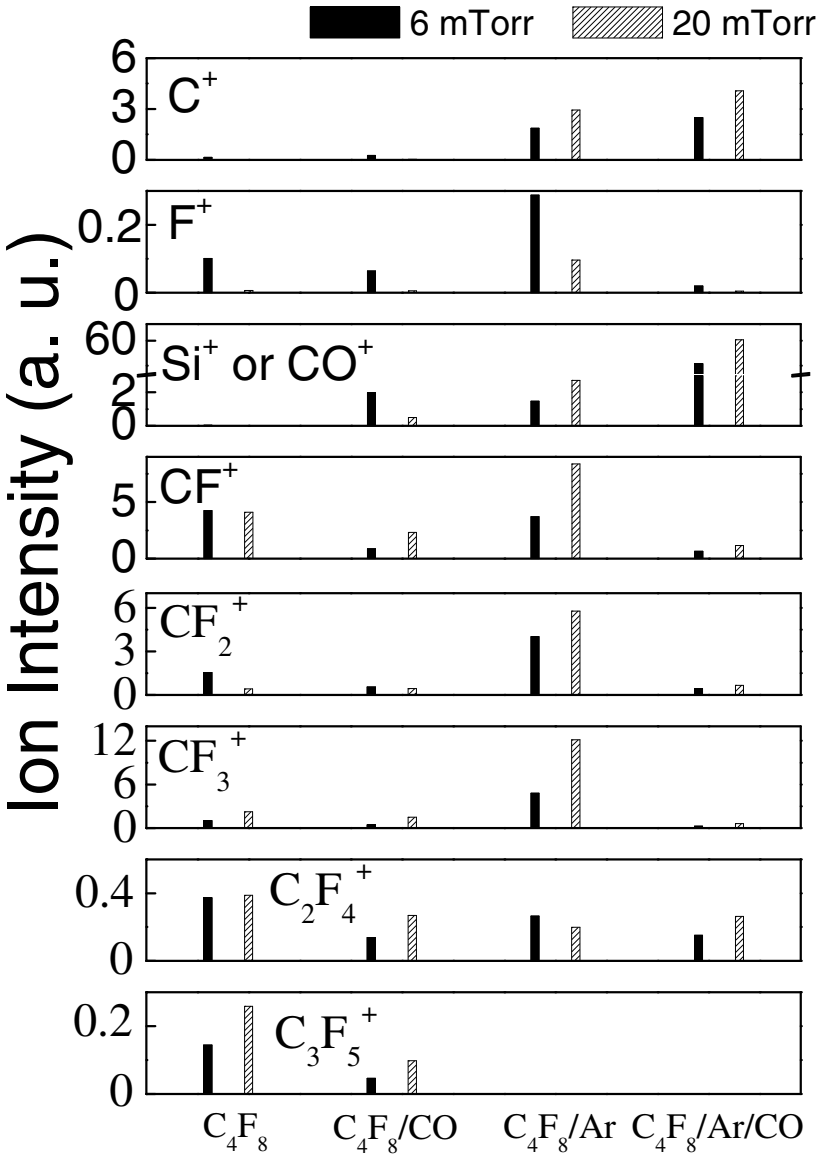

Fig. 2.2: Ion flux composition in C_4F_8, C_4F_8/50%CO, C_4F_8/Ar:2/8 and (C_4F_8/Ar:2/8)/50%CO plasma. The other experimental parameters were: 600 W inductive power, 40 sccm gas flow rate, and 6 and 20 mTorr pressure.

For pure C_4F_8, ionic fragments are detected at *m/e*=12 (C^+), 19 (F^+), 31 (CF^+), 50 (CF_2^+), 69 (CF_3^+), 100 ($C_2F_4^+$), 131 ($C_3F_5^+$). The dominant ionic species is CF^+. This may be explained by multi-step processes involving C_4F_8 dissociation and successive ionization of the fragments to produce CF^+ ions. When CO is added, the intensities of CF^+, CF_2^+ and CF_3^+ decrease significantly, but still remain the dominant ionic species. Addition of Ar to C_4F_8 causes a significant increase of C_4F_8 dissociation. Heavier ions like $C_2F_4^+$ and $C_3F_5^+$ vanish almost completely, whereas lighter ions increase in importance, e.g. C^+. For C_4F_8/Ar with and without CO, a strong peak at *m/e*=28 at appears, which is assigned to CO^+ or Si^+. For C_4F_8/Ar/CO the spectrum is dominated by CO^+ and is explained by CO ionization. For C_4F_8/Ar the CO^+ or Si^+ impurities can be explained by capacitive coupling effects of the coil and etching of the quartz window[2.13]. For both Ar containing discharges the strong C^+ signals suggest strong dissociation of C_4F_8 and/or CO.

2.3.3. Infrared Laser Absorption Measurement

The densities of CF, CF_2, and COF_2 neutral radicals were determined using Infrared Laser Absorption Spectroscopy (IRLAS). Fig. 2.3 (a) shows the densities of CF, CF_2, and COF_2 calculated from the infrared absorption spectra obtained with C_4F_8/CO plasmas at 40 sccm gas flow for pressure of 20 mTorr, and 600 W inductive power. The radical densities were measured for either fluorocarbon deposition (no RF bias) or Si etching (at –100 V self-bias voltage). Figure 2.3 shows that the density of all FC radicals is slightly reduced as the CO percentage is increased. The CF_2 partial pressure is about 40 times greater than that of CF or COF_2. When an RF bias is

applied and etching of the fluorocarbon film and Si substrate begins, the CF_2 radical density decreases for all gas mixture. This may be explained by radical consumption in the etching process[2.13].

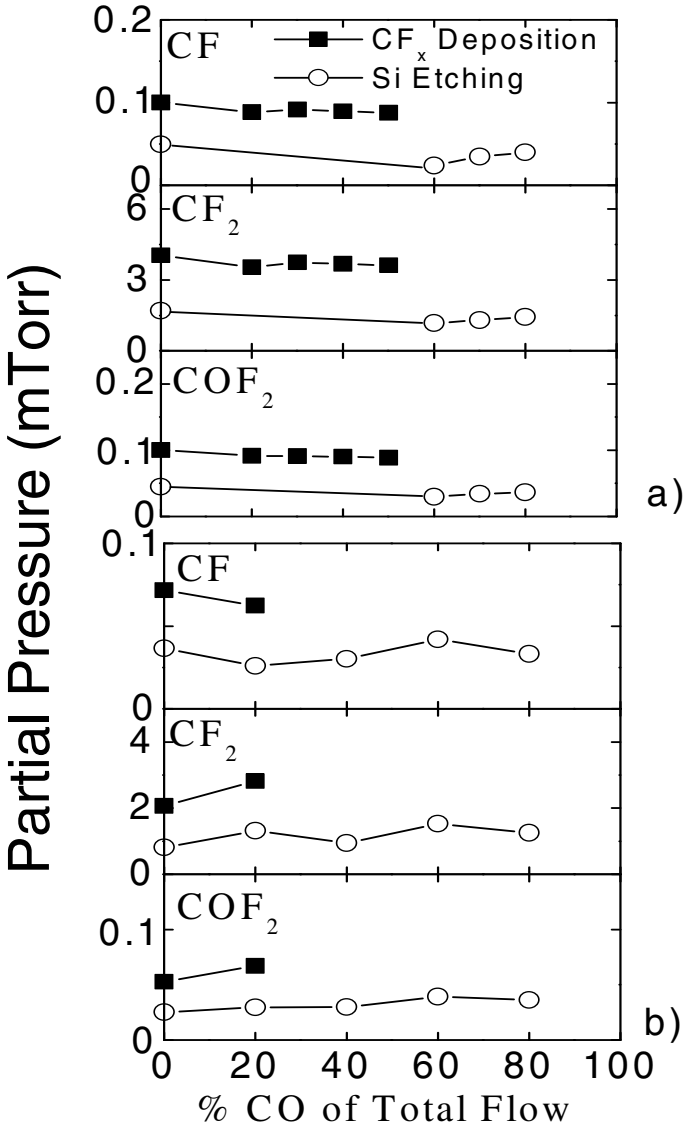

Fig. 2.3: Dependence of CF, CF_2 and COF_2 radical partial pressure on CO additive to (a) C_4F_8 and (b) C_4F_8/Ar:1/9. The other experimental parameters were: 600 W inductive power, 40 sccm gas flow rate, and 20 mTorr pressure.

The CF, CF_2 and COF_2 radical densities for the same deposition and etching processes using the Ar-rich discharges are shown in Fig. 2.3 (b). Although Ar addition strongly increases the dissociation of C_4F_8, the radical densities for all experimental conditions shown here are lower than for the corresponding C_4F_8/CO plasmas because of the much lower partial pressure of C_4F_8.

2.3.4. Influence of CO Addition on Fluorocarbon Deposition Rates

In fluorocarbon plasma processing, the deposition characteristics are dependent on the feedgas chemistry. Figure 2.4 (a) shows the measured fluorocarbon deposition rates for floating substrates (no rf bias applied) as a function of the percentage CO added to C_4F_8 or C_4F_8/Ar discharges. We used 6 mTorr and 20 mTorr pressure, 600 W inductive power and a total gas flow rate of 40 sccm. The measured deposition rates at 20 mTorr are higher than at 6 mTorr for both C_4F_8/CO and C_4F_8/Ar/CO discharges. When CO is added to C_4F_8, the FC film deposition rate decreases continuously as the amount of CO is increased. When CO is added to C_4F_8/Ar, the deposition rate varies little up to about 20% CO, and at higher CO percentages shows a small decrease. The deposition rate measured for C_4F_8/Ar/CO is significantly lower than seen for C_4F_8/CO. Figure 2.4 (b) shows the corresponding refractive index of the deposited fluorocarbon films. Generally, the refractive index of the deposited films increases with increasing CO in the gas phase which implies that the fluorine-content of the fluorocarbon films decreases. The refractive index increase occurs for much lower percentages of CO in the case of C_4F_8/Ar/CO than for C_4F_8/CO. We will see below that the XPS data show significant C and O

incorporation in the carbonaceous film in this case. For C_4F_8/CO the FC deposition rate shows a strong decrease when the concentration of CO increases above 60%. This can be explained by the reduction of the fluorocarbon gas flow rate. For these CO-rich discharges CO dissociation becomes important, and likely causes the abrupt increase of the refractive index (see Fig. 2.4(b)).

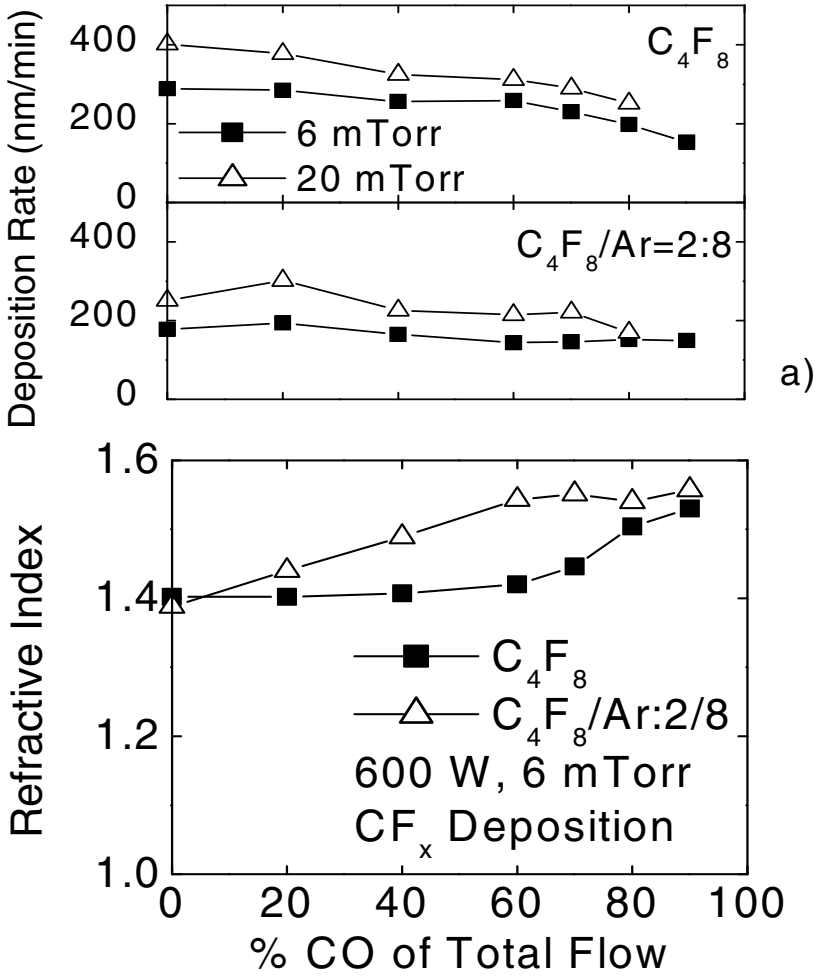

Fig. 2.4: Dependence of (a) deposition rate and (b) refractive index on CO additive to C_4F_8 and C_4F_8/Ar. The other experimental parameters were: 600 W inductive power, 40 sccm gas flow rate, and 6 and 20 mTorr pressure.

For the Ar-rich plasma, the fluorocarbon deposition rate decreased slightly and saturated at 60% CO addition. The slight reduction may be explained by the reduced C_4F_8 flow rate and is in part compensated by the strongly increased dissociation of CO. With increased CO addition, dissociation of CO becomes more important and carbon rather than fluorocarbon species is incorporated into the deposited film, causing the increase of the refractive index.

2.3.5. Surface Analysis of Deposited Films: XPS

The deposited fluorocarbons were analyzed by X-ray photoelectron spectroscopy (XPS), paying in particular attention to the carbon and oxygen 1s core levels. Figure 2.5 shows the C (1s) photoemission spectra of 300 nm thick fluorocarbon films deposited on the Si substrate using different gas mixtures (C_4F_8, C_4F_8/70%CO, C_4F_8/Ar:1/9 and (C_4F_8/Ar:2/8)/70%CO. Four peaks can be clearly identified in the C 1s spectrum obtained with a film deposited using pure C_4F_8. These are identified as C-C or C-CF_x (x=1,2,3), CF, CF_2 and CF_3 bonding, respectively. The spectra change as CO is added to C_4F_8. The intensity of the CF_2 and CF_3 peaks decreases with increasing CO concentration, whereas the intensities of C-C or C-CF_x (x=1,2,3) and CF increase. This indicates that a carbon-rich fluorocarbon film is produced by the addition of CO into the C_4F_8/CO plasma. A similar change in the C 1s spectrum is seen when Ar is added to C_4F_8. The mechanisms to produce films with a lower fluorine content may in the case of C_4F_8/CO be postulated to be due to a reaction of CO and fluorocarbon radicals[3], whereas for C_4F_8/Ar it should be caused by the increased dissociation of C_4F_8[12,13]. For (C_4F_8/Ar:2/8)/70%CO discharges, both

mechanisms are operative, and Ar also should increase the dissociation of CO. In this case the C-C or C-CF_x (x=1,2,3) and CF peaks dominate the C 1s spectrum.

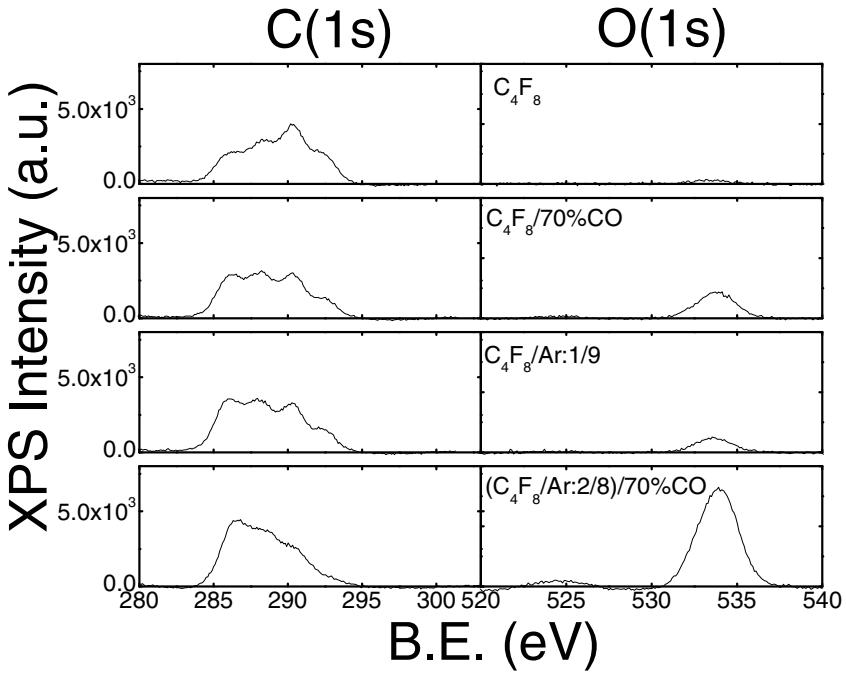

Fig. 2.5: C (1s) and O (1s) photoemission spectra of passively deposited films produced in C_4F_8, C_4F_8/50%CO, C_4F_8/Ar:2/8 and (C_4F_8/Ar:2/8)/50%CO discharge. The other experimental parameters were: 600 W inductive power, 40 sccm gas flow and 6 mTorr.

The corresponding O (1s) photoemission spectra are also shown in Fig. 2.5. For C_4F_8 and C_4F_8/CO little oxygen incorporation is seen, e.g. even when 70% CO was added to C_4F_8, the observed O (1s) peak was still very small. For the Ar-rich C_4F_8 gas mixtures, an oxygen signal was seen both with (large) and without (small) CO. The unexpected small O (1s) peak seen for C_4F_8/Ar is due to etching of the

quartz coupling window[2.13]. When both Ar and CO were added to C_4F_8, strongly increased oxygen incorporation was observed. This suggests a strongly increased dissociation of CO for C_4F_8/Ar/CO plasmas.

2.3.6. Influence of CO Addition on Thin Film Etching Rates

The etch rates of blanket films of OSG, SiO_2, Si_3N_4, SiC, and poly-Si were measured at a fixed self-bias voltage of –100 V for C_4F_8/CO and C_4F_8/Ar/CO discharges. Fig. 2.6 shows the measured etch rates as a function of the percentage of CO added to C_4F_8 or C_4F_8/Ar:2/8. A total gas flow of 40 sccm and a pressure of 6 mTorr were used, and the inductive power level was 600 W. SiO_2, OSG and Si_3N_4 on the one hand, and poly-Si and SiC on the other hand, show a similar dependence of the etching rate on gas composition. This was previously observed when investigating the influence of N_2 addition to fluorocarbon discharges on etching behavior[2.8]. The differences in etching behavior can be attributed to substrate-specific abilities to gasify carbon during plasma etching. By the interaction of carbon with substrate atoms the balance between fluorocarbon deposition and fluorocarbon etching is affected, which controls the fluorocarbon steady-state thickness and ultimately the substrate etching rate[2.11]. In the case of Si and SiC, no volatile products can be formed by an interaction of substrate atoms with carbon, and a relatively thick steady-state fluorocarbon film develops. For SiO_2 and OSG, most of carbon is consumed by the reaction with substrate oxygen, leading to a relatively thin steady-state fluorocarbon film, and a high steady state etching rate. Nitrogen atoms from Si_3N_4 are less reactive than O with C and CF_x and generate volatile CN and FCN. This results in a lower

etching rate than seen for SiO_2 and OSG, but a similar dependence of the etching rate on gas composition.

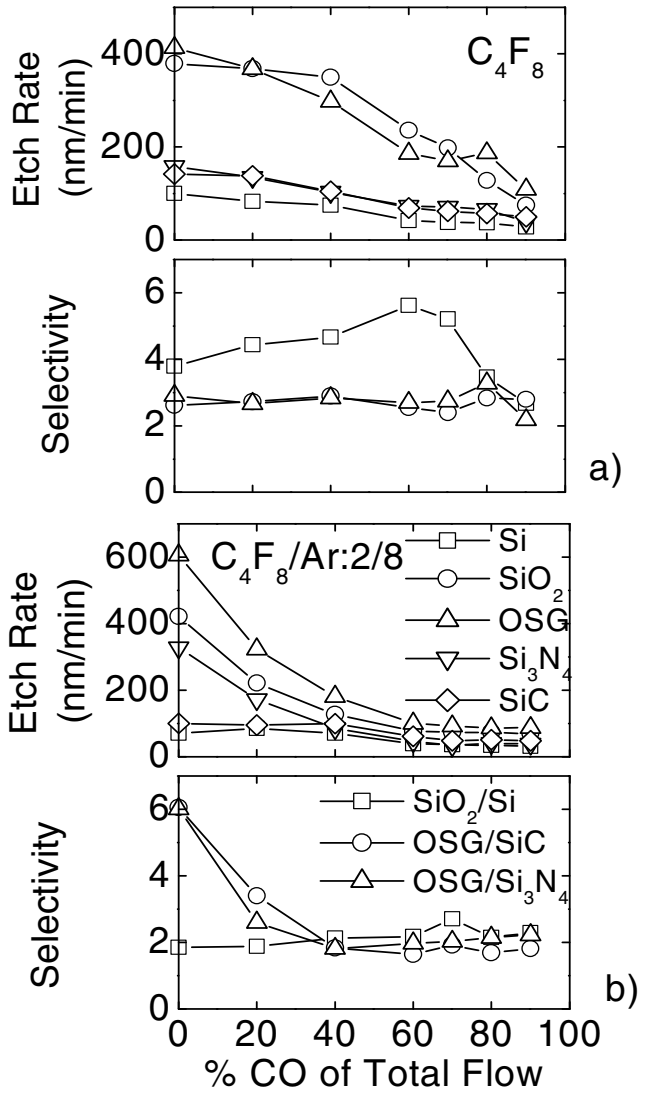

Fig. 2.6: Dependence of etch rates and selectivity on CO additive to (a) C_4F_8 and (b) C_4F_8/Ar measured using *in-situ* ellipsometry. The other experimental parameters were: 600 W inductive power, 40 sccm gas flow, 6 mTorr and –100 V bias voltage.

Figure 2.6 also shows the dependence of the SiO_2/poly-Si, OSG/Si_3N_4 and OSG/SiC etch rate ratios on the percentage of CO added to C_4F_8 or C_4F_8/Ar:2/8. We used a C_4F_8/Ar/CO gas mixture for the etching of blanket films of OSG, Si_3N_4, SiO_2, SiC, and poly-Si. For these gas mixtures the ratio of C_4F_8 to Ar is fixed at 2:8. We chose this ratio of C_4F_8 to Ar because we have found that the SiO_2/Si etching selectivity is optimized at this Ar-rich gas mixture[2.12, 2.13].

2.3.6.1. C_4F_8/CO

The maximum etch rate is obtained for all the materials in pure C_4F_8 plasmas. The etch rates decrease with the increase of the CO concentration, which can be explained by a limitation of the etchant. The SiO_2/poly-Si etching selectivity increases with the amount of CO added and peaks at 60% CO. Above 70% CO a strong decrease of the SiO_2/poly-Si selectivity is observed. This is consistent with data previously published by Akimoto et.al[7]. The selectivity of SiO_2/SiC and SiO_2/Si_3N_4 remains nearly constant as CO is added to C_4F_8. For C_4F_8/CO plasmas the effects on etching behavior are weak because of the stability of the CO molecule.

2.3.6.2. C_4F_8/Ar/CO

Addition of Ar to fluorocarbon gas is used to enhance the dissociation and ionization of the molecular gases[2.9, 2.10]. SiC and Si exhibits a similar dependence on the percentage CO added: the etching rates increase initially, then decrease, and finally saturate when a high percentage of CO had been added. For OSG, Si_3N_4 and SiO_2, the etching rates show a strong decrease as CO is added and saturate at 70% CO

addition. The OSG/SiC and SiO_2/poly-Si etch rate ratio show a very similar trend as a function of the amount of CO added.

2.3.7. Surface Analysis of Partially Etched Samples Using XPS

The steady state fluorocarbon layer thickness is a key parameter that determines the etching rate of a thin film and therefore the etch rate ratio of two materials[2.11]. To explore the effect of CO addition on the steady state fluorocarbon layer thickness and etching behavior, we analyzed surfaces of partially etched OSG, Si_3N_4, SiC thin films using XPS. Samples of these materials were processed using a self-bias voltage of –100 V at the same gas compositions and process parameters as used for the fluorocarbon film deposition experiments described above.

To evaluate the effect of CO addition on the composition of the fluorocarbon layers formed on the various thin film materials, the oxygen intensity and the ratio of fluorine to carbon (F/C) for each partially etched sample were calculated from the O (1s) and C (1s) XPS spectra, respectively. The oxygen intensity is calculated from the O (1s) peak area, and the F/C ratio is defined as[2.11]:

$$F/C = \frac{\sum_{i=1}^{3} iI(C-F_i)}{I(C-Si)+I(C-C)+\sum_{i=1}^{3} iI(C-F_i)}$$

where I(…) is the area of the fitted Gaussian function for the chemically shifted contribution indicated between the parentheses. The F/C ratio presented here is the ratio of the fluorine in the fluorocarbon film to the density of C (1s), which is an approximation, since this layer also may contain CO. The use of the F 1s peak to

estimate the fluorine content is not possible, since some of the fluorine has reacted and is associated with the substrate.

The steady-state surface reaction layer thickness can be estimated from the Si (2p) or C (1s) spectra[2.14, 2.15]. Since both OSG and SiC contain carbon, the steady state fluorocarbon thickness in this work is measured using the corresponding Si (2p) spectra. The layer thickness was calculated from the decrease of the Si (2p) intensity relative to the Si (2p) intensity measured for untreated material according to[2.14]:

$$d_{CF} = -\lambda_{Si(2p)} \ln(I_{Si(2p)} / I_o) \sin\theta$$

Here $\lambda_{Si(2p)}$ is the escape depth of Si (2p) photoelectrons in the CF_x layer (assumed to be 3.0 nm); θ the photoelectron take off angle (90° in this work); and $I_{Si(2p)}$ and I_0 are the Si (2p) photoemission peak intensities of partially etched or untreated samples, respectively.

2.3.7.1. C_4F_8/CO

Fig. 2.7 shows the oxygen intensity observed on top of the different materials for all gas compositions. OSG has the highest oxygen intensity on the surface, and Si_3N_4 has the lowest. For pure C_4F_8 discharges, the small oxygen signal for partially etched Si_3N_4 and SiC originates from erosion of the quartz coupling window. The much larger oxygen signal for OSG is due to the material itself. The oxygen intensities observed with all materials increase when 70% CO was added to C_4F_8.

The F/C ratio and the steady state fluorocarbon film thicknesses for the partially etched OSG, Si_3N_4, and SiC thin films are also shown in Fig. 2.7. The F/C ratios for all materials decrease with CO addition. The F/C ratio measured with OSG

films decreased more significantly than seen for Si_3N_4 and SiC. In addition, the steady state film thickness for Si_3N_4 and SiC substrates remained nearly constant, whereas the FC film thickness for an OSG substrate decreased significantly.

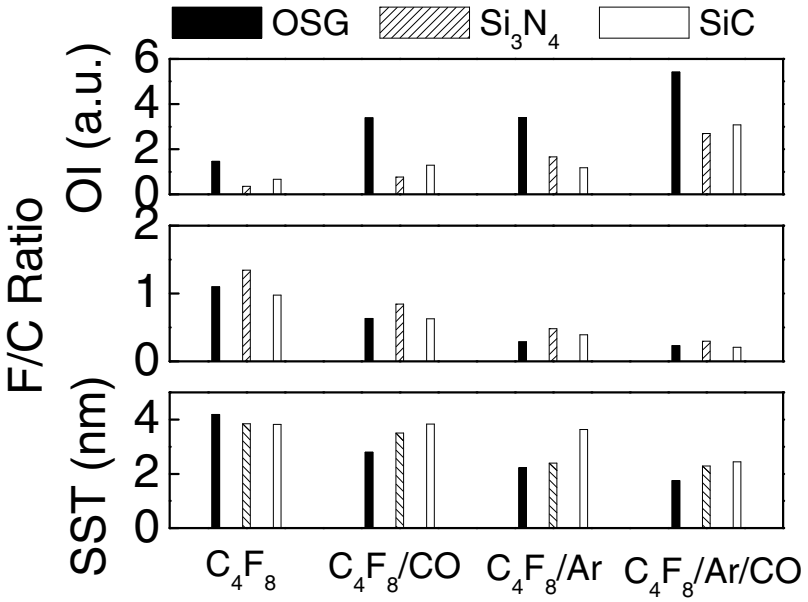

Fig. 2.7: Measured oxygen intensity (OI), F/C ratio, and steady-state thickness (SST) on the OSG, Si_3N_4 and SiC.

2.3.7.2. C_4F_8/Ar/CO

Corresponding results for CO addition to C_4F_8/Ar:2/8 discharges are also shown in Fig. 2.7. CO addition to C_4F_8/Ar:2/8 causes similar changes in the surface characteristics of partially etched films as CO addition to C_4F_8, in particular an increase of the oxygen intensity, and a decrease of the F/C ratio of the FC film. However, for (C_4F_8/Ar:2/8)/CO discharges the oxygen intensity measured with partially etched samples is much higher than for C_4F_8/CO, especially for the SiC surface. Si (2p) photoemission spectra of SiC films partially etched using either

C_4F_8/70%CO or (C_4F_8/Ar:2/8)/70%CO discharges are compared in Fig. 2.8. The two peak components shown are attributed to Si-C and Si-O bonding. The Si-O peak component measured after SiC etching in (C_4F_8/Ar:2/8)/70%CO discharges is of much greater intensity than after etching using C_4F_8/70%CO plasmas. The increased oxidization of the SiC substrate seen for the (C_4F_8/Ar:2/8)/70%CO discharge indicates increased CO dissociation for the Ar-rich gas mixture. This conclusion is also supported by studies of the C (1s) spectra.

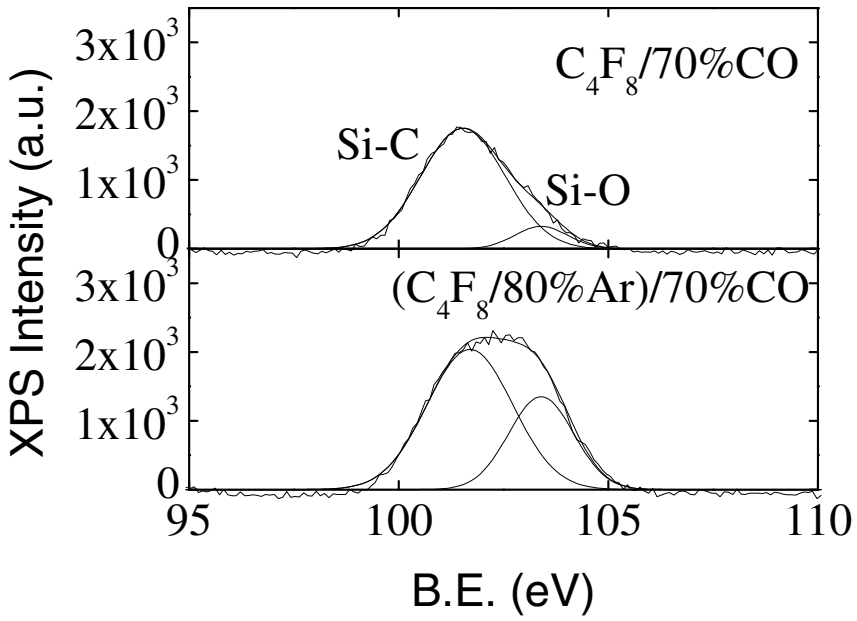

Fig. 2.8: Si (2p) photoemission spectra of partially etched SiC films produced in C_4F_8/70%CO and (C_4F_8/Ar:2/8)/70%CO discharge. The other experimental parameters were: 600 W inductive power, 40 sccm gas flow and 6 mTorr.

The properties of the steady-state fluorocarbon film on a substrate, i.e. the film composition and thickness, play a dominant role in controlling the magnitude of

the substrate etch rate. In Fig. 2.7 we also compare the measured F/C ratios for all substrates. An important effect of Ar addition to C_4F_8 is that the steady-state FC film becomes more fluorine deficient. The reduction of the fluorine content is explained by the increased ion bombardment of the FC film that takes place in C_4F_8/Ar discharges for which the plasma density is increased relative to C_4F_8. When CO is added to C_4F_8/Ar, a further decrease of the F/C ratio is observed, and a carbon-rich steady-state FC film is produced, which causes a decrease of the substrate etch rate.

It has been found that when the FC steady-state film thickness on a substrate is greater than about 2.5 nm, the substrate etching rate becomes limited by the FC film since it restricts the interaction of ions with the substrate[2.11]. The FC film thickness on SiC shows a strong decrease until 70% CO is added to C_4F_8/Ar:2/8, and a strong enhancement of the SiC etching rate is observed. For OSG and Si_3N_4 etched in C_4F_8/Ar:2/8 plasmas, the FC steady-state film thickness is much smaller than for SiC exposed to the same discharges. When 70% CO was added to C_4F_8/Ar:2/8 only a slight reduction of the FC film thickness was seen and little change in the OSG and Si_3N_4 etching rates was observed.

The changes of the FC steady-state film properties as a result of CO addition to C_4F_8/Ar can be explained by an increased degree of CO dissociation in the Ar-rich plasmas relative to C_4F_8/CO discharges. The mechanistic origin of these differences will be presented in the Discussion Section.

2.3.8. Correlation of Etching Selectivity and Surface Analysis Data

The ability of OSG to react with carbon species in the steady state fluorocarbon film is greater than Si_3N_4 or SiC. This is because the reactions between fluorocarbon and oxygen from SiO_2 with typical volatile reactions products like CO, CO_2, or COF_2, are more effective than reactions between fluorocarbon and nitrogen from Si_3N_4, resulting in the formation of volatile products such as FCN. In SiC etching, there is no volatile carbon containing compound that can be formed in reactions of fluorocarbon species and the substrates. Thus, the steady state fluorocarbon film thickness on OSG is thinner than for Si_3N_4 or SiC so that the etching selectivity of OSG/Si_3N_4 or OSG/SiC is mainly determined by the steady state FC thickness on Si_3N_4 or SiC. We saw in the previous sections that the steady state FC film thickness for OSG and Si_3N_4 substrates are small for C_4F_8/Ar discharges (<2.5 nm) and likely not etch rate limiting. In this case, the etching selectivity of OSG/Si_3N_4 is more likely gas chemistry dependent, rather than FC thickness dependent. On the other hand, the FC steady state films on Si_3N_4 in C_4F_8/CO discharges and on SiC in either C_4F_8/CO or C_4F_8/Ar/CO are relatively thick (>2.5 nm). When poly-Si and SiC substrates were etched in C_4F_8 and C_4F_8/Ar discharges, the steady-state FC film thickness was large, restricting the interaction of the plasma with the substrates, i.e. the ion-substrate interaction and fluorine atom interaction with the substrate. In this case, the FC steady-state film controls the etching rate for C_4F_8 and C_4F_8/Ar discharges. Adding CO to either C_4F_8 or C_4F_8/Ar reduces the FC film thickness for SiC and poly-Si substrates and reduces the etchant supply. In this case, the net effect will be a decrease of the etching selectivity of OSG/SiC or OSG/poly-Si

since the etch rate controlling factor for SiC and poly-Si is removed. Similarly, a decrease of OSG/Si_3N_4 etching selectivity is also observed when adding CO to C_4F_8.

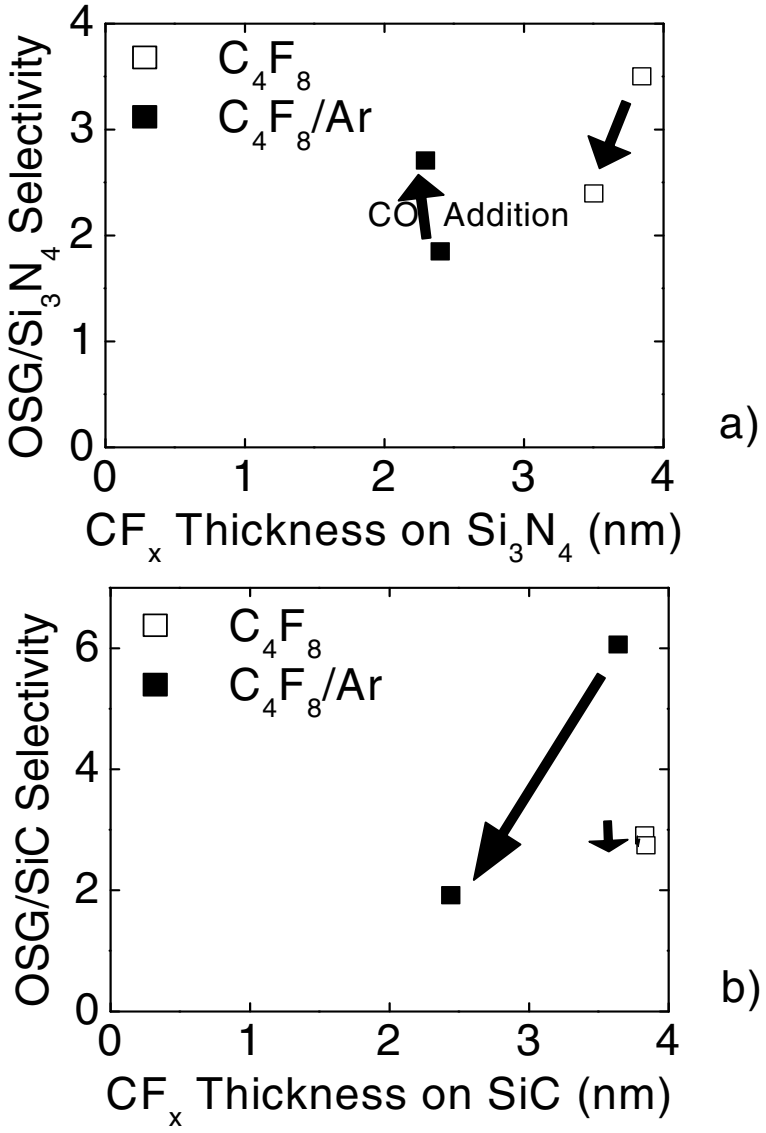

Fig. 2.9: Etching selectivity as a function of the steady state film thickness on (a) Si_3N_4 and (b) SiC etched by C_4F_8/CO and C_4F_8/Ar/CO. The other experimental parameters were: 600 W inductive power, 40 sccm gas flow and 6 mTorr.

The OSG/Si_3N_4 and OSG/SiC etching selectivities versus the FC steady-state film thicknesses on the Si_3N_4 and SiC substrates are plotted in Figs. 2.9 (a) and (b), respectively. The behavior shown in Figs. 2.9 (a) and (b) is completely consistent with the foregoing discussion. Only for C_4F_8 discharges is the Si_3N_4 etching rate limited by the FC film thickness (see Fig. 2.6 (a)). Only in this case, we observed a decrease of the etching selectivity of OSG/ Si_3N_4 as CO is added to C_4F_8. The etch rate of SiC is dominated by the fluorocarbon film thickness (see Fig. 2.6 (a)), and the OSG/SiC etching selectivity is strongly affected by the fluorocarbon film thickness. In the case of CO addition to C_4F_8, the steady state fluorocarbon thickness remains nearly constant, which results in a constant OSG/SiC etching selectivity (Fig. 2.9 (b)); when CO is added to C_4F_8/Ar, the steady state fluorocarbon thickness shows a strong decrease, which leads to the loss of the OSG/ SiC etching selectivity.

2.3.9. Discussion

1. Energy Level Diagram

Important electron induced excitation, dissociation and ionization energy thresholds for Ar[2.16], CO[2.16], and C_4F_8[2.17] are listed in the energy level diagram shown in Fig. 2.10. For CO and C_4F_8 the lowest energy levels of interest for this discussion are the energy thresholds for molecular dissociation. The dissociation thresholds presented in Fig. 2.10 are the minimum energies required for dissociation (thermal dissociation energies), and not the dissociation thresholds expected from an excitation from the ground state into a dissociating state. In the discharge molecules can be

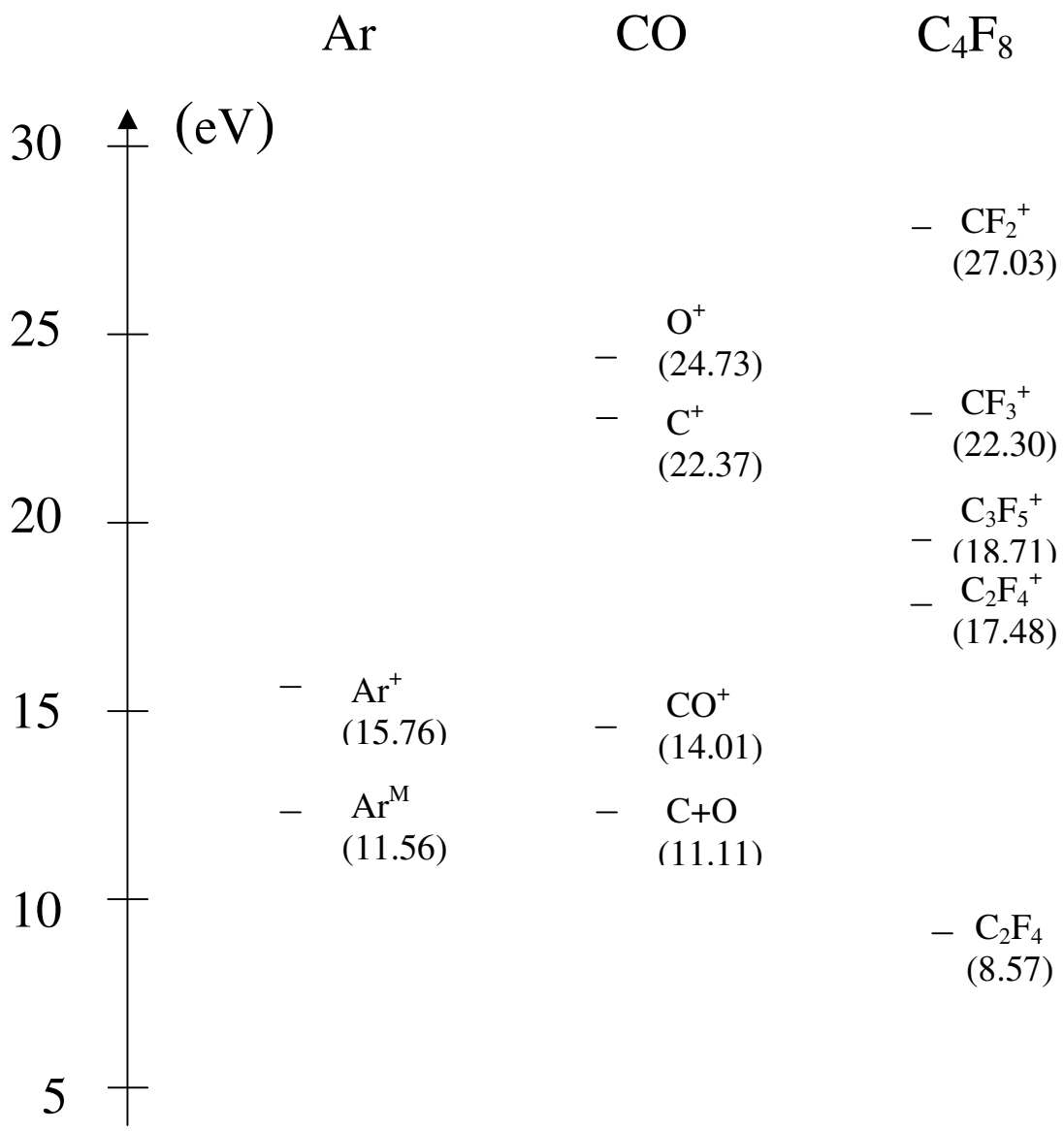

Fig. 2.10: Electron impact energy thresholds for Ar, CO and C_4F_8 dissociation and ionization. Ar^M: argon metastable. The 11.11 eV is the thermal dissociation threshold for CO, and that average electron impact dissociation energy is12.94 eV according to Liu et.al[2.18].

vibrationally excited, which will reduce the required energy. For instance, for CO 11.11 eV is the thermal dissociation threshold for CO. The average electron impact dissociation energy is12.94 eV according to Liu et.al[2.18], lower than the energy threshold from the ground state into the lowest energy dissociative state. Figure 2.10 shows that the molecular dissociation energy thresholds are below the energy required to produce Ar metastables.[2.16]

2.3.9.2. Pressure Effect

In Fig. 2.1, 2.2, and 2.4, we compared the ion current density, ion flux composition and deposition rate at pressures of 6 and 20 mTorr. Although the trends are similar, some differences do exist for the different pressures. The ion current density measured at 20 mTorr is lower than at 6 mTorr and the ion flux composition shows an important difference for C_4F_8/CO gas mixtures. The detailed analysis of the behavior shown requires a careful analysis of dissociation and ionization channels that exist in these discharges. The evolution of the data as a function of pressure can be interpreted roughly as follows: With increasing pressure, an electron energy distribution function results that is characterized by[2.19] a lower mean electron energy and a smaller high energy tail. The dissociation of CO is very sensitive to this change. A strong decrease in CO dissociation takes place as the pressure is increased, and can explain the strongly reduced C^+ flux measured at 20 mTorr relative to 6 mTorr pressure. Dissociation of C_4F_8 requires the least energy of all the processes shown in Fig. 2.10. As the electron energy distribution moves to lower energy, dissociation of C_4F_8 and ionization of FC radicals is favored relative to CO dissociation. This

explains why the FC radical flux is so large for C_4F_8/CO discharges at 20 mTorr. More of the available electron energy is expended for gas dissociation as the pressure is increased, resulting in a lower ion current density relative to lower pressures. This requires that the pressure of the molecular gas is sufficiently high, see the crossover of the curves in Fig. 2.1 (b).

2.3.9.3. C_4F_8/CO Discharges

When CO is added to C_4F_8, the lowest energy level of this gas mixture is occupied by the dissociation of C_4F_8, with C_4F_8 molecules also always being of a high density for the gas mixtures examined here. The applied power is channeled into C_4F_8 dissociation, and little CO dissociation takes place. This explains the lack of strong oxygen incorporation in the deposited carbonaceous films, even at 70% CO addition to C_4F_8. CO can interact with FC films being deposited through the reaction

$$CO + CF_x \rightarrow COF_y + CF_{x-y,} \qquad (1)$$

suggesting that CO extracts F from the deposited FC films, without becoming incorporated. This reaction may in part be responsible for the decrease of CF_2 shown in Fig. 2.3 (a). If a high CO percentage is used, the dissociation and ionization of CO cannot be neglected, and a reduced CF_x^+ ion flux and a decreased F/C ratio of the deposited film will result. A thinner, more carbon-rich steady-state FCO film should be formed on the partially etched samples, enabling an improved etching selectivity.

2.3.9.4. C_4F_8/Ar/CO Discharges

For Ar-rich C_4F_8/Ar gas mixtures, the collision processes of electrons with Ar, rather than dissociation of C_4F_8 become the factors that control the electron energy distribution. When CO is added to C_4F_8/Ar, we find from the energy level diagram of Fig. 2.10, that CO dissociation is one of the lower energy processes in this case. For the (C_4F_8/Ar:2/8)/CO gas mixture, CO dissociates at a much higher rate than for C_4F_8/CO. The atomic oxygen thus produced reacts with CF_x radicals at surfaces and produces COF_x[2.3] according to

$$CO \rightarrow C + O \uparrow \quad (2)$$

$$O + CF_x \rightarrow COF_x \uparrow \quad (3)$$

$$CO + CF_x \rightarrow C + COF_x \uparrow. \quad (4)$$

These reactions lead to a more carbon-rich FC film deposition on substrates without rf bias. In addition, some of the oxygen can be incorporated. These changes in the film stoichiometry explain the increase of the refractive index of the deposited carbonaceous films as the percentage of CO in C_4F_8/Ar/CO is increased. The same reaction should occur during rf biasing and etching of the substrate, thus producing thinner and more carbon-rich steady-state fluorocarbon films on the partially etched substrates. In addition, for Ar-rich gas mixtures, the reactions (2), (3) and (4) are expected to be enhanced by the increased ion flux seen for Ar-rich gas mixtures.

2.3.9.5. Pattern Transfer into OSG

OSG films were patterned with 300 nm Deep Ultra-Violet (DUV) photoresist and 80 nm bottom antireflection coating (BARC). The patterns were transferred using C_4F_8, C_4F_8/50%CO, C_4F_8/Ar:2/8, and (C_4F_8/Ar:2/8)/50%CO discharges maintained at

6 mTorr and 600 W source power. The gas flow during the etch was fixed at 40 sccm and the bias voltage was set at –100 V. Fig. 2.11 shows cross-sectional secondary electron micrographs of partially etched OSG films. The contrast between the features etched by the different gas discharges is clearly evident in the sidewall profiles and in the selectivity to the photoresist mask. The figures indicate that CO addition to C_4F_8 provides a higher degree of anisotropic etching compared with to pure C_4F_8.

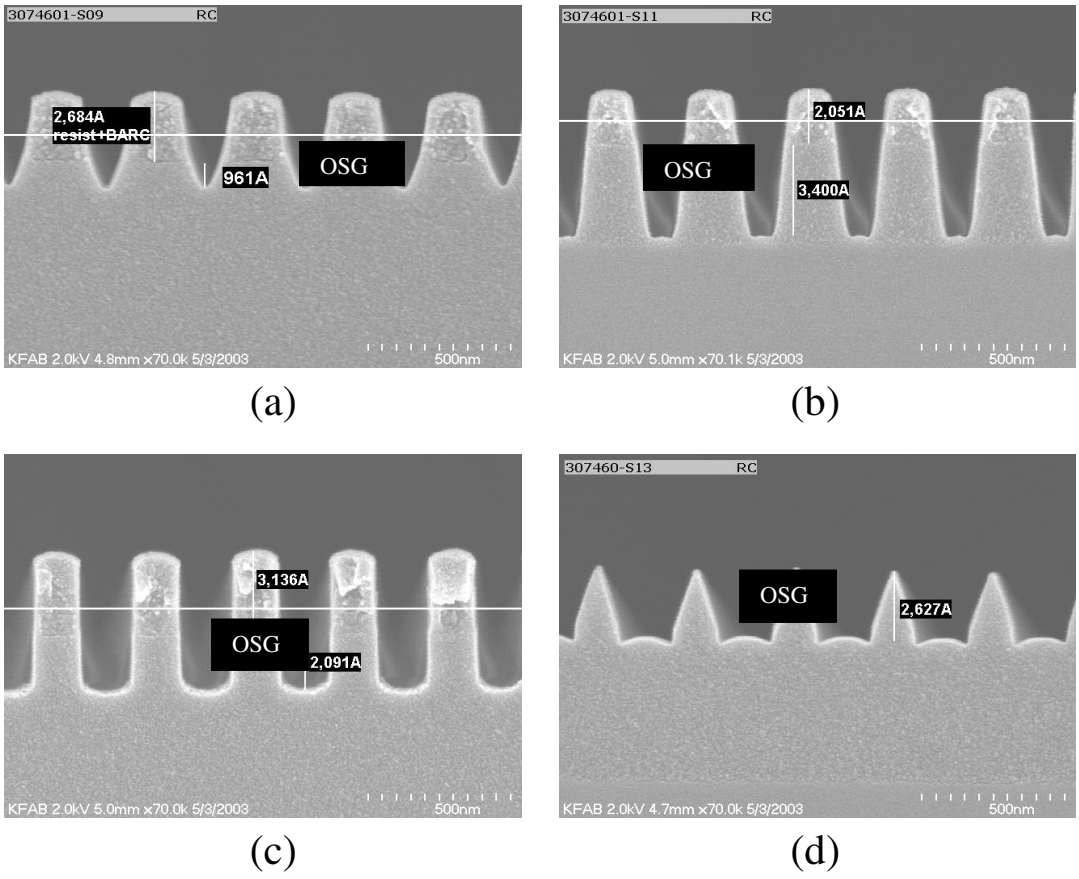

Fig. 2.11: Cross-sectional SEM photographs of patterned photoresist partially etched in pure (a) C_4F_8, (b) C_4F_8/50%CO, (c) C_4F_8/Ar:2/8, and (d) (C_4F_8/Ar:2/8)/50%CO. The other experimental parameters were: 600 W inductive power, 40 sccm gas flow, 6 mTorr and –100 V bias voltage.

C_4F_8/Ar:2/8 provides the best sidewall profile and highest etching selectivity of OSG/photoresist. This is partially attributed to the higher ion/neutral flux ratio (higher etching directionality) and an increase of the steady-state fluorocarbon thickness[2.12]. Due to high dissociation of CO in the Ar rich C_4F_8/Ar/CO discharges, the photoresist mask is completely removed for the (C_4F_8/Ar:2/8)/50%CO discharges and produces unacceptable pattern transfer.

2.4. CONCLUSION

The mechanisms for the changes in OSG/Si_3N_4 and OSG/SiC etching selectivity caused by CO addition to C_4F_8 and C_4F_8/Ar discharges were investigated. XPS surface analysis shows that a fluorocarbon film is present on all substrates during steady-state etching. The thickness of the film is strongly correlated with the etch rate of the substrate. The thickness of the fluorocarbon film is dependent on both the gas chemistry and the substrate materials. CO addition to C_4F_8 decreases the etch rates, primarily by dilution, and the etching selectivity of OSG relative to Si_3N_4 or SiC remains nearly constant. This is explained by the high stability of the CO molecule as compared to C_4F_8. CO addition to C_4F_8/Ar:2/8 has also been studied. For this Ar rich gas mixture, dissociation of CO is strongly increased. CO addition produces a reduced fluorine-content of fluorocarbon films, decreases the fluorocarbon film thickness, and leads to loss of the OSG/SiC selectivity seen for C_4F_8/Ar discharges. The energy thresholds of electron induced excitation, dissociation and ionization in the C_4F_8/CO and C_4F_8/Ar/CO gas mixtures can be used to explain qualitatively all of the observations. The present work illustrates clearly the important

chemical consequences induced by the addition of a noble gas to a reactive molecular gas mixture.

ACKNOWLEDGEMENTS

Financial support of this work by the Semiconductor Research Corporation is gratefully acknowledged. The authors also would like to thank Texas Instruments, Inc., Dallas, TX, USA for support and supply of the thin film materials used in this work.

Chapter 3: Investigation of Surface Modifications of 193 nm and 248 nm Photoresist Materials During Low-Pressure Plasma Etching

J. Vac. Sci. Technol. A., 22,2594 (2004)

L. Ling, X. Hua, X. Li, G. S. Oehrlein, E. A. Hudson, P. Lazzeri and M. Anderle

Abstract:

Plasma-based pattern transfer of lithographically produced nanoscale patterns in advanced photoresist materials is often accompanied by photoresist surface roughening and line edge roughening due to factors which are not well understood. We have studied the evolution of surface roughening in prototypical 193 nm and 248 nm photoresist materials during plasma processing as a function of plasma operating parameters. We used real-time ellipsometry and mass spectrometry, along with atomic force microscopy, x-ray photoemission spectroscopy and time-of-flight secondary ion mass spectrometry in an effort to understand the morphological and chemical changes of the photoresist materials as a function of plasma-surface interactions parameters, e.g. maximum ion energy, total energy flux, and plasma chemistry, and photoresist material. A comparison of 248 nm photoresist with 193 nm photoresist shows that significantly more surface roughness is introduced in the 193 nm photoresist for most plasma processing conditions investigated. We also find a dramatic dependence of surface roughening on the chemistry of the plasma process, e.g. for Ar/C_4F_8 a modified photoresist surface layer with an extent of about 50 nm is produced in 193 nm photoresist, whereas for C_4F_8 discharges the surface modification

is much less for otherwise similar conditions. We show that one important reason for these differences may be ion-enhanced selective volatilization of carbonyl groups of the 193 nm photoresist polymer backbone which is absent for the 248 nm material, along with modulation of the ion-interaction with the photoresist material by fluorocarbon surface passivation.

3.1. INTRODUCTION

Currently, 193 nm lithography is being introduced for manufacturing of integrated circuits featuring devices with sub-0.13 μm critical dimensions[3.1, 3.2]. Lithography at 193 nm wavelength requires photoresist materials that are thinner than 248 nm photoresist materials, and consist of a different polymer backbone exhibiting less absorption at 193 nm than the 248 nm photoresist materials[3.1, 3.2]. The decrease of the thickness of 193 nm photoresist materials requires higher plasma etching resistance relative to 248 nm photoresist materials. The polymer backbone used for 193 nm photoresist is much different from 248 nm photoresist[3.3, 3.4], leading to new challenges in the interaction of plasma etch processes with the photoresist material. One issue with 193 nm photoresist materials in plasma etching environments is increased surface roughness as a result of the etch process. Surface roughness can produce roughness of feature sidewalls that can be transferred into the films being etched[3.5-3.13].

In this work, the plasma etching behavior of 193 nm and 248 nm photoresist is examined in fluorocarbon discharges used for dielectric etching. We performed etch rate measurements and etch product analysis during the etching process, along with the surface analysis after the etching, and identified an important mechanism that correlates with the enhanced introduction of surface roughness seen for the 193 nm photoresist material.

3.2. EXPERIMENTAL

The transformer coupled plasma (TCP) reactor used in this work has been described in earlier articles of this group[3.14]. All experiments described here were carried out in discharges at pressures ranging from 6 to 10 mTorr, and maintained using 400 to 600 W source power at 13.56 MHz (we studied Ar and oxygen discharge at reduced power level due to the following facts: 1) the ion current density is much higher in Ar discharges than for C_4F_8 discharges; 2) the etch rate of photoresist is very high in a pure O_2 600 W plasma, and reduced at lower source power). Discharges produced using C_4F_8, C_4F_8/Ar, Ar or O_2 at total gas flows of 40 sccm were studied. The ion energy at the wafer can be controlled independently of the plasma generation by a variable frequency (0.4-40 MHz) rf power supply (0-300 W). For this study the rf frequency was fixed at 3.7 MHz, and the rf bias power was varied up to 250 W. The self-bias voltage was measured during the experiments, and for certain experiments self-bias voltage rather than rf bias power was controlled.

Etching rates, surface morphological and chemical changes of two kinds of blanket photoresist films were studied. The 248 nm photoresist (Shipley UV6) is based on aromatic groups and shown in Fig. 3.1. The 193 nm photoresist is a polymethylmethacrylate backbone with lactone- and adamantine-based substituents.

A rotating compensator ellipsometer in the polarizer-compensator-sample-analyzer (PCSA) configuration with a 632.8 nm He/Ne laser was used to determine thin film etching rates and the introduction of surface modifications in real time. In order to detect etch products, the sampling orifice of a mass spectrometer (MS) was positioned above the photoresist samples during the process. The electron-impact ionizer of the mass spectrometer was set at 30 eV. Chamber conditions were carefully

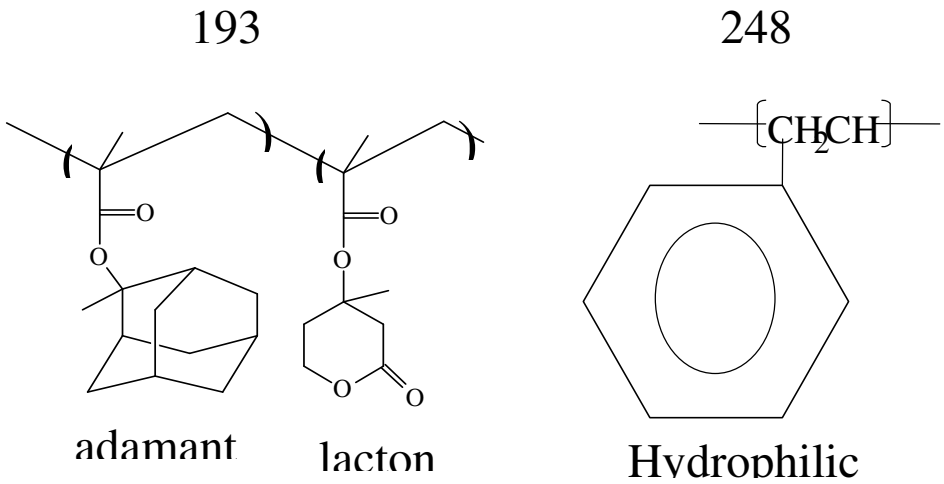

Fig. 3.1: Chemical structures of 193 nm and 248 nm photoresist materials.

controlled to rule out effects of processing history on the results obtained. The plasma etched samples used for the Atomic Force microscopy (AFM), x-ray photoelectron spectroscopy (XPS) and time of flight secondary ion mass spectrometry (ToF-SIMS) studies were etched at least 1 minute to achieve steady-state surface conditions. Surface roughness is studied by the Digital Instruments (DI) dimension 3000 Scanning Probe Microscopy (SPM). Samples of 2.5×2.5 cm^2 size were transferred to the XPS chamber to determine changes in surface composition. These measurements were performed at a 90^o detection take-off angle using a non-monochromatized Mg K-alpha X-ray source (1253.6 eV). For the ToF-SIMS analysis, a 25 keV pulsed Ga^+ primary beam was used. Static SIMS (SSIMS) spectra[3.15] were acquired for both detection polarities (positive and negative secondary ions were detected), by sampling

an area of 150 μm x 150 μm in size. The mass resolution using these experimental conditions was greater than 5500 at m/z of 31.

3.3. RESULTS AND DISCUSSION

3.3.1. Comparison of C_4F_8 and C_4F_8/90%Ar Discharges

Table 3.1 summarizes the properties of C_4F_8 and C_4F_8/90%Ar discharges from the previous work of this group[3.16, 3.17]. The addition of Ar increases the importance of ion bombardment relative to neutral and direct reactive ion etching. This is supported by the comparison of CF_2 flux and ion flux in both pure C_4F_8 and Ar rich gas discharge. In the latter case, the CF_2 flux, which is the main neutral radical in C_4F_8/90%Ar discharges, is about one order of magnitude less and the total ion flux is about 5 times larger relative to C_4F_8. Ion flux composition analysis shows that the ion composition changes from $C_xF_y^+$ dominant to Ar^+ dominant. These suggest that increasing Ar changes the etching process from ion-limited to neutral-limited.

	C_4F_8	C_4F_8/90%Ar
CF_2 Flux (mL/s)	>4000	<500
Total Ion Flux (mL/s)	~130	~700
Ion Species	100%$C_xF_y^+$	>70%Ar^+

Table 3.1: Comparison of C_4F_8 and C_4F_8/90%Ar discharges[3.16, 3.17]

3.3.2. Etch Resistance

Average etch rates of both 193 nm and 248 nm photoresist materials in C_4F_8, C_4F_8/Ar and Ar are presented in Fig. 3.2. For these etching experiments, the self-bias voltage was fixed at –100 volts. For 193 nm photoresist, the maximum etch rate was obtained in C_4F_8/90%Ar plasmas. For 248 nm photoresist, the maximum erosion rate was obtained in pure Ar. For both materials, the minimum etch rate is observed for pure C_4F_8 plasmas. For pure C_4F_8 a thicker fluorocarbon layer is formed on the photoresist surfaces for these conditions during steady-state etching. Figure 3.2 shows that for all plasma operating conditions examined, the etch rate of 193 nm photoresist material is higher than that of 248 nm photoresist. The simplest explanation for these differences is related to the fact that the polymer backbone of the 193 nm photoresist is non-aromatic and with easier bond-breaking in the plasma. This effect can be enhanced by oxygen bonded carbon atoms that are of higher number density for the 193 nm material[3.18, 3.19] and carbonyl groups[3.7] (see Fig. 3.1).

3.3.3. Time Dependent Etch Rates and Changes in Photoresist Optical Properties

The photoresist etching rates were found to be time-dependent. This is shown in Fig. 3.3 (a) for the two types of photoresists and different plasma operating conditions. For each experiment, all controllable parameters were kept constant and the photoresist films were completely removed. The etch rate of the 193 nm photoresist increased initially, then decreased after about half of the film was removed. For 248 nm photoresist, the etch rate increased continuously in C_4F_8/Ar discharges and decreased continuously in C_4F_8 discharges.

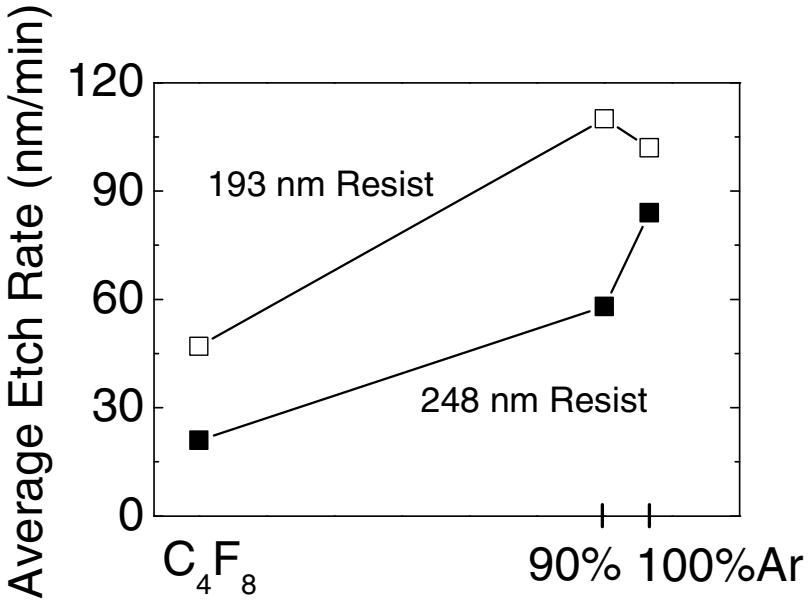

Fig. 3.2: Average etch rates of blanket 193 nm and 248 nm photoresists measured in C_4F_8, C_4F_8/90%Ar and Ar using in-situ ellipsometry. The other experimental parameters were used: For C_4F_8, C_4F_8/90%Ar discharge, 600 W inductive power, 40 sccm gas flow, 10 mTorr and –100 V bias voltage; For Ar discharge, 400 W inductive power, 40 sccm gas flow, 6 mTorr and –100 V bias voltage.

A comparison of the time dependence of the refractive index of 193 nm and 248 nm photoresists is presented in Fig. 3.3 (b). The refractive index of 248 nm photoresist remains nearly constant throughout an etching experiment. The refractive index of 193 nm photoresist remains nearly constant in a pure C_4F_8 discharge, but shows a strong decrease for a C_4F_8/90%Ar discharge. This change of the optical properties of the photoresist may be explained by the continuous surface and bulk

modification of the 193 nm photoresist in the C_4F_8/Ar discharge, and will be discussed later.

.

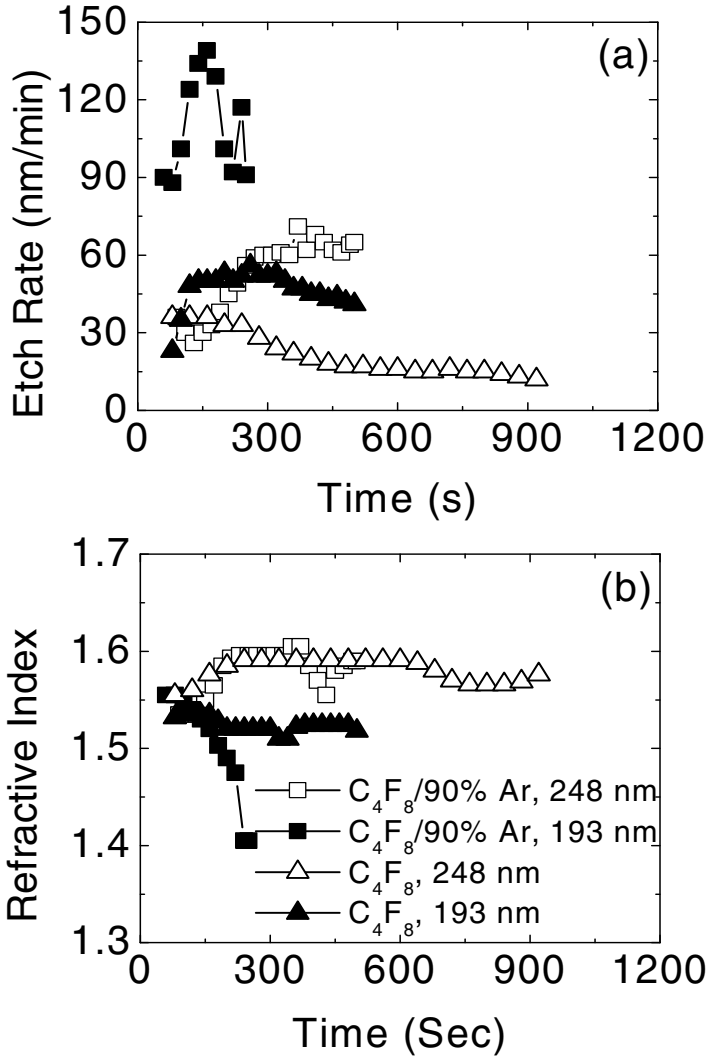

Fig. 3.3: Dependence of (a) etch rates and (b) refractive index of blanket 193 nm and 248 nm photoresists on time in C_4F_8 and C_4F_8/90%Ar measured using *in-situ* ellipsometry. The other experimental parameters were: 600 W inductive power, 40 sccm gas flow, 10 mTorr and –100 V bias voltage.

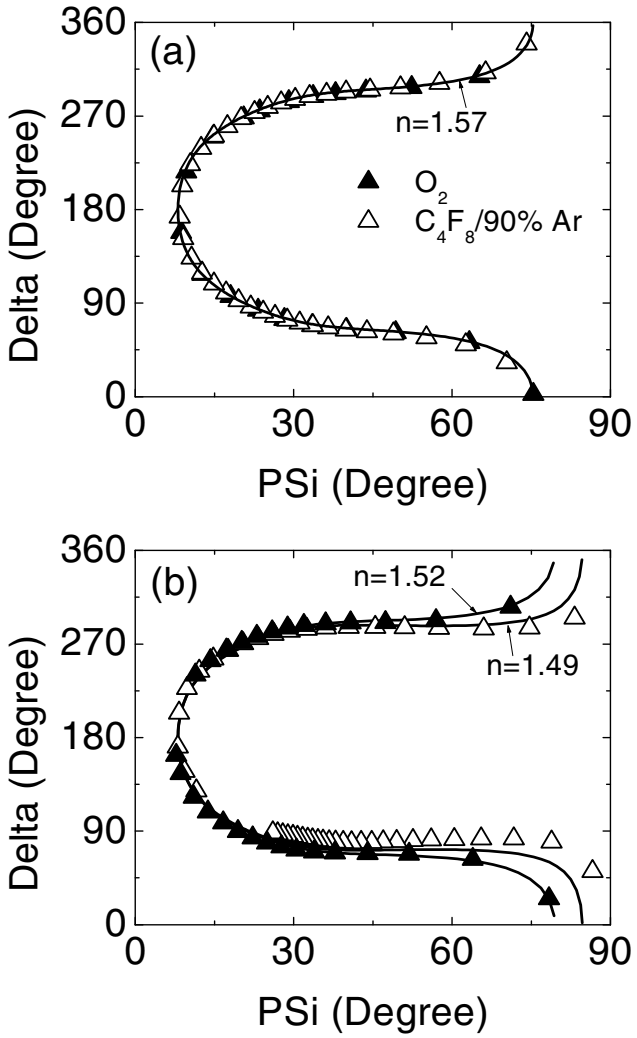

Fig. 3.4: Ellipsometry data of (a) 248 nm and (b) 193 nm photoresist etched in O_2 and C_4F_8/90%Ar. The experimental parameters were: For O_2 discharge: 400 W inductive power, 40 sccm gas flow, 6 mTorr, no bias. For C_4F_8/90%Ar discharge: 600 W inductive power, 40 sccm gas flow, 10 mTorr and –100 V bias voltage.

3.3.4. Real-time Ellipsometry Characterization

To illustrate more clearly the change of the optical properties of the photoresist films as a function of time during the plasma process, the real-time Ψ and

Δ ellipsometry data (wavelength of 632.8 nm) obtained during plasma etching are plotted in Fig. 3.4. Data are shown for both O_2 and C_4F_8/90%Ar discharges. Superimposed on the experimental data are model curves that were calculated using a one-layer optical model utilizing the program of McCrackin[3.20]. The refractive index of the thin fluorocarbon film that exists on the photoresist surface was treated as an adjustable parameter. The values of the parameters used in the model were an experimental angle of incidence of 70^0, and the refractive index of Si substrate was chosen as 3.866-i0.028.

Figure 3.4 (a) shows that for 248 nm photoresist the ellipsometry data obtained for both gas chemistries are nearly the same, and can be fitted with a refractive index of 1.57. For 248 nm photoresist the effective refractive index remains constant during the plasma etching process. Equivalent data are shown in Fig. 3.4 (b) for 193 nm photoresist etched in either O_2 or C_4F_8/90%Ar. In this case the curves obtained in O_2 and C_4F_8/90%Ar differ strongly. In addition, whereas the Ψ and Δ data obtained during O_2 plasma etching can be described by a constant refractive index, this is not the case for the data obtained with C_4F_8/90%Ar. In this case, a continuously changing refractive index of the photoresist material is required.

The model used for the initial analysis is a one-layer optical model, which just considers a single film on a substrate. The refractive index of this film is adjusted to fit the data, and physically corresponds to a modification of the photoresist surface and bulk. A more accurate way to describe the changes of the photoresist film during etching is to use a two-layer optical model. This is shown in the inset of Fig. 3.5 (a).

In this model the photoresist near-surface region is represented by a damaged layer. The parameters of this layer (refractive index, thickness) are

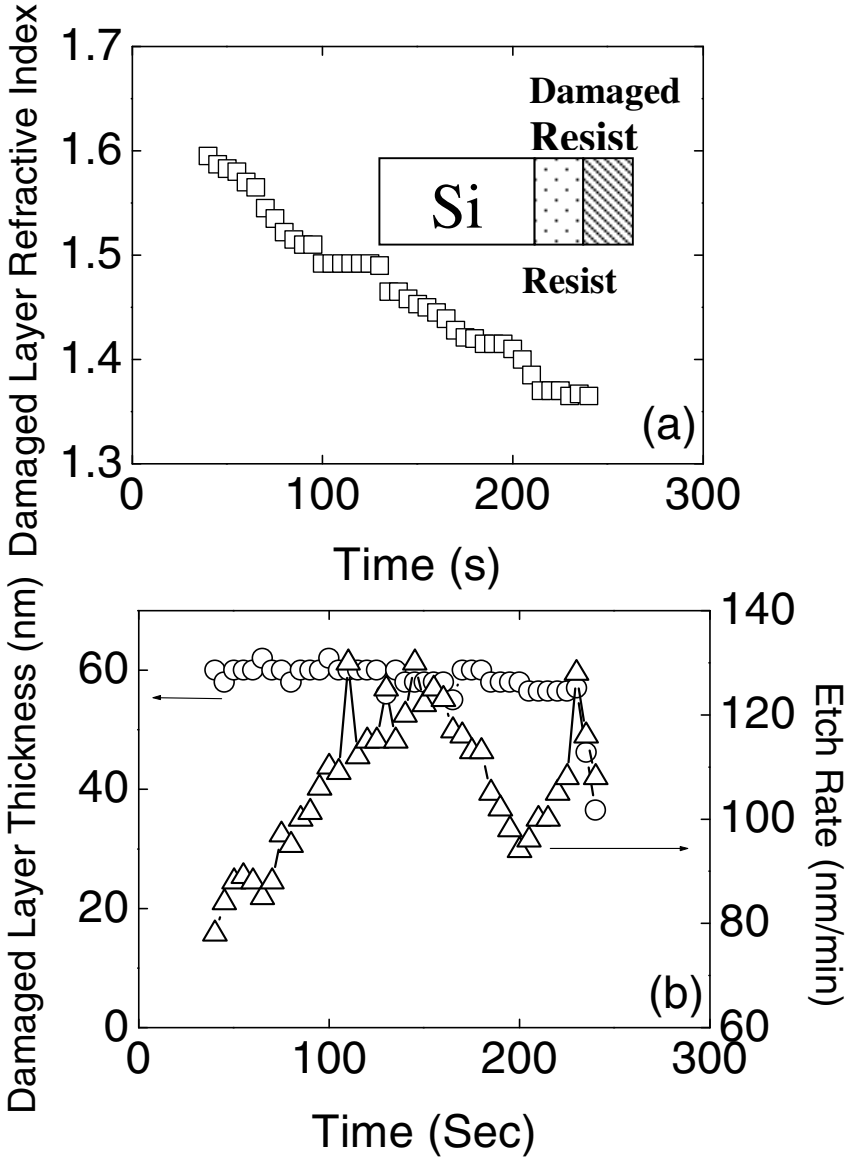

Fig. 3.5: Dependence of (a) damaged layer refractive index and (b) damaged layer thickness and etch rates of 193 nm photoresist on time and analyzed by two layer optical model. The other experimental parameters were: C_4F_8/90%Ar, 600 W inductive power, 40 sccm gas flow, 10 mTorr and –100 V bias voltage.

free to change during etching process. The layer underneath represents the bulk photoresist material. The refractive index of this layer is assumed to remain the same during the plasma etching process. Physically, it is reasonable to assume that two distinct regions exist for the photoresist film. For the near-surface region of the photoresist we can assume that enhanced loss of oxygen may take place, and simultaneously fluorine penetration will occur. For instance, the dry-etching resistance of organic polymers has often been related to the carbon-atom-density (Ohnishi parameter) [3.16, 3.17], and enhanced removal of oxygen atom as compared to carbon atoms. For the 193 nm photoresist material we expect loss of oxygen atoms, and fluorine penetration into the near-surface region. Introduction of surface roughness also will change the optical properties of the top layer. These effects are apparently enhanced in Ar-rich fluorocarbon plasma, producing stronger surface modifications in this case. The changing composition and morphology of the damaged surface layer produces a refractive index that changes as a function of time. In addition, the thickness of the damaged layer can change as a function of time, the importance of which can be examined by modeling.

The results of analyzing the ellipsometric data obtained during C_4F_8/90%Ar plasma etching of 193 nm photoresist with this two-layer optical model are shown in Figs. 3.5 (a) and (b). The required refractive index of the bulk photoresist film is 1.52 and consistent with the value obtained during O_2 plasma etching of the 193 nm photoresist. Figure 3.5 (a) shows that the refractive index of the damaged layer decreases monotonically with time. This can be explained by either fluorine

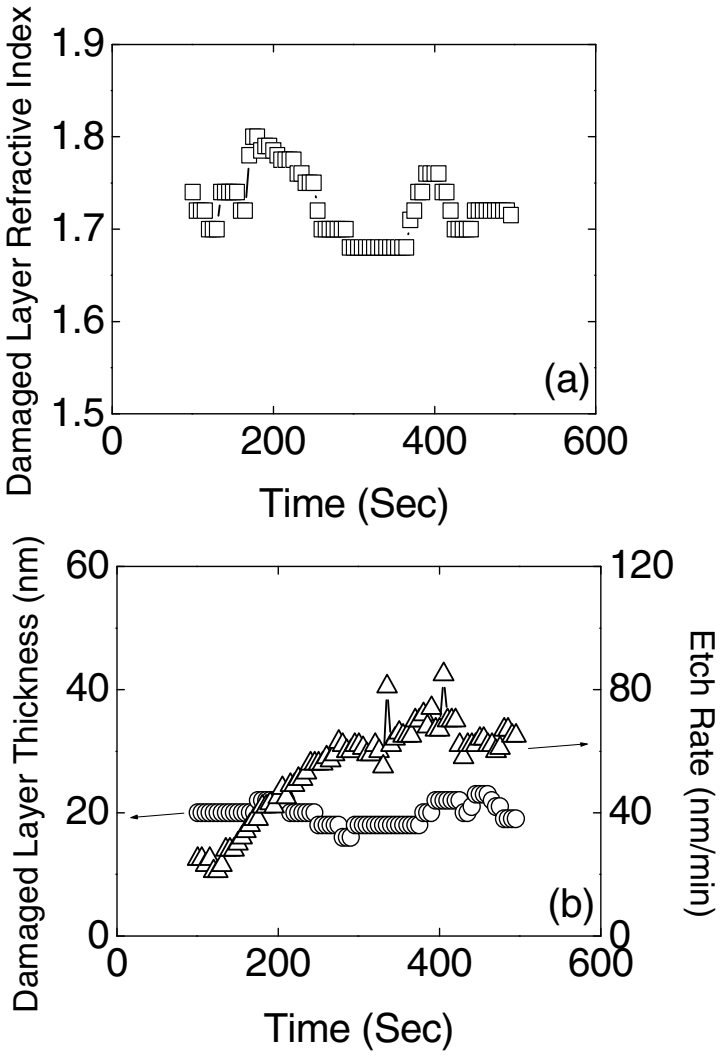

Fig. 3.6: Dependence of (a) damaged layer refractive index and (b) damaged layer thickness and etch rates of 248 nm photoresist on time and analyzed by two layer optical model. The other experimental parameters were: C_4F_8/90%Ar, 600 W inductive power, 40 sccm gas flow, 10 mTorr and –100 V bias voltage.

penetration into the photoresist, increased photoresist surface roughness of the photoresist or both. Figure 3.5 (b) shows the thickness of the damaged layer as a function of time. It is nearly constant for most of the plasma exposure. The thickness

value is comparable to the damaged layer thickness measured by AFM (see below). Towards the end of the plasma etching process, the damaged layer thickness decreases. This occurs once the undamaged photoresist film has been completely removed, and the damaged layer thickness becomes equal to the total film thickness. Figure 3.5 (b) also shows the photoresist etching rate obtained from this analysis, and is consistent with the value obtained from the one-layer optical model.

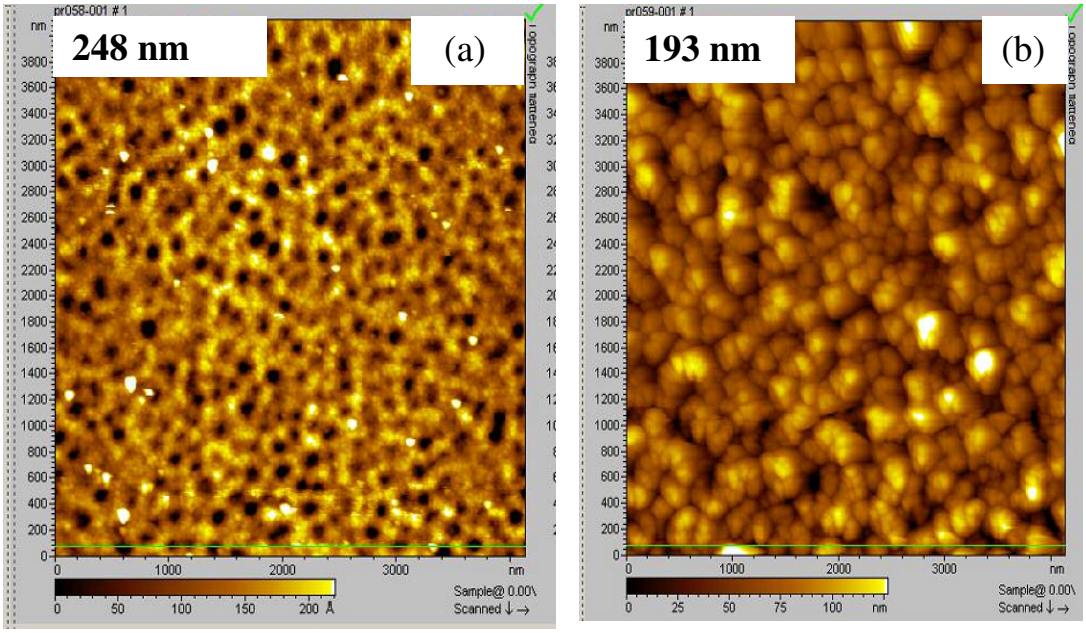

Fig. 3.7: AFM photographs of blanket (a) 193 nm and (b) 248 nm photoresist partially etched in C_4F_8/90%Ar. The other experimental parameters were: 600 W inductive power, 40 sccm gas flow, 10 mTorr and –100 V bias voltage.

Equivalent results of analyzing 248 nm photoresist data (also measured during C_4F_8/90%Ar plasma etching) are shown in figures 3.6 (a) and (b). The most significant difference is that the refractive index of the damaged layer is slightly

greater than seen for the undamaged 248 nm photoresist (see Figure 3.6 (a)). The refractive index of bulk film is 1.57, consistent with the value obtained during O_2 plasma exposure. Figure 3.6 (b) shows the thickness of the damaged photoresist layer as function of time. The thickness of the slightly modified layer remains nearly constant during plasma processing, and is much smaller than that measured for the 193 nm photoresist. Figure 3.6 (b) also shows the time-dependent etching rate of the 248 nm photoresist that is consistent with the value obtained by one-layer optical modeling.

3.3.5. Surface Roughness Analysis by AFM

The morphology of photoresist films after plasma etching was examined by Atomic Force Microscopy (AFM). After plasma processing, in particular C_4F_8/90%Ar discharges, severe surface roughening was observed for the 193 nm material. This is shown in Fig. 3.7, where AFM images of 193 nm material are compared with 248 nm photoresist after the same C_4F_8/90%Ar etching process (selfbias voltage of – 100 V). The scale of the uniformly distributed surface roughness is by one order of magnitude greater for the 193 nm material than for the 248 nm photoresist.

In Fig. 3.8, the results of surface roughness measurements of both types of photoresists before and after plasma processing are compared. A smooth surface is observed for the virgin samples, with a RMS roughness of about 0.2-0.3 nm. These values are consistent with data of similar measurements by Kwong et. al[3.21]. In Fig. 3.8, the surface roughness parameters RMS, R_a and R_{max} measured by AFM are

compared for both types of photoresists after Ar, C_4F_8 and C_4F_8/90%Ar treatments. Here RMS (root mean square) is the standard deviation of the Z values within a given area, R_a (mean roughness) represents the arithmetic average of the deviations from the center plane and R_{max} is the difference in height between the highest and lowest points on the surface relative to the mean plane. The same selfbias voltage of – 100 V was applied in each case. In general, more severe surface roughness is observed for the 193 nm photoresist material than for the 248 nm photoresist material. For 193 nm photoresist, gas chemistry plays an important role in producing the surface roughness. Severe surface roughening is seen after both Ar sputtering and etching in an Ar-rich fluorocarbon discharge. On the other hand, little surface roughness is observed after etching in pure C_4F_8. Additional surface analysis of the photoresist films by X-ray photoemission analysis but not shown here has revealed that for C_4F_8 the photoresist surface is covered by a fairly thick (~ 2nm) fluorocarbon film. For 248 nm photoresist little dependence on discharge chemistry is observed. We will discuss the origin of the surface roughness in the Discussion Section.

3.3.6. Surface Analysis of Partially Etched Samples Using XPS

The effect of oxygen in photoresist materials has often been related to low plasma etching resistance[3.18, 3.19]. The presence of reactive oxygen containing groups in the 193 nm photoresist, e.g. carbonyl groups (see Fig. 3.1), may contribute to the higher etching rate and introduction of surface roughness in that material, in contrast to the 248 nm photoresist which does not show this group[3.22, 3.23]. To explore the fate of carbonyl groups during the plasma etching processes, we analyzed untreated and

partially etched 193 nm and 248 nm photoresist materials by X-ray photoelectron spectroscopy (XPS). We paid particular attention to the fine structure of the carbon 1s and oxygen 1s core levels which provide information on the carbonyl group. 193 and 248 nm photoresist samples were etched for 1 minute using a selfbias voltage of –100 V employing either Ar or C_4F_8/90%Ar discharges. For the pure Ar discharge the RF source power was 400 W, whereas for the C_4F_8/90%Ar it was 600 W. For photoresist samples etched in pure C_4F_8 the fluorocarbon overlayer is too thick to allow differentiation of the photoresist material underneath by XPS.

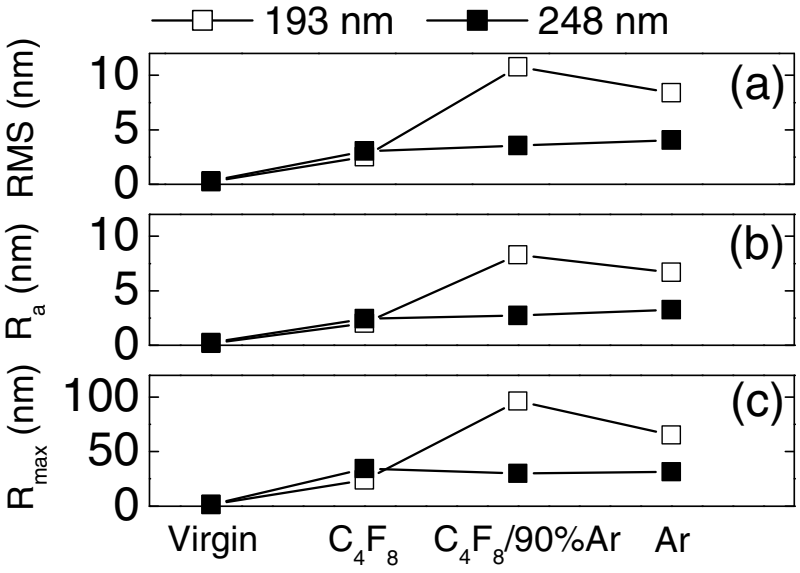

Fig. 3.8: RMS, R_a and R_{max} of partially etched blanket 193 nm and 248 nm photoresist measured by AFM. The other experimental parameters were: 600 W inductive power, 40 sccm gas flow, 10 mTorr and –100 V bias voltage.

Figures 3.9 and 3.10 show the C (1s) and O (1s) photoemission spectra of the untreated and plasma etched photoresist samples, respectively. The untreated 193 nm photoresist shows clearly two peaks in the C 1s region of the spectrum. These are identified as being due to C-C and C=O bonding, respectively. For the untreated 248 nm photoresist material the C=O peak is absent in the C 1s spectrum. Figures 3.9 (b) and 3.10 (b) show that Ar plasma etching eliminated the carbonyl peak at 288 eV for the 193 nm photoresist. Similarly, after C_4F_8/90%Ar plasma etching the carbonyl peak was absent in the C 1s spectrum of the 193 nm photoresist (see Fig. 3.9 (c)). For the C_4F_8/90%Ar gas chemistry, a thin steady state fluorocarbon film is formed on the surface of the photoresist film, which leads to the presence of weak fluorocarbon peaks in the high energy region of the C 1s spectrum. Fluorocarbon film formation is also apparent for the 248 nm photoresist material after C_4F_8/90%Ar etching. In general, the C 1s spectra of the 193 nm and 248 nm photoresist films are nearly identical after etching in Ar and C_4F_8/90%Ar discharges, indicative of similar surface chemistry.

The presence of oxygen in the photoresist materials can also be followed in the O 1s region of the XPS spectrum. In this case the presence of C=O for the 193 nm material does not introduce an easily recognizable peak, but gives rise to a greater overall O 1s intensity than for the 248 nm photoresist. The O 1s peak intensities are reduced after Ar and C_4F_8/90%Ar plasma etching. It is interesting to see a greater level of O 1s reduction resulting from C_4F_8/90%Ar etching for 248 nm photoresist than for 193 nm photoresist. We also observed in this case that the C 1s and F 1s (not

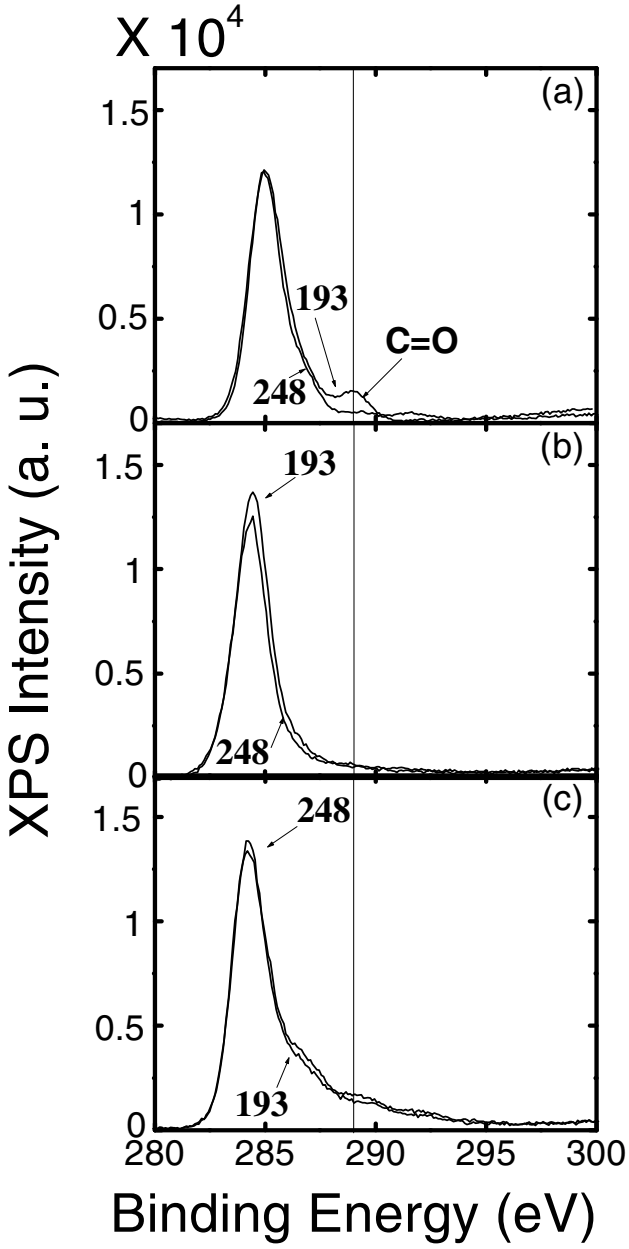

Fig. 3.9: C (1s) photoemission spectra of (a) untreated and partially etched 193 nm and 248 nm photoresist films produced in (b) Ar and (c) C_4F_8/90%Ar discharge. The other experimental parameters were: For Ar discharge, 400 W inductive power, 40 sccm gas flow, 6 mTorr and –100 V bias voltage; for C_4F_8/90%Ar discharge, 600 W inductive power, 40 sccm gas flow, 10 mTorr and –100 V bias voltage.

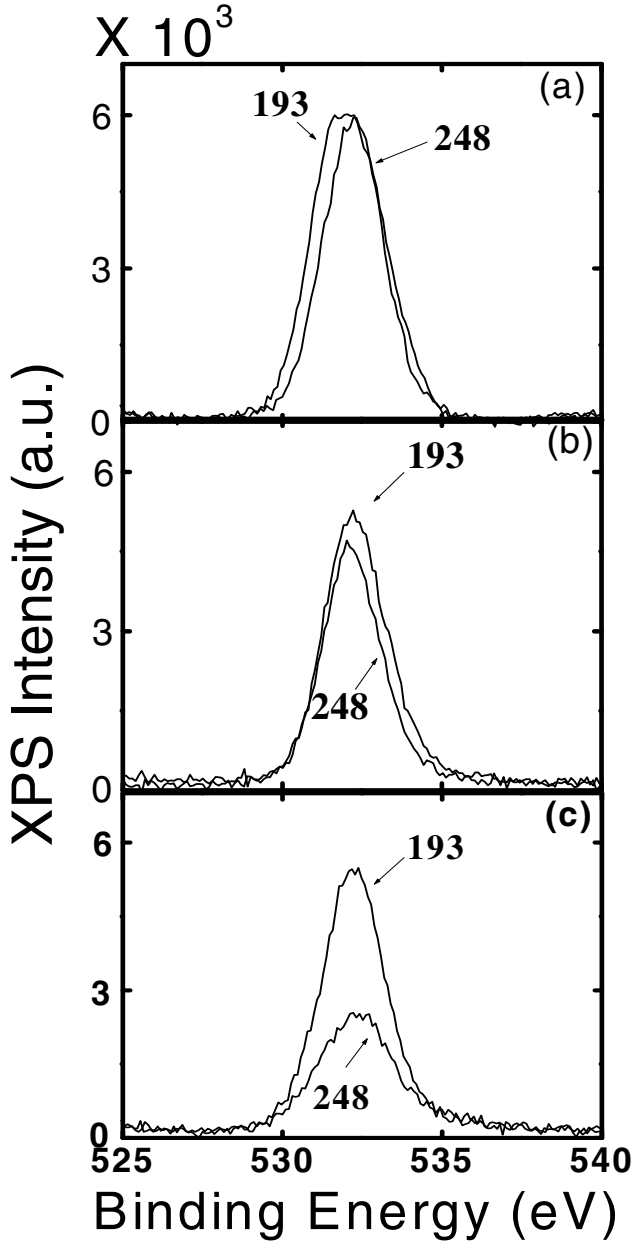

Fig. 3.10: O (1s) photoemission spectra of (a) untreated and partially etched 193 nm and 248 nm photoresist films produced in (b) Ar and (c) C_4F_8/90%Ar discharge. The other experimental parameters were: For Ar discharge, 400 W inductive power, 40 sccm gas flow, 6 mTorr and –100 V bias voltage; for C_4F_8/90%Ar discharge, 600 W inductive power, 40 sccm gas flow, 10 mTorr and –100 V bias voltage.

shown here) peaks of both photoresists are very similar for this etching gas chemistry. The enhanced O 1s peak for the 193 nm resist film indicates a much larger effective surface area on the 193 nm photoresist that is being examined by XPS. It indicates that the origin of the different behavior of the O 1s peak for the 193 nm material is related to the fact that the surface topography of the 193 nm is much rougher than for the 248 nm material after this etching treatment, which is expected to affect the XPS measurement. This is consistent with previous observation by AFM.

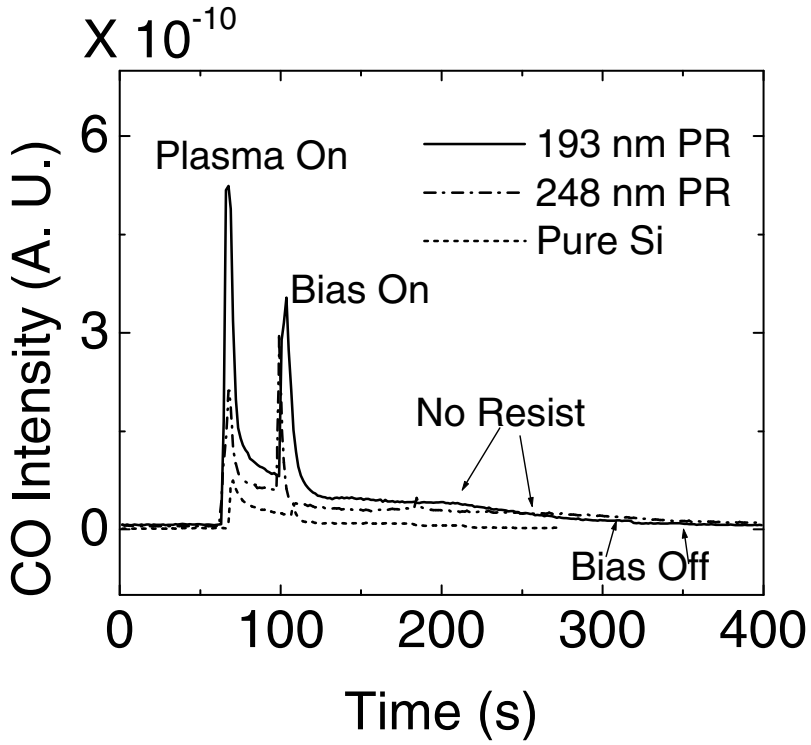

Fig. 3.11: Dependence of CO intensity on processing time in C_4F_8/90%Ar produced by 193 nm, 248 nm photoresist and by background. The other experimental parameters were: 600 W inductive power, 40 sccm gas flow, 10 mTorr and –100 V bias voltage.

3.3.7. Etch Products Analysis by MS

We attempted to follow the removal of CO during the plasma treatment using real time mass spectrometry. Figure 3.11 shows the CO^+ mass spectrometer signal during the etching of 193 nm and 248 nm photoresists. For reference, the real time trace obtained with a Si substrate is also shown. The latter was used to obtain information on the CO background level, e.g. etching of the quartz coupling window can contribute CO to the discharge[3.24]. Initially, the photoresist films are etched in pure Ar discharges without applying a bias to the substrate. High CO^+ levels are observed for both types of photoresist films, but the CO^+ intensity of the 193 nm photoresist material is about 2.5 times higher than for the 248 nm photoresist film, and both are above the CO^+ background level. This difference in CO^+ signal was reproducible, and indicates that volatile CO species can be more easily formed for the 193 nm photoresist than for the 248 nm material during low energy ion bombardment of the photoresist surfaces (Ar^+ ions with an energy corresponding to the plasma potential (~20 eV) bombard the photoresist surfaces during this part of the process.) A strong decrease of the CO^+ intensity is subsequently observed and the CO^+ signals attain a nearly constant level. This level is higher for the 193 nm photoresist than for the 248 nm material and the levels correspond to steady-state etching of both photoresist materials for these conditions. In the second step, a selfbias voltage of –100 V is applied to the photoresist surfaces. This gives rise to another peak of the CO^+ as a function of time. The CO^+ increase can be explained by the higher ion energies that will produce enhanced etching and plasma-surface interactions with

deeper-lying regions of the photoresist films. Upon complete removal of the photoresist films, the CO^+ intensities decrease to the background CO^+ signal.

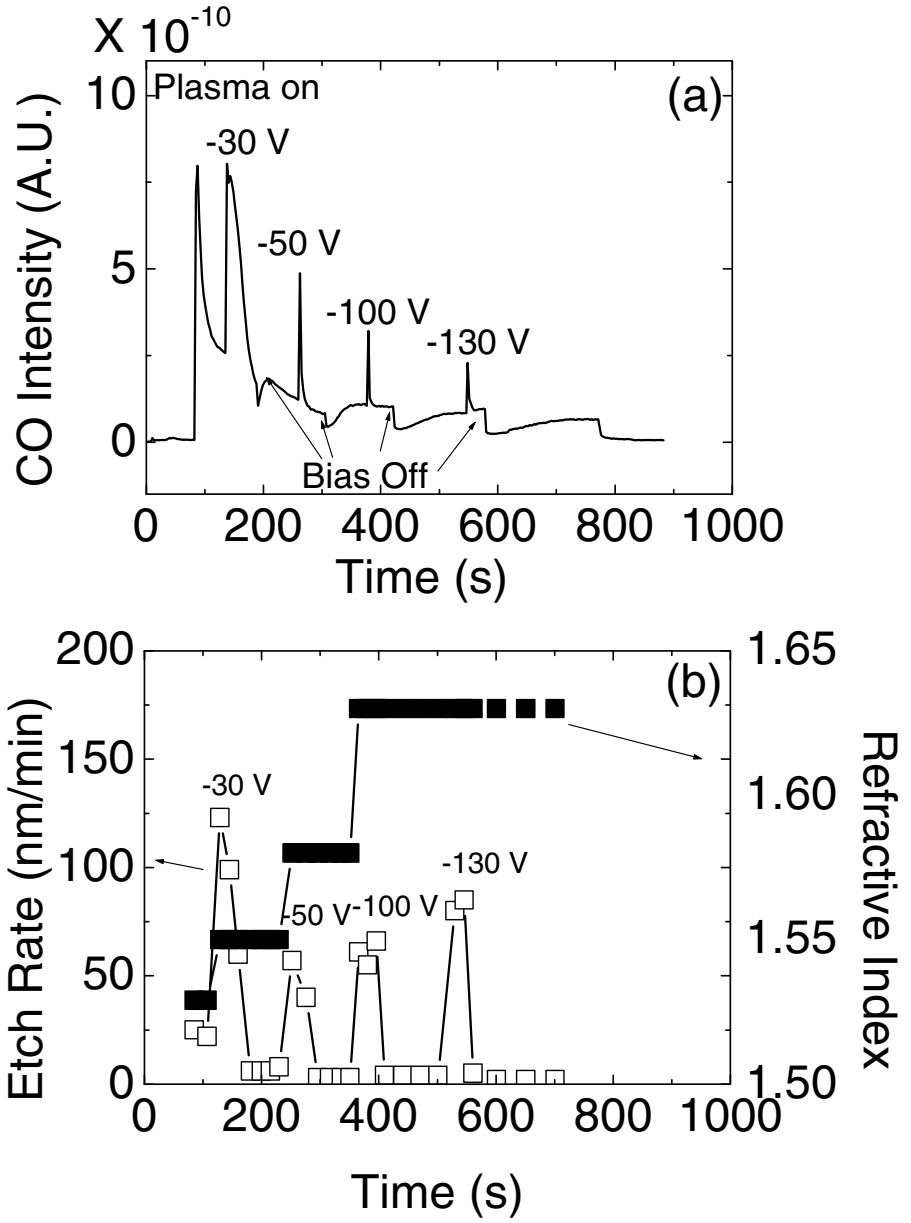

Fig. 3.12: Dependence of (a) CO intensity and (b) etch rates and refractive index of 193 nm photoresist on time in C_4F_8/90%Ar discharge. The other experimental parameters were: 600 W inductive power, 40 sccm gas flow, 10 mTorr.

To study this process in more detail, a 193 nm photoresist sample was processed using different selfbias voltages in the Ar plasma. Mass spectrometry and ellipsometry were used to monitor the sample simultaneously. Figure 3.12 (a) displays the CO^+ signal. Several sharp CO^+ peaks are observed for plasma operating conditions and when a selfbias voltage is applied. The CO^+ intensity decreases strongly each time the bias is switched off, which may indicate depletion of oxygen atom, e.g. carbonyl groups, in the surface region of the plasma etched photoresist film. The idea that the surface region is depleted of species giving rise to CO^+ is supported by the recovery of the CO intensity as a function of time after the bias voltage had been switched off. During this period the photoresist film etches at a slow rate, and the modified near-surface material is removed and unmodified photoresist material is exposed to the plasma. The corresponding refractive index and etch rate of the photoresist film is shown in Fig. 3.12 (b). The refractive index increased as a result of applying larger and larger selfbias voltages, but did not decrease subsequently during the time interval the bias voltage was switched off. This indicates permanent modifications of the photoresist material, e.g. changes in surface topography. The photoresist etch rate increased as a function of bias voltage, except for the initial application of a bias voltage of –30 V. In this situation, the surface of 193 nm photoresist is not heavily damaged before biasing the substrate. No obvious relationship between the photoresist etch rate and the CO^+ signal is indicated by the data of Fig. 3.12.

3.3.8. Characterization of 193 nm Photoresist by TOF-SIMS

The surface of untreated and plasma etched 193 nm photoresist materials were also characterized by TOF-SIMS. Analyzed samples include materials treated in oxygen (no selfbias voltage applied), pure C_4F_8 and C_4F_8/90% Ar plasma.

Both the positive and negative SSIMS spectra from the untreated material are characterized by high molecular weight peaks. In particular, a large molecular peak is detected at m/z 498.92 in the negative spectrum, along with several other peaks at lower masses, as shown by Fig. 3.13 (a). The study of this fingerprint reveals that the largest part of the species detected as negative ions are related to perfluoroalkane-sulfonates, reasonably present as photo-acid generator (PAG) in this photoresist[3.25]. In fact, the parent peak can be attributed to $C_8F_{17}SO_3^-$, whilst the remaining peaks can be evenly related to smaller fragments arising by the parent molecular ion. The inventory list of these species is summarized in Table 3.2. The most intense peak in the positive SSIMS spectrum is observed at 149.132 amu. In addition, larger species up to about mass 600 amu are observed. The exact mass value of the major peak is in agreement with the expected mass of $C_{11}H_{17}^{+\cdot}$ The mass of the larger ions is generally close to the mass integer value. The larger ions must contain little, or no, hydrogen and thus likely correspond to derivatives containing fluorine, oxygen or both. Based on these results, it is argued that the positive species are related to the resist polymer backbone. In particular, $C_{11}H_{17}^+$ likely corresponds to the adamantane ring present as protective group of fluorinated polymers as acrylates.

The comparison of the negative SSIMS spectra obtained by the oxygen plasma exposed samples clearly highlights that this process caused high molecular

weight peaks observed for the virgin material to vanish. This is shown in Fig. 3.13 (b). The peak related with $C_8F_{17}SO_3^-$, almost completely disappears (80x reduction of the measured intensity) as well as the intensity of the fragments still related to PAG that unsurprisingly drops to the background value. Accordingly, the comparison of the positive SSIMS spectra of virgin and oxygen treated samples shows the vanishing of the largest part of the peaks related with the photoresist polymer backbone. The SSIMS results thus highlight that the disruption of surface PAG and polymer backbone is induced to a very large extent upon the O_2 plasma treatment.

Ion	Mass [amu]	Ion	Mass [amu]
SO_3	79.95	CF_2SO_3	129.96
$C_2F_3SO_3$	160.97	$C_3F_6SO_3$	229.97
$C_4F_7SO_3$	260.95	$C_4F_8SO_3$	279.95
$C_5F_9SO_3$	310.93	$C_6F_{11}SO_3$	360.92
$C_7F_{13}SO_3$	410.91	$C_7F_{15}SO_3$	448.90
$C_8F_{15}SO_3$	460.91	$C_8F_{16}SO_3$	479.92
$C_8F_{17}SO_3$	498.92		

Table 3.2: Measured mass and proposed origin of peaks characterizing the untreated 193 nm photoresist PAG (neg. SSIMS).

Very strong modifications of the 193 nm photoresist surface are induced by the pure C_4F_8 plasma treatment. This is shown in the comparison of negative SSIMS

spectra obtained from the virgin (Fig. 3.13 (a)) and C_4F_8 plasma treated photoresist (Fig. 3.13 (c)). After plasma etching, the molecular peaks characterizing the untreated material are absent. Instead, a completely new family of compounds is formed. These species provide a regularly spaced fingerprint related to molecular ions containing an increasing number of C and F atoms. The mass difference between adjoining peaks is equal to 12.000 or 18.998 amu and the largest mass peak shown in Fig. 3.13 (c) matches with $C_{13}F_{17}^-$ (478.973 amu). These observations support the conclusion that rather long chain fluorocarbon compounds are formed upon this plasma process. These conclusions are also supported by the positive SSIMS spectrum, which confirm the formation of a thin layer of fluorocarbon formed on the photoresist surface in this plasma process.

Fluorocarbon compounds are also observed after C_4F_8/Ar etching. However, the exact mass of the corresponding peaks matches with compounds containing also oxygen. The partial inventory list of these species is summarized in Table 3.3. These observations show that the presence of Ar in the discharge plays a crucial role in determining the efficiency of the reaction mechanism leading to the formation of the fluorinated polymer layer as described previously, due to the interaction of fluorocarbon and ionic species with the bulk polymer material. Part of the species listed in Table 3.3 may in fact be attributed to the dissociation of the FC layer and resist material, and to the simultaneous incorporation of fluorocarbon species.

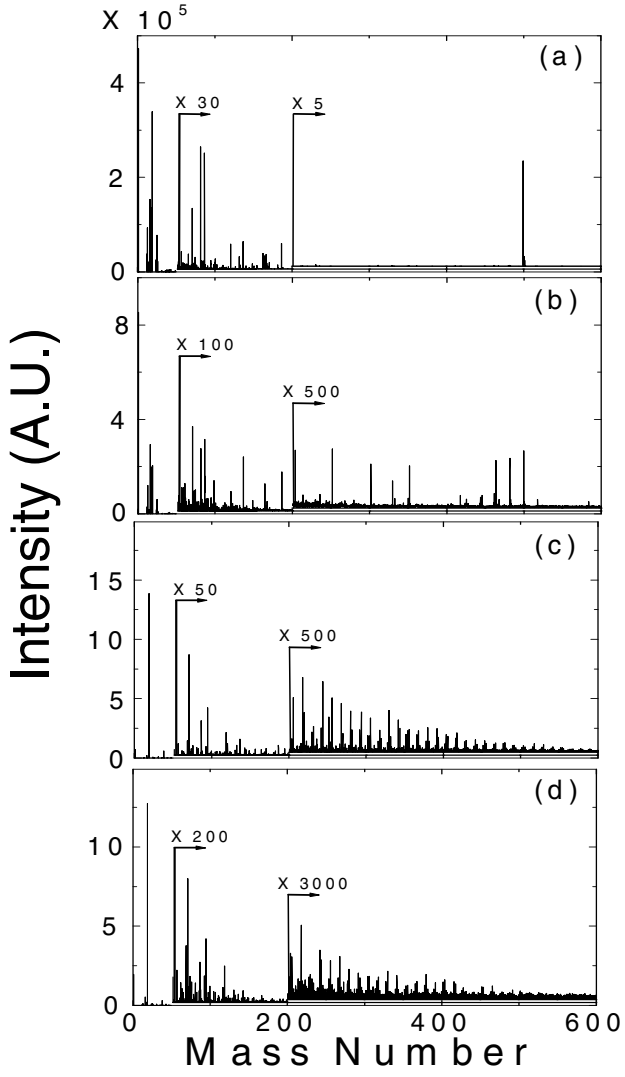

Fig. 3.13: Negative SSIMS spectra of (a) untreated, (b) O_2 plasma exposed and (c) pure C_4F_8 etched, (d) C_4F_8/90%Ar etched 193 nm photoresist. The other experimental parameters were: for C_4F_8 and C_4F_8/90%Ar plasma, 600 W inductive power, 40 sccm gas flow, 10 mTorr and –100 V bias voltage; for O_2 plasma, 400 W inductive power, 40 sccm gas flow, 6 mTorr and without bias.

Mass [amu]	Ion	Mass [amu]	Ion	Mass [amu]	Ion
119	C_2F_5	251	$C_4F_9O_2$	417	$C_7F_{15}O_3$
135	C_2F_5O	301	$C_5F_{11}O_2$	467	$C_8F_{17}O_3$
163	$C_3F_5O_2$	329	$C_6F_{11}O_3$	517	$C_9F_{19}O_3$
185	C_3F_7O	351	$C_6F_{13}O_2$	583	$C_{10}F_{21}O_4$

Table 3.3: proposed composition of species characterizing sample after C4F8/Ar etching (neg. SSIMS, mass value rounded to integer).

3.3.9. Discussion: Mechanism of Surface Roughness for 193 nm Photoresist

The polymer backbone structures of typical 193 nm and 248 nm photoresists are shown in Fig. 3.1. Significant differences in the makeup of 193 nm and 248 nm polymer backbones are observed, including the lack of aromatic groups and the presence of the carbonyl group for the 193 nm material. The lack of aromatic group is expected to decrease the etching resistance, whereas the presence of carbonyl groups can contribute to surface roughness and line edge roughness[3.7, 3.8].

The RMS, R_a and R_{max} roughness examined by AFM are compared in Figure 3.8. As previously stated, for 193 nm photoresist, no significant damage is observed for plasma etching in pure C_4F_8, severe damage is caused by pure Ar plasma etching, whereas the worst damage is caused by Ar-rich C_4F_8 plasmas. The origin of surface roughness may be enhanced for conditions that lead to the simultaneous fluorine penetration into the photoresist film and removal of volatile gas species, like C=O.

The presence of carbonyl group in 193 nm photoresist leads to potential chain scission and production of volatile fragments induced by energetic ion bombardment. For a pure C_4F_8 plasma, thicker and more polymer-like fluorocarbon film are formed on top of the photoresist, and result in a reduced direct attack of the photoresist material by ion bombardment. As a consequence, only a small amount of the carbonyl groups are gasified and the fluorine penetration of the photoresist film is limited. In pure Ar plasma, ion interacts directly with the photoresist film and may gasify carbonyl groups easily. This is seen in the mass spectrometry data, and may be responsible for the severe surface roughness seen in this case. For Ar-rich fluorocarbon plasmas, only a thin fluorocarbon film is formed on the photoresist surface, and the direct ion interaction with the photoresist films is not strongly affected. Ion induced dissociation of carbonyl group is possible, and fluorine penetration into the photoresist film takes place at the same time. The fluorine in the modified photoresist surface may enhance the evolution of C=O, e.g. by COF_2 formation, and lead to enhanced surface roughness for the 193 nm photoresist in this case.

Consistent with our findings, Padmanaban et. al[3.7] compared the surface roughness of different types of 193 nm photoresist in aggressive fluorocarbon plasmas used for oxide etching. They found that electron beam curing of 193 nm photoresist before plasma exposure strongly improved the etch performance of 193 nm photoresist, with regards to both etching rate and introduction of surface roughness. This was also seen in the work of Kudo et. al[3.8]. Both groups contribute the improvement to cleavage of carbonyl groups upon e-beam curing.

3.4. CONCLUSION

Dry etching characteristics of both 193 nm and 248 nm photoresists was investigated in inductively coupled plasmas fed with Ar, C_4F_8, C_4F_8/Ar and O_2. We find that the plasma durability of the 248 nm photoresist that we examined was better than that of 193 nm photoresist material, both in terms of etching rate and surface smoothness. XPS analysis showed that removal of carbonyl groups from the surface region is seen for 193 nm photoresist in both Ar and C_4F_8/Ar discharges and strongly correlated with ion bombardment of the photoresist surface. For the same conditions introduction of enhanced surface roughness is seen by AFM. For pure Ar discharges, an increased signal of volatile CO is observed by MS during plasma etching for 193 nm photoresist material as compared with 248 nm photoresist. The SIMS analysis suggests the fluorine penetration of the photoresist material is strongly promoted when Ar is present in the fluorocarbon plasma. Elimination of reactive groups like C=O from the polymer backbones of photoresists, either during the design of the photoresist, or possibly by a pre-treatment like electron-beam irradiation, should be valuable in reducing the introduction of surface roughness (and likely line edge roughness) during plasma etching. In addition, surface roughness varies strongly with plasma etching conditions and careful control of the plasma-photoresist surface interactions is required to minimize surface and line edge roughness for photoresist materials.

ACKNOWLEDGEMENTS

The authors gratefully acknowledge support of this work by Lam Research Corporation and the Department of Energy under Contract No. DE-FG0200ER54608. We thank Drs. R. E. Ellefson and L. C. Frees and INFICON Inc. for helpful discussions and support with the mass spectrometry equipment.

Chapter 4: Studies of Fluorocarbon Film Deposition and its Correlation with Etched Trench Sidewall Angle by Employing a Gap Structure in C_4F_8/Ar Based Capacitively Coupled Plasmas

To be submitted to J. Vac. Sci. Technol. A, 2006

Li Ling, X. Hua, L. Zheng, G. S. Oehrlein, E. A. Hudson and P. Jiang

Abstract:

A small gap structure has been used to study surface chemistry aspects of fluorocarbon (FC) film deposition and to simulate FC film deposited on feature sidewalls during pattern transfer for fluorocarbon plasmas produced in a mechanically confined dual-frequency capacitively coupled plasma (CCP) reactor. The small gap structure provides a completely shadowed region, without direct ion bombardment, similar to sidewall surfaces of trench patterns. On both trench sidewalls and the shadowed surface portions of the small gap structure, very thin FC layers are formed by adsorption due to reactive neutrals. During etching, film deposition on the sidewall produces a characteristic sidewall slope angle. We show that the feature sidewall angles formed for different process chemistries qualitatively correlate with the deposition rates measured for shadowed surfaces of the gap structure. For C_4F_8/Ar, (C_4F_8/Ar)/O_2 and (C_4F_8/Ar)/N_2 discharges, the deposition rate, composition and bonding of deposited FC films are determined as a function of processing conditions by using ellipsometry and X-ray photoemission spectroscopy (XPS). The deposition rate and surface chemistry of FC films deposited in this region depend strongly on

discharge chemistry. The lack of ion bombardment for the shielded deposition increases the retention of the chemical structure of the FC film precursors in the deposited films. A carbon-depleted FC film is observed when N_2 or O_2 are added to C_4F_8/Ar.

4.1. INTRODUCTION

As ultralarge scale integrated (ULSI) circuits are scaled down, resistance capacitance (RC) delays in the backend-of-the-line (BEOL) increase and dominate the circuit performance. To reduce RC delays, low k and ultra-low k dielectric materials are introduced as a replacement for SiO_2 and need to be integrated into the BEOL processing sequence. Plasma etching of low k or ultra-low k materials can be challenging, as the process used to etch SiO_2 and silica-based low k materials can be quite different[4.1-4.3]. FC film deposition during fluorocarbon plasma-based low k material etching is known to play an important role for pattern transfer of photoresist features into these materials. The deposited FC films affect both the etch selectivity to the mask and the film below the low k material, as well as the low k material etching profiles[4.4-4.10]. A general observation for fluorocarbon discharges has been that high energy ions induce etching reactions whereas low energy ions and neutrals contribute to FC deposition at surfaces[4.11-4.23].

We previously described the use of the gap structure shown in Figure 4.1 to investigate the influence of ion bombardment on the composition of deposited FC films and to simulate FC deposition on feature sidewalls during pattern transfer[4.24]. The lack of ion bombardment underneath the gap structure makes this region similar to a sidewall in a trench pattern. As expected, FC film bonding and composition show strong differences with and without ion bombardment. In the current investigation we have expanded this work, to measure for several prototypical discharges FC film deposition rates, composition and bonding using the small gap structure, along with determining etching rates and etched trench profiles of features formed in

organosilicate glass (OSG) and porous OSG. Our experimental results clearly show that the ratio of the FC deposition rate under the "roof" to the low k material etch rate strongly correlates to the sidewall angle of the etched feature for various plasma etching chemistries. This suggests that this method can be used to examine surface chemical aspects of sidewall deposition processes controlling etching profiles.

4.2. EXPERIMENTAL

4.2.1. Gap Structure

To investigate the influence of ion bombardment on the composition of deposited FC films and to simulate FC deposition on the sidewall during pattern transfer, a gap structure was used[4.24]. Figure 4.1 compares the gap structure with a high aspect ratio trench feature etched using a fluorocarbon plasma. The gap structure was formed by placing two rectangular Si spacers between a Si roof and a Si base wafer. The thickness of the Si spacers was 0.65 mm. The purpose of the rectangular spacer design is twofold: 1) The spacers produce one-dimensional diffusion of neutrals; 2) The spacers provide a large contact area between the roof and base wafers and prevent an excessive temperature rise of the roof wafer, especially for processing conditions using RF bias. The base wafer is designed to be 15 mm longer than the roof wafer, so that a part of the base wafer is exposed to direct ion bombardment, while the other part of the base wafer is underneath the roof wafer and forms a completely shadowed region. A transition region exists between the ion bombarded and the shielded areas. In the exposed part of the wafer both ions and neutrals interact in the formation of FC layers (no RF bias) or the etching of a thin film (with applied

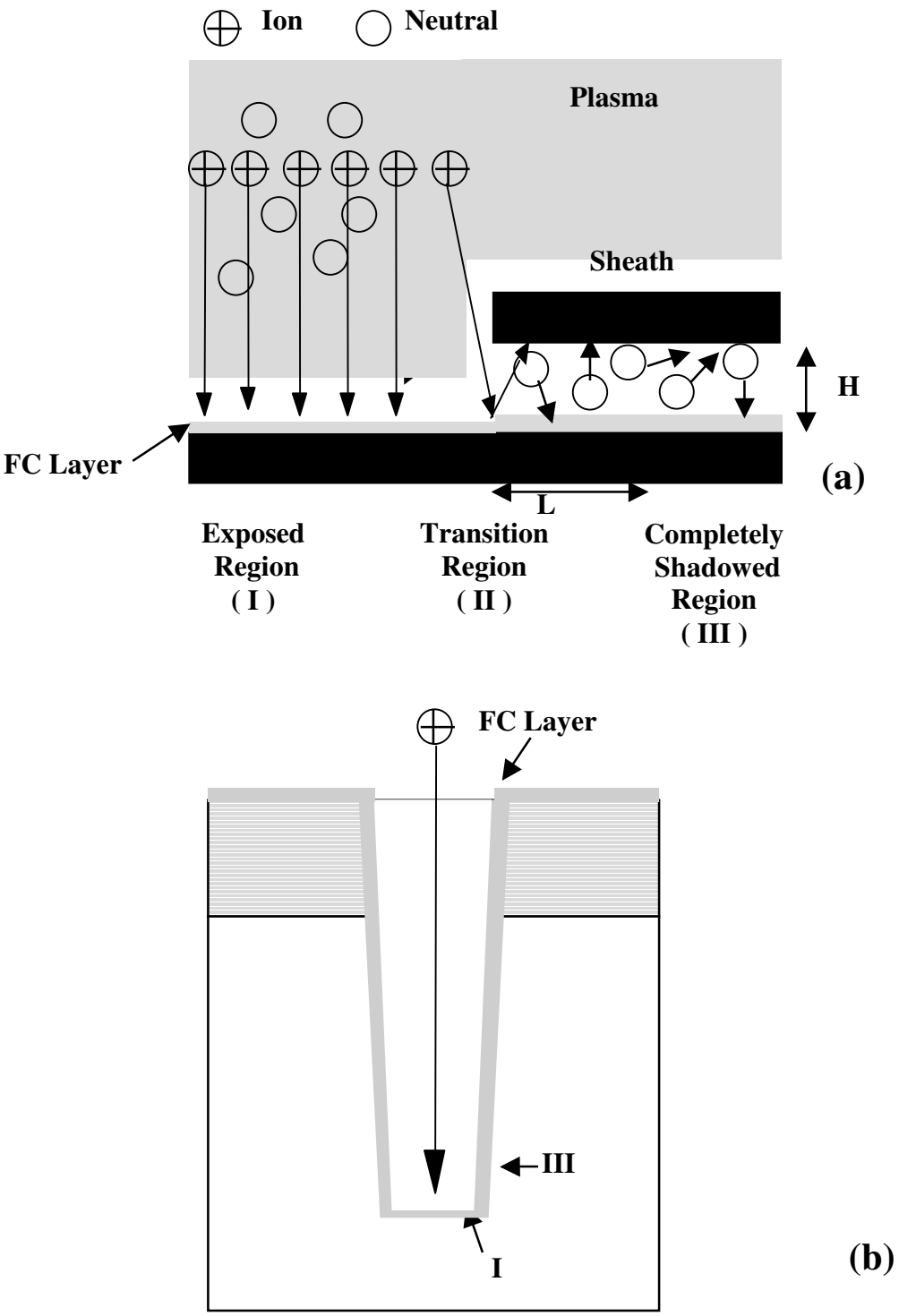

Fig. 4.1: (a) Schematic of small gap structure used in this work and comparison with (b) the high aspect ratio feature.

RF bias). This plasma-surface interaction is characteristic of feature surface portions that are in line-of-sight of the plasma, e.g. the bottom of a trench. In the transition region, ions, either deflected by the sheath formed at the edge of the roof wafer, or incident at large angles relative to the normal, bombard some of the shielded surface area. The ion flux decreases sharply as compared to that incident on the exposed region. This plasma-surface interaction appears similar to that experienced by surface elements located near the top of trench sidewalls. For the fully covered surface portions, ion bombardment is negligible. Film growth in the shadowed region is due to neutrals that diffuse underneath the roof and form a FC layer. The lack of ion bombardment makes this region similar to the sidewall of a high-aspect ratio trench. FC films formed in the completely shadowed region are typically only a few nm thick. This was studied for both silicon wafers from which the native oxide had been removed by etching in a 1% HF solution, and OSG coated silicon.

During plasma etching of actual patterned dielectric films on substrates, there are two dominant processes that determine the feature profile: The dielectric etching rate ER_{trench} at the bottom of the trench structure feature and the FC film deposition rate $DR_{sidewall}$ occurring on the feature sidewall. If these processes dominate relative to other processes, e.g. we ignore changes of the profile due to roughening of the photoresist mask, and so forth, they will determine the feature sidewall angle formed during plasma etching. Figure 4.2 shows a simple schematic of the application of this simple model to trench etching and the profile of an actual etched trench. As shown in Figure 4.2 (a), $DR_{sidewall}$ and ER_{trench} form the two legs of a right triangle. The average etching rate (ER_{trench}) during pattern transfer can be calculated from the actual etched

profile. The actual deposition rate $DR_{sidewall}$ on the feature sidewall is unknown. We approximate the deposition rate on the feature sidewall $DR_{sidewall}$ using the deposition rate DR_{gap} measured underneath the roof of the gap structure. Therefore, from Figure 4.2 (a), the relation between sidewall angle and the ratio between $DR_{sidewall}$ and ER_{trench} can be deduced as

$$tg(90^0-\theta)=(DR_{sidewall}*t)/(ER_{trench}*t)$$

$$\approx DR_{gap}/ER_{trench} \quad (1)$$

Here t is the actual time of the etching process.

Of a variety of possible processes occurring at feature sidewalls, the deposition rate measured underneath the roof of the gap structure will only reflect the FC film deposition aspect due to gas phase species. DR_{gap} does not account for redeposited etch product, which will become relatively more important for etching processes with little or no FC film deposition on the sidewall. For strongly inclined feature sidewalls, ion bombardment of sidewall surface elements can no longer be ignored, and this process can also not be captured by the present methodology. Our data show that the present approach correlates well with the qualitative behavior of the sidewall slope evolution over a range of process conditions, and shows systematic differences at the above extremes. A key aspect of the present approach is that it enables the study of the surface chemical aspects of the deposited FC films that are relevant to sidewall processes.

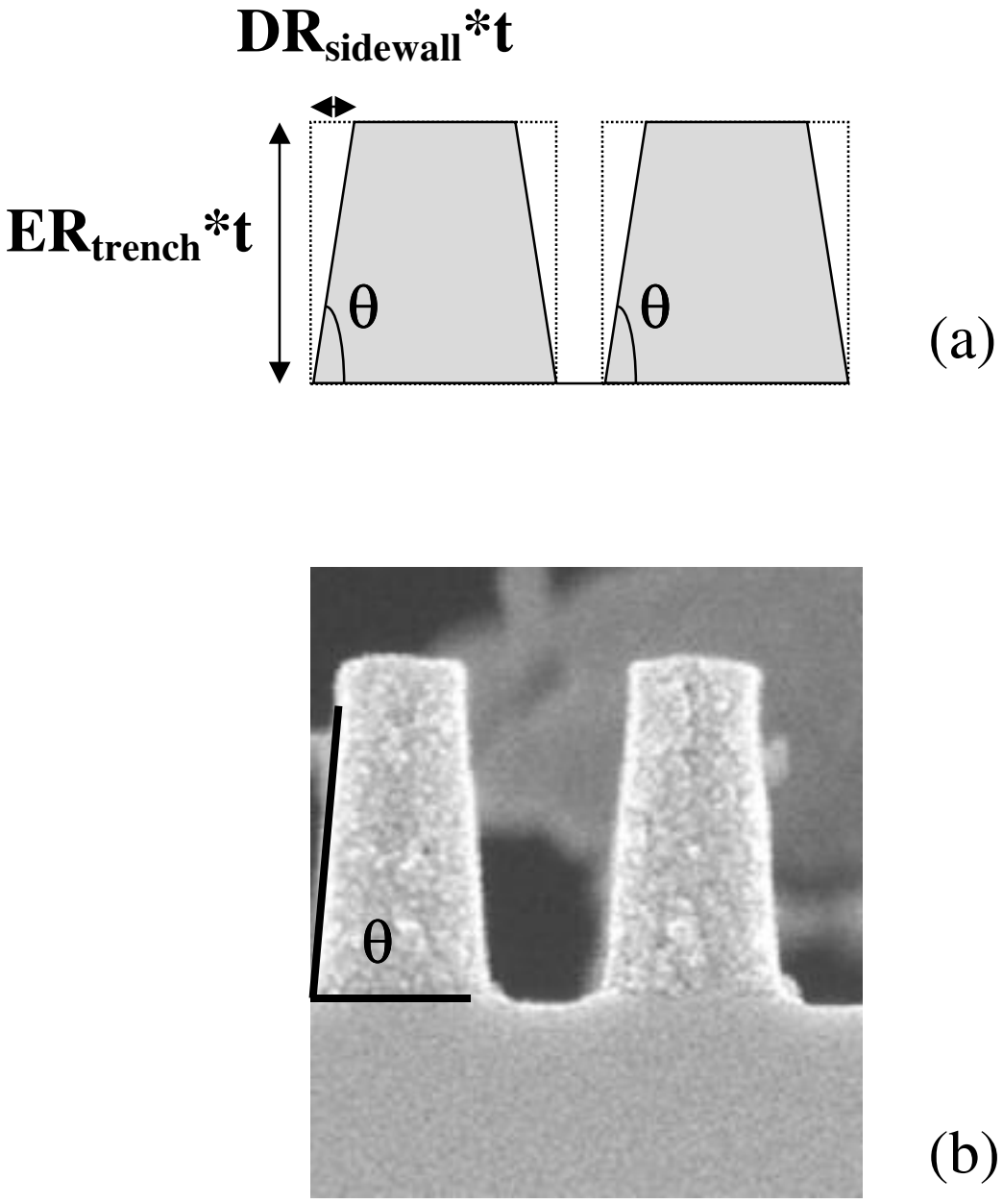

Fig. 4.2: (a) Schematic of dominant processes that are expected to control sidewall profiles and comparison with (b) the profile of an actual etched trench in OSG.

4.2.2. The Capacitively Coupled Plasma Reactor and Experimental Procedures

The reactor used in this study is a dual frequency capacitively coupled plasma (CCP) reactor[4.24, 4.25] and a schematic is shown in Figure 4.3. The top electrode features a showerhead design for gas distribution and is powered using a 40.68 MHz power supply. Typical powers applied are in the range of 100 to 300 W. Matching of the source power is achieved through a Π-matching network configuration, which allows high power transfer efficiency. Ground shields surround the rim and back of the top electrode to prevent discharges outside the space above the bottom electrode. An aluminum confinement ring is installed outside of both electrodes to mechanically confine the plasma, and to provide an additional ground reference. The bottom electrode is powered through a modified L-matching network using a 4 MHz RF power supply. Typical RF bias power levels are in the range of 50 to 150 W. The gap between the two electrodes (125 mm diameter) is 50 mm. The electrodes are located in a stainless steel chamber with an inner diameter of 250 mm. The wafer is mounted on the cooled bottom electrode using a thermal paste to provide good temperature control of the wafer. The bottom electrode is connected to a low temperature circulator, and kept at 10^{o}C. The system is pumped using a magnetically suspended turbomolecular pump backed by a roots blower and a mechanical pump. The base pressure of the chamber is about 1×10^{-6} Torr. The process gases are admitted using mass flowmeters. For all experiments described here the total gas flow into the reactor was set at 40 sccm (standard cubic centimeters per minute), and the pressure was varied from 30 to 80 mTorr. Constant pressure was maintained by using an automatic throttle valve in the pump line.

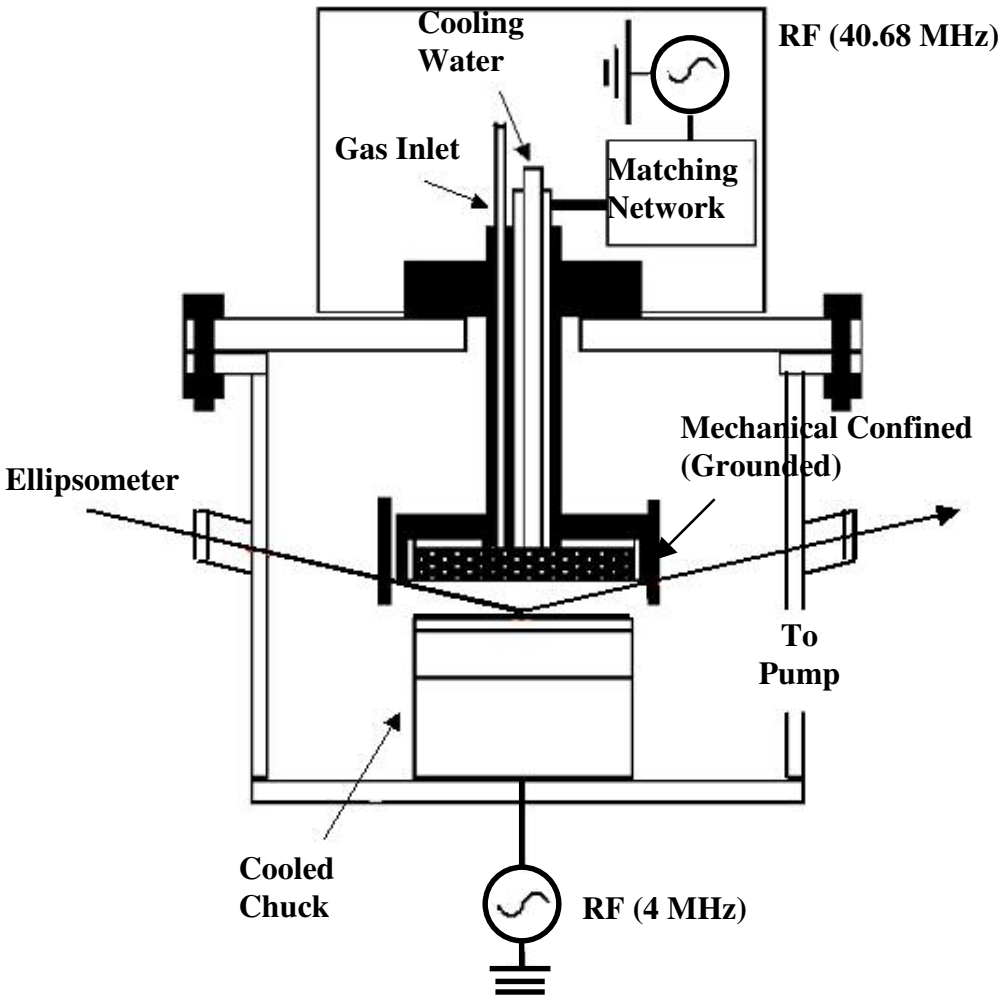

Fig. 4.3: Schematic diagram of the Capacitively Coupled Plasma system.

C_4F_8/Ar, (C_4F_8/Ar)/O_2 and (C_4F_8/Ar)/N_2 plasmas were employed for the present etching and FC film deposition studies. Both OSG and porous OSG films were patterned by transferring line and space features formed on 300 nm thick 248 nm photoresist on top of a 90 nm thick bottom antireflection coating (BARC) using these gas chemistries. A SiC etch stop layer was employed. The applied source power was 200 W and the bias power was kept at 100 W. The OSG and porous OSG films

were 20% over-etched. After etching, photoresist was removed using in-situ O_2 plasma ashing in the same reactor. For in-situ O_2 ashing we employed an O_2 gas flow rate of 40 sccm, a pressure of 30 mTorr, and the source power was 200 W. No RF bias was applied.

The gap structure experiments were performed as follows. FC films were deposited in both exposed and completely shadowed regions for discharges operated without RF bias to the substrate. After the experiments, the base wafer was removed from the plasma chamber and placed on a motor driven stage and the thickness and refractive index of the deposited FC film as a function of position for both exposed and completely shadowed regions were determined by ellipsometry (632.8 nm He/Ne laser). Deposited FC films on specimens for which air exposure was minimized were also analyzed using X-ray photoelectron spectroscopy (XPS) to determine surface composition and chemical bonding. These measurements were performed at a 90^o and 20^o electron take-off angle using a non-monochromatized Mg K-alpha X-ray source (1253.6 eV).

4.2.3. Characterization of Capacitively Coupled Plasma

In our dual frequency CCP system, the plasma is primarily generated by the upper electrode electric field and the substrate is RF biased by the bottom electrode utilizing the smaller RF power. We have characterized this system using a variety of techniques and present here selected results. We report the demonstration of the ability to independently control plasma density and ion energies using the source power and bias power levels, respectively.

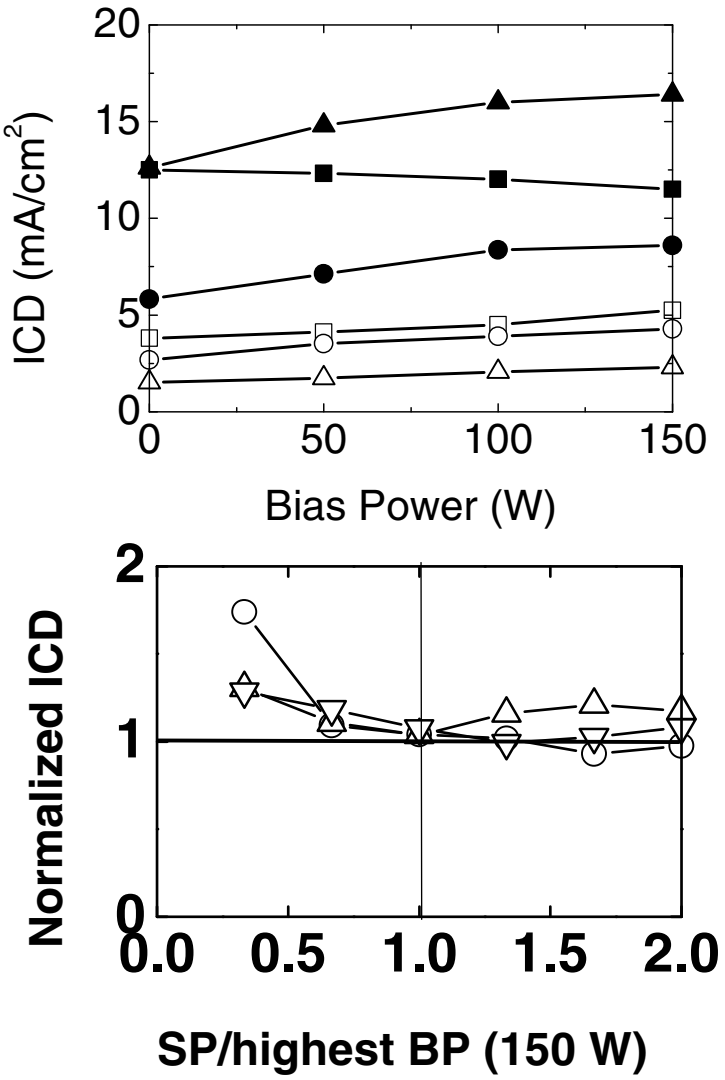

Fig. 4.4: (a) Measured ion current densities for Ar ( ), O_2 (O) and C_4F_8/90%Ar (Δ) plasmas as a function of bias power at both 100 W (void) and 300 W (solid) source power. (b) Normalized ion current densities for Ar ( ), O_2 (O) and C_4F_8/90%Ar (Δ) plasmas as a function of ratio between source power and bias power at 30 mTorr.

To study how the relative levels of source power and bias power affect ion generation, we measured the ion current density (ICD) as a function of bias power for different source power levels (50 W to 300 W). Figure 4.4 (a) compares ICD measured at different bias powers using Ar, O_2 and C_4F_8/Ar plasma. Data obtained using 100 and 300 W source power are shown. The overall conclusion form these data is that if the plasma is sustained at a low source power level, the ICD increases continuously with the applied bias power. On the other hand, for high source power, the ICD increases only slightly at lower bias power and shows saturation at higher bias power. We conclude that for conditions employing low source power, bias power will affect the plasma density and possibly other properties of the plasma, whereas for conditions for which the source power is higher than the bias power this is not the case.

To show how both source power and bias power affect the generation of ions in the plasma, the ICD is normalized as

Normalized ICD=(ICD at 150 W bias power)/(ICD at low bias power) (2)

If the ion generation is not affected by the bias power, then the normalized ICD should be close to 1. Figure 4.4 (b) compares the normalized ICD with the ratio between source power and bias power. For all gas chemistries, when the source power is lower than bias power, i.e. the ratio is lower than 1, the normalized ICD is much higher than 1. It indicates that when source power is lower than or comparable to the bias power, the bias power generates additional ions. If the source power is higher than bias power, i.e. the ratio is higher than 1, the normalized ICD is always close to 1 and is almost not affected by the bias power. Plasma production and ion

acceleration can be decoupled in this case. The fact that ionization is enhanced for application of source power is explained by the higher frequency of the source power supply, which leads to more efficient electron heating than at low RF frequency[4.26-4.29]. In this work the bias power levels are in the range of 50 to 150 W for the etching experiments, and the source power was 200 W and higher.

4.3. RESULTS AND DISCUSSION

4.3.1. Gap Structure Studies

4.3.1.1. FC Film Deposition

It is well known that for plasma deposited FC films, film chemistry and structure depend strongly on whether the growing film is exposed to ion bombardment during deposition or not[4.11-4.23]. Before we compare these aspects for FC films deposited underneath the gap structure and in open areas exposed to ion bombardment, we first report the influence of discharge chemistry and substrate location on the deposition rate. In Figure 4.5 we compare the FC deposition rates in the open area with that in the completely shadowed region for C_4F_8/90%Ar, (C_4F_8/90%Ar)/5%O_2, and (C_4F_8/90%Ar)/10%N_2 plasmas. For these experiments the pressure was kept at 30 mTorr and the applied source power was 200 W. No RF bias power was applied to the substrate. The deposition rates (DR) in the exposed region were measured using an in-situ ellipsometer and the time-averaged deposition rates in the completely shadowed region were measured after 5 minutes deposition using an ex-situ ellipsometer. The FC deposition rates measured for the ion exposed region are about two orders of magnitude higher than those measured for the completely

shadowed region. For both substrate locations, the FC deposition rate varied strongly with gas chemistry and the dependence is similar. The highest deposition rate is observed for pure $C_4F_8$90%Ar plasmas. When even a small amount of O_2 is added to C_4F_8/90%Ar, the FC deposition rate decreases significantly. This may be explained by the ability of oxygen-related species to react with FC film precursors and produce volatile reaction products like CO, CO_2 and COF_2[4.29]. This can lower the overall flux of FC film deposition precursors, and also potentially could lead to removal of already deposited material. This decrease for (C_4F_8/90%Ar)/5%O_2 is much more subtle for surfaces not exposed to ion bombardment than for ion bombarded surfaces. This suggests that the volatilization of already deposited FC film precursors through interaction with oxygen is ion-assisted. When 10%N_2 is added to C_4F_8/90%Ar, the FC deposition rate increases slightly for surfaces exposed to ion bombardment, and decreases for the surface shielded from ion bombardment during growth. N_2 can either assist in the removal of CF_x film precursors by forming volatile CNF_x and NF_3 species or it can be incorporated in the growing carbonaceous film as C_xN_y[4.30]. This will be clearly shown in the XPS spectra to be reported below. We have observed similar trends for deposition at higher pressures, but will not show the data for the sake of conciseness.

In Figure 5 (b) we also compare the FC deposition rates with and without applying bias in the completely shadowed region for C_4F_8/Ar based plasmas. Overall, the FC deposition rates show a slight increase with the application of bias power at C_4F_8/Ar and (C_4F_8/Ar)/O_2 plasmas and remain constant at (C_4F_8/Ar)/N_2 plasmas. We

can conclude that the FC deposition rate in the completely shadowed region is not sensitive to the application of bias in C_4F_8/Ar based plasmas.

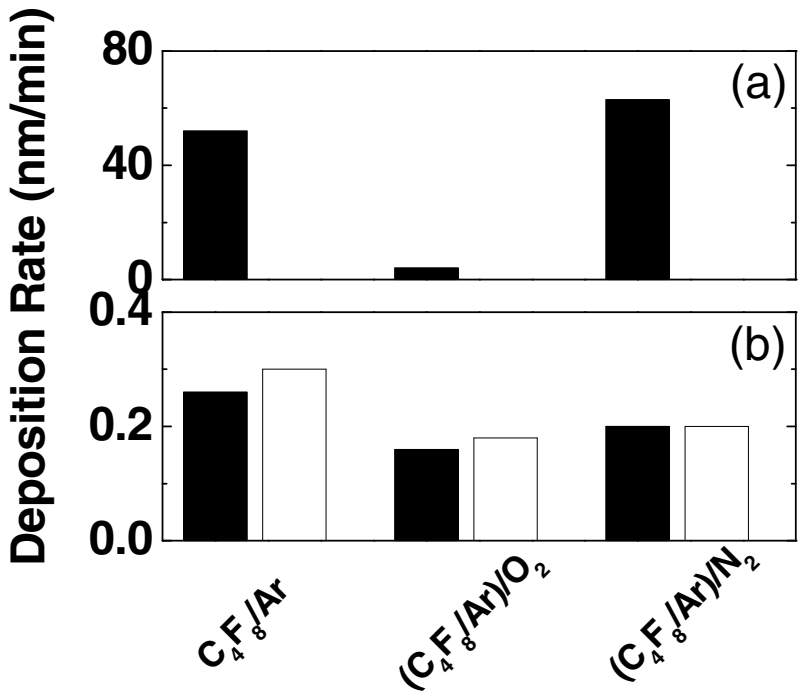

Fig. 4.5: Deposition rates of FC film both in the (a) exposed region and (b) completely shadowed region (solid bar) with and (open bar) without application of RF bias power for C_4F_8/90%Ar, (C_4F_8/90%Ar)/5%O_2, and (C_4F_8/90%Ar)/10%N_2 at 30 mTorr pressure, 200 W capacitive source power and 100 W bias power.

4.3.1.2. Time Dependent FC Film Growth

In general, when surfaces are exposed to ion bombardment during FC film growth the FC film deposition rate remains nearly constant as a function of time. For film deposition without ion bombardment, the deposition rate varies strongly with time. Using the gap structure, a systematic study of FC film deposition without ion

bombardment was undertaken by performing the deposition for different run times, and then measuring the resulting FC film thickness. Figure 4.6 (a) shows the variation of FC film thickness under the roof with deposition time for C_4F_8/Ar, (C_4F_8/Ar)/N_2, and (C_4F_8/Ar)/O_2 plasmas. The applied source power level was 200 W and the pressure was 30 mTorr. In Figure 4.6 (b) the normalized deposition rates are shown for the same experiments. Although continuous growth of FC films is observed for all gas chemistries, the normalized deposition rate shows a strong initial decrease and subsequent saturation. This is consistent with the idea that continuous low energy ion bombardment during film growth is important to maintain high deposition rates[4.11-4.15]. After 5 minutes of plasma exposure, the deposition rates measured for C_4F_8/Ar and (C_4F_8/Ar)/N_2 are lower than 10% of the deposition rates measured during the first 30 seconds, while the deposition rate for (C_4F_8/Ar)/O_2 vanishes. This difference may be explained by the ability of O_2 related species to react with FC film precursors. These observations suggest that during pattern transfer, FC deposition on trench sidewalls may be most important when fresh surface elements are initially exposed, and subsequently saturate for C_4F_8/Ar, (C_4F_8/Ar)/N_2 and (C_4F_8/Ar)/O_2 plasmas.

Since the etching study was performed using low k material, we performed the same study using OSG film coated substrates. The measured FC film thickness is slightly lower for OSG than measured on Si substrates (difference is less than 0.5 nm). However, a similar time dependent deposition rate is seen for OSG: The FC deposition rate decreases strongly initially and then saturates. This is also seen in the results of the XPS analysis of deposited films which will be discussed later. This similarity suggests that there is no significant difference between the data obtained for

a Si substrate and an OSG substrate as long as there is no ion bombardment of the substrate during FC film growth. To simplify the data analysis, the deposition rates measured on the Si substrates were used for the comparison with the measured sidewall angles.

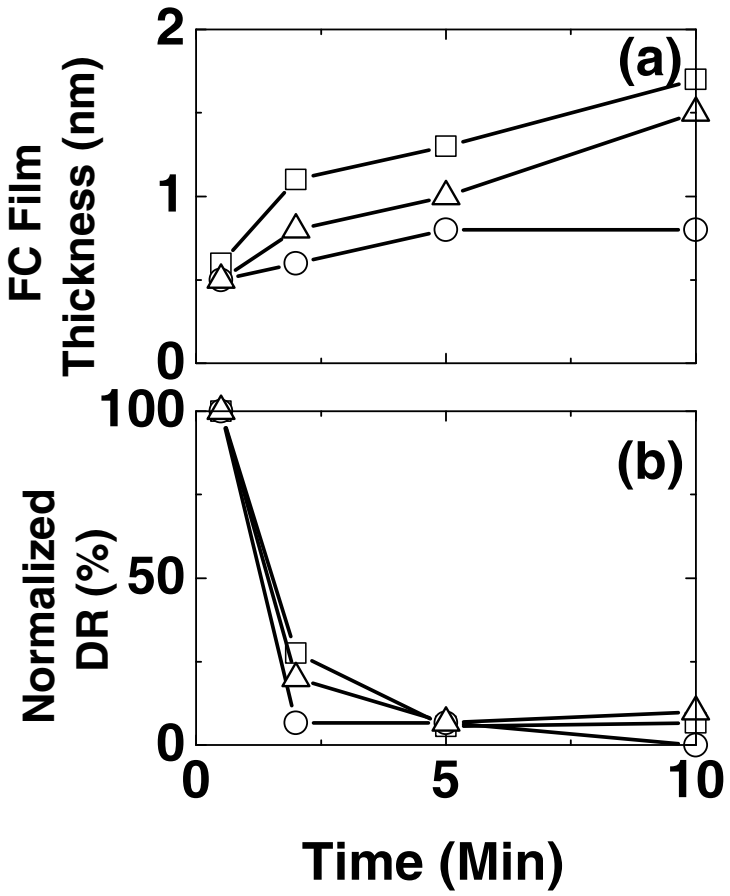

.

Fig. 4.6: Time dependent (a) FC film thickness and (b) Normalized FC deposition rates completely shadowed region for C_4F_8/90%Ar ( ), (C_4F_8/90%Ar)/5%O_2 (O), and (C_4F_8/90%Ar)/10%N_2 (Δ) measured at 30 mTorr pressure, 200 W capacitive power.

4.3.1.3. Effect of N_2 Addition on FC Film Growth

Previous work in this group has shown that N_2 can play two roles when added to a fluorocarbon gas: it can either assist in the removal of FC film precursors by forming volatile CNF_x or NF_3 species or it can be incorporated into the growing carbonaceous film as C_xN_y[4.30]. The results of the prior work suggest that N_2 addition can be used to carefully adjust both steady state FC film thickness on a horizontal surface and the FC film thickness deposited on feature sidewalls during low k material etching [4.30, 4.31]. The thickness of both FC films contributes to the resulting etching profile. To utilize this concept we measured both the FC deposition rate underneath the roof and the OSG etch rates as a function of N_2 addition to C_4F_8/90%Ar. Figure 4.7 compares the ratio of FC film deposition rate underneath the roof (DR_{gap}) to the blanket OSG etch rate in the exposed region ($ER_{blanket}$) as a function of the amount of N_2 added. Both roles of N_2 can be immediately seen in the figure. When a small amount of N_2 is added to C_4F_8/90%Ar, a lower ratio of $DR_{gap}/ER_{blanket}$ is observed. This indicates that for this condition, N_2 addition causes a reduction of FC film thickness. When a large amount of N_2 is introduced, a much thicker FC film is formed than C_4F_8/90%Ar without N_2.. This can be contributed to incorporation of nitrogen into the film. Thus, an increased FC film deposition rate and/or decreased OSG etch rate lead to an increase of the *DR/ER* ratio, as is observed in Figure 4.7. A more vertical etching profile may be expected at 10% N_2 addition, which has the lowest $DR_{gap}/ER_{blanket}$ ratio measured.

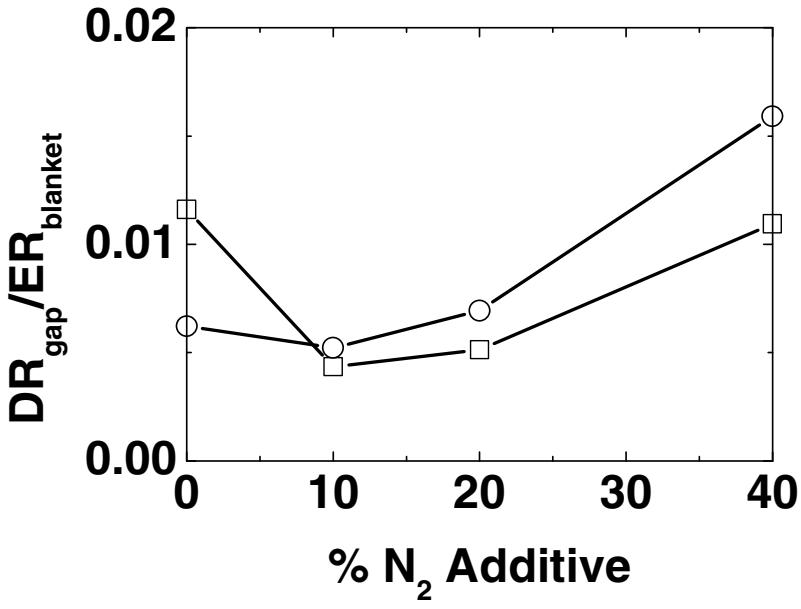

Fig. 4.7: Correlation $DR_{gap}/ER_{blanket}$ ratio with N_2 addition in $(C_4F_8/90\%Ar)/N_2$ plasma at both 30 ( ) and 80 mTorr (O). The other experimental parameters were: 200 W capacitive power and 100 W bias power for etching and without bias for deposition.

4.3.1.4. Surface Analysis of Deposited FC Film in the Completely Shadowed Region by XPS

It is well known that N_2 and O_2 addition for fluorocarbon discharges can be used for the control of etching profiles. However, some side effects may be caused by N_2 and O_2 addition, which will significantly affect its application. To understand the role of nitrogen and oxygen in the etching profile control during the pattern transfer, FC films were deposited underneath the gap structure using $(C_4F_8/90\%Ar)/10\%N_2$

and (C_4F_8/90%Ar)/5%O_2 plasmas and then examined by XPS. Figures 4.8-4.12 show the XPS spectra of the FC layers deposited on both Si and OSG substrates. The XPS spectra of the FC film deposited using the C_4F_8/90%Ar plasma are included for comparison. The other experimental conditions were 30 mTorr operating pressure, 200 W source power and no bias applied. The time used for these depositions was 5 minutes. For all conditions, the C (1s), F (1s), N (1s), O (1s), and Si (2p) spectra are shown at electron emission angles of 70º relative to the horizontal surface.

4.3.1.4.1. FC Film Deposition on Si Substrates

The C (1s) spectrum obtained in C_4F_8/90%Ar plasma, which is shown in Figure 8, is similar to the spectra of the conventional FC films deposited directly by a plasma process[26]. Four peaks (in order of increasing binding energy), can be assigned to C-CF_x (x=1, 2, 3), C-F, C-F_2, and C-F_3 bonding. For this gas chemistry, C-F_2 bonding dominates the C (1s) spectra. C-CF_x and C-F bonding are very weak, but can still be detected.

As N_2 is added, the most significant change shown in the spectra is nitrogen incorporation into the FC film. This can be clearly seen in both C (1s) and N (1s) spectra. In the N (1s) spectrum, it results in the appearance of a strong C_x-N_y peak. In the C (1s) spectrum, nitrogen incorporation leads to the broadening of the C-F_2 and C-F_3 bonding. At the same time, C-CF_x and C-F bonding can no longer be distinguished. The reaction of CF_x radicals with N_2 can generate volatile CNF_x or NF_3 species, leading to a decrease of the radical density which may result in a thinner FC film deposited under the roof. As a result, a stronger Si-O_2 peak can be observed in

both Si (2p) and O (1s) spectra. The stronger C-F_2 and C-F_3 peaks and much weaker C-CF_x and C-F peaks indicates that without ion bombardment, CF_2 and CF_3 radicals have a higher sticking coefficient and are the main precursors for the film formation in both C_4F_8/90%Ar and (C_4F_8/90%Ar)/N_2 plasmas[24]. This is also observed in the (C_4F_8/90%Ar)/O_2 plasma.

A reduction of FC film thickness is immediately seen when a small amount of O_2 is added to C_4F_8/90%Ar. This can be explained by the greater ability of oxygen related species to react with deposited FC films and generate volatile reaction products. The XPS finding is consistent with the data of the ellipsometric measurements made on these samples. Therefore, the bonding intensities of all peaks are low as compared for films deposited using other gas chemistries. The C (1s) spectrum obtained with films deposited using (C_4F_8/Ar)/O_2 gas chemistry shows some similarity to XPS spectra obtained with (C_4F_8/90%Ar)/N_2, in particular the broadening of C-F_2 and C-F_3 bonding and the disappearance of C-CF_x and C-F bonding. Similar to N_2 addition, the broadening of the C-F_2 and C-F_3 peaks may be the result of oxygen incorporation into the film. Oxygen also oxidizes the Si substrate, as can be seen by strong SiO_2-bonding evident in both the Si (2p) and O (1s) spectra. The FC film deposited with (C_4F_8/Ar)/O_2 is much thinner than the one obtained with (C_4F_8/Ar). The effect of substrate oxidization seen for a Si substrate suggests that for an ultra-low k (ULK) material plasma etching process, the ULK material may be damaged by the addition of oxygen. A much lower F 1s intensity is shown in Figure 12 for (C_4F_8/Ar)/O_2 deposited FC films as compared to spectra obtained with films deposited using C_4F_8/Ar or (C_4F_8/Ar)/N_2. This is the result of a

much thinner FC films and fluorine removal from the film due to interaction with oxygen.

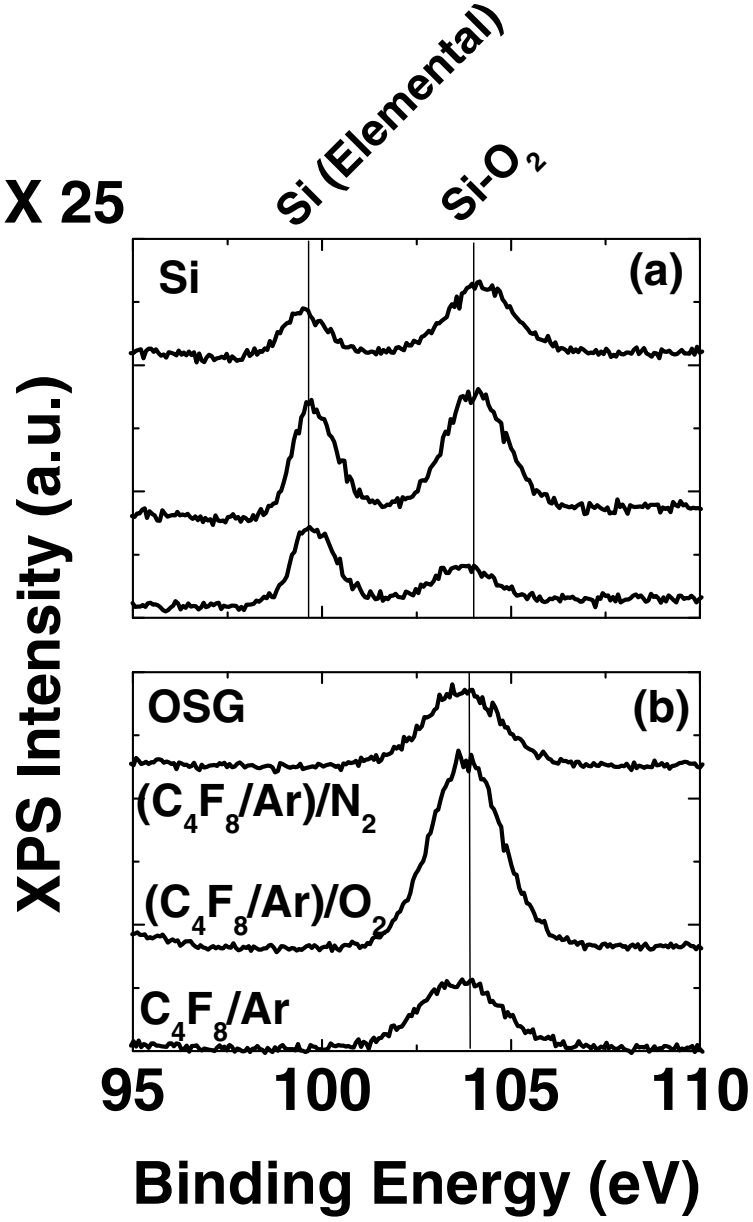

Fig. 4.8: Si (2p) photoemission spectra of FC layer in the completely shadowed region on both (a) Si and (b) OSG substrates in C_4F_8/90%Ar, (C_4F_8/90%Ar)/10%N_2 and (C_4F_8/90%Ar)/5%O_2 plasmas at 30 mTorr pressure and 200 W capacitive power.

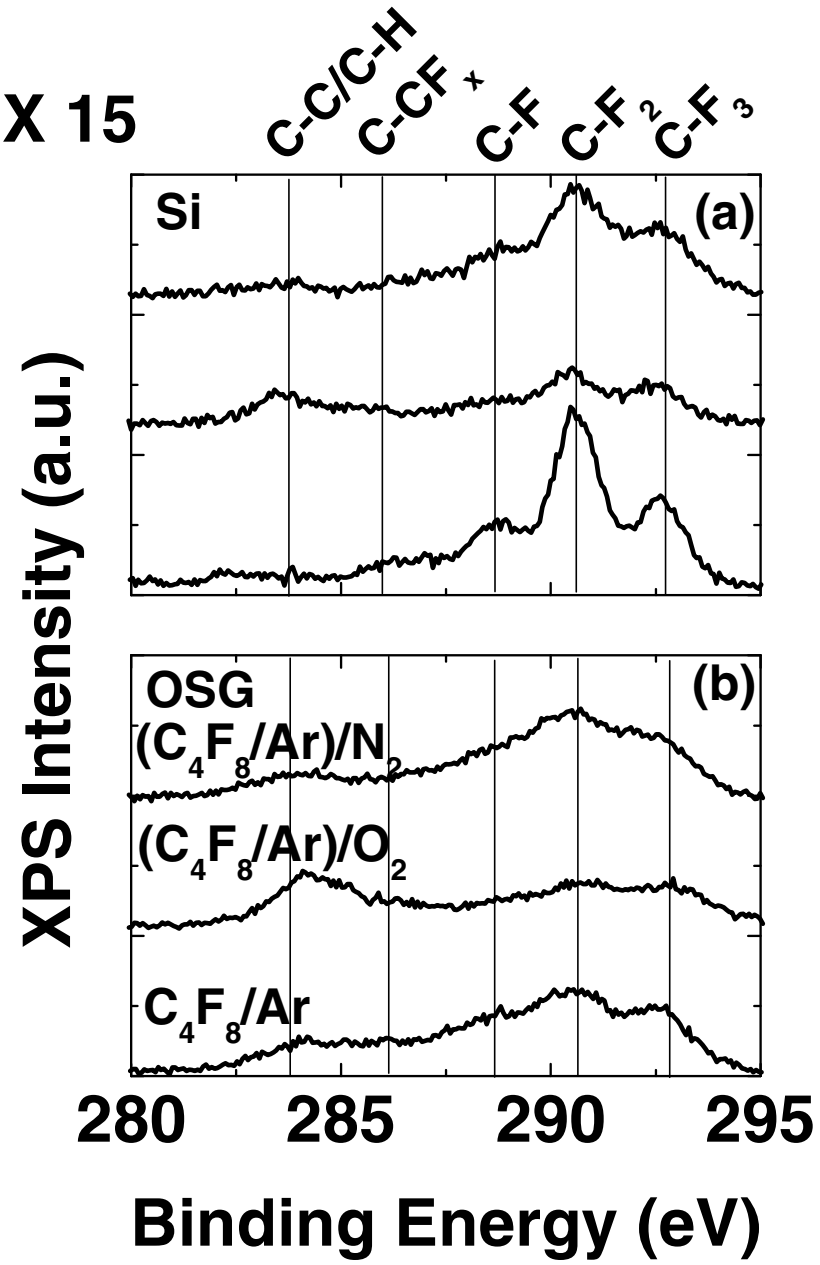

Fig. 4.9: C (1s) photoemission spectra of FC layer in the completely shadowed region on both (a) Si and (b) OSG substrates in C_4F_8/90%Ar, (C_4F_8/90%Ar)/10%N_2 and (C_4F_8/90%Ar)/5%O_2 plasmas measured at same conditions in Fig. 4.8.

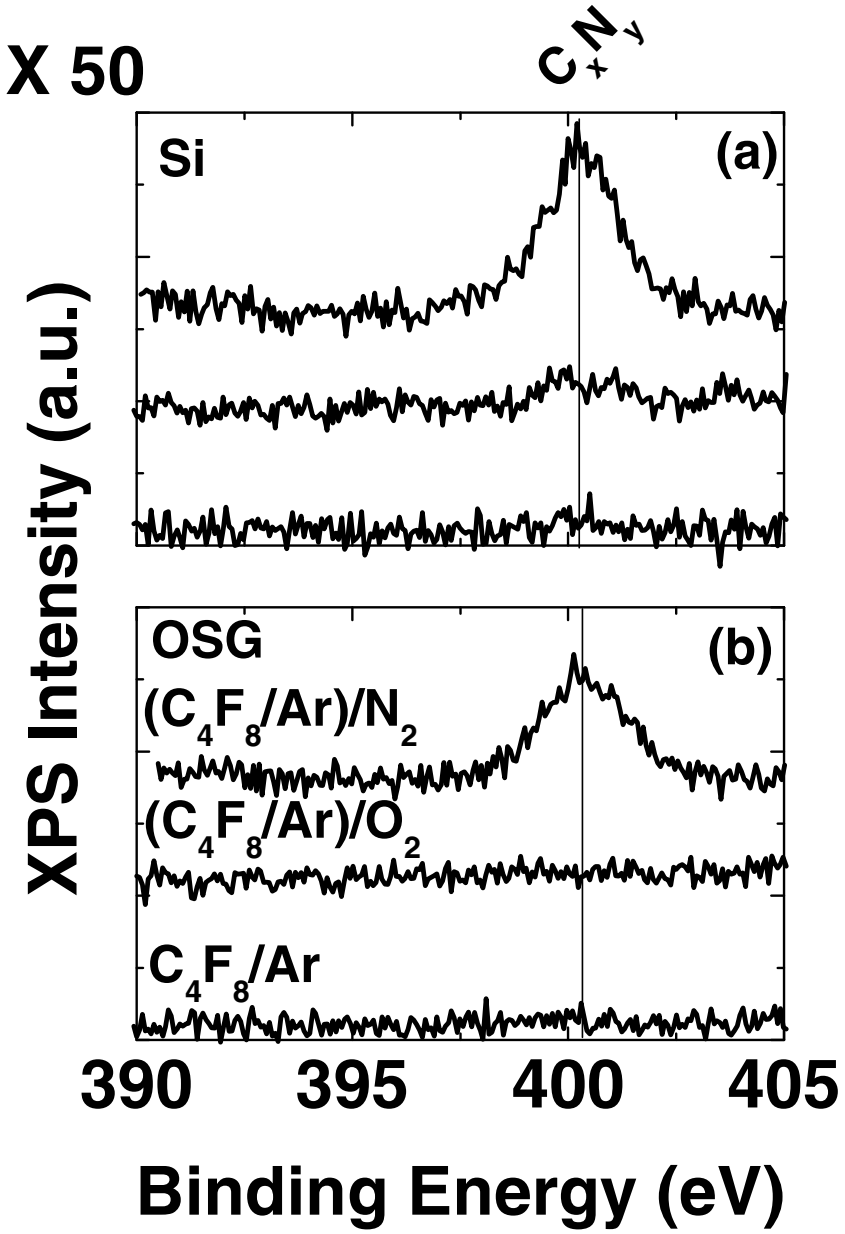

Fig. 4.10: N (1s) photoemission spectra of FC layer in the completely shadowed region on both (a) Si and (b) OSG substrates in C_4F_8/90%Ar, (C_4F_8/90%Ar)/10%N_2 and (C_4F_8/90%Ar)/5%O_2 plasmas measured at same conditions in Fig. 4.8.

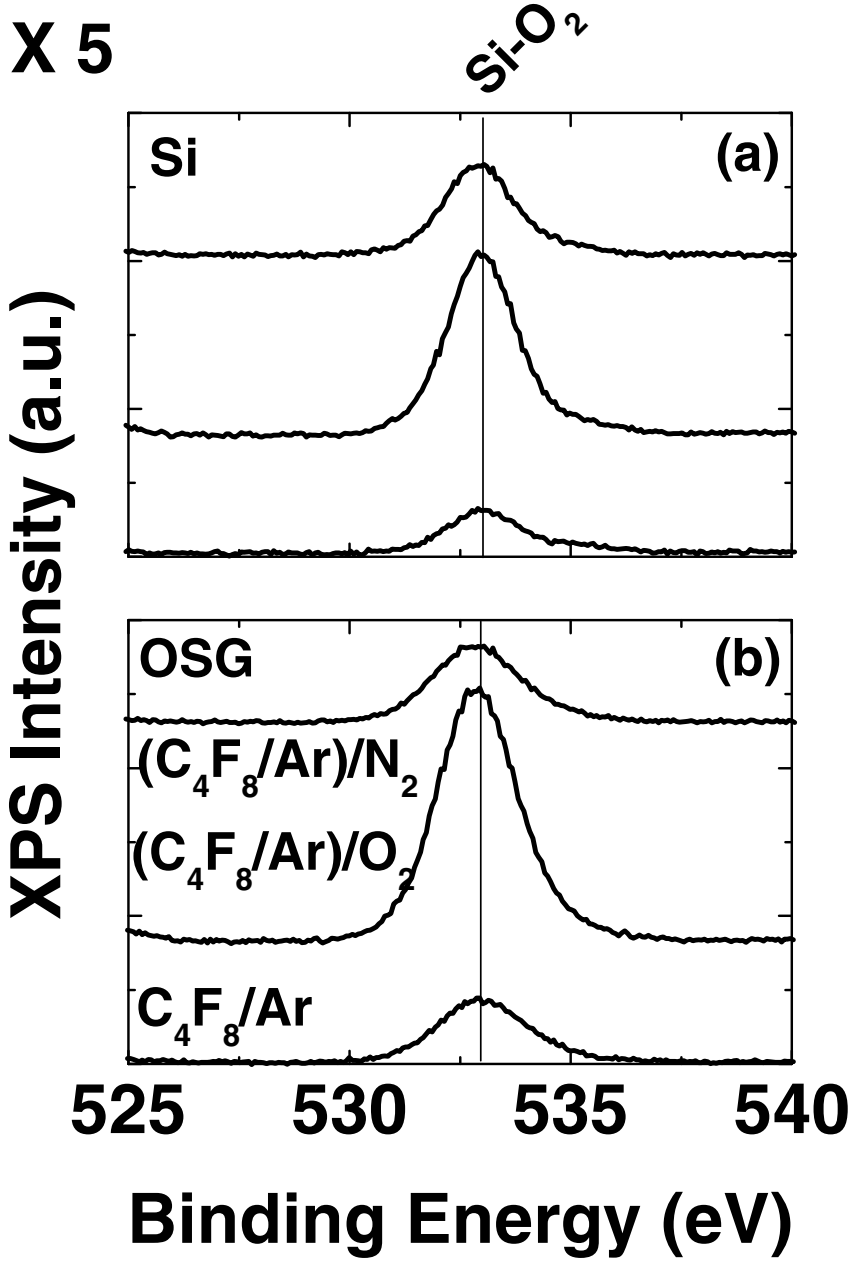

Fig. 4.11: O (1s) photoemission spectra of FC layer in the completely shadowed region on both (a) Si and (b) OSG substrates in C_4F_8/90%Ar, (C_4F_8/90%Ar)/10%N_2 and (C_4F_8/90%Ar)/5%O_2 plasmas measured at same conditions in Fig. 4.8.

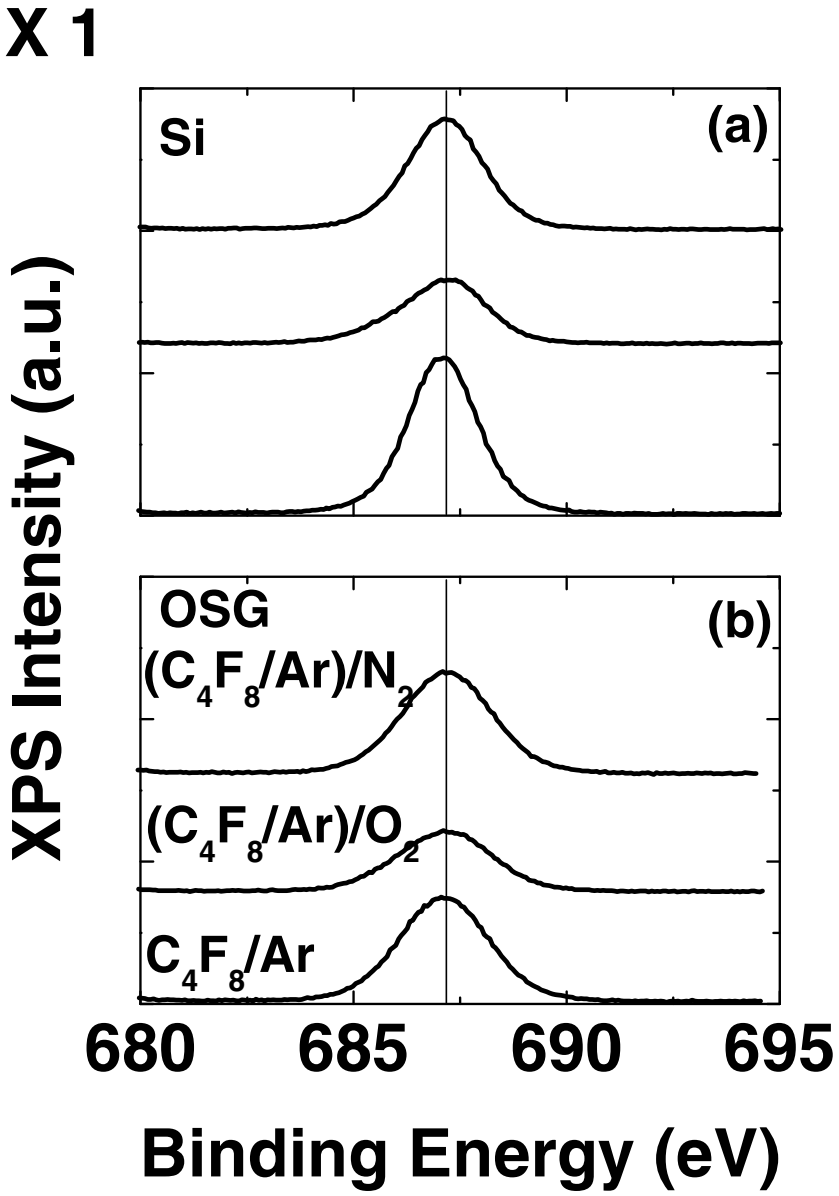

Fig. 4.12: F (1s) photoemission spectra of FC layer in the completely shadowed region on both (a) Si and (b) OSG substrates in C_4F_8/90%Ar, (C_4F_8/90%Ar)/10%N_2 and (C_4F_8/90%Ar)/5%O_2 plasmas measured at same conditions in Fig. 4.8.

4.3.1.4.2. FC Film Deposition on OSG Substrate

Since the etching studies were performed using OSG rather than Si substrates, we also studied FC deposition underneath the roof on OSG substrates. The corresponding XPS spectra are shown in Figures 4.8-4.12. Overall, the trends seen for different gas compositions are consistent with the data obtained with Si substrates. Upon N_2 or O_2 addition to C_4F_8/Ar, the shape of the C (1s), N (1s), O (1s), and F (1s) peaks obtained with OSG show similar changes as seen for Si. Important differences indicated by the XPS spectra obtained for the two types of substrates are: First, the FC film formed on the OSG substrate is thinner than the one deposited on Si. This can be seen in the C (1s) and F (1s) spectra, where the peak intensities are much weaker for the OSG substrate. The second difference is seen in the Si (2p) and F (1s) spectra, where no evidence of Si-F bonding can be seen in the Si (2p) spectrum of OSG. This can at least in part be attributed to the difficulty to distinguish Si-F bonding from Si-O_2 bonding in the XPS data. At the same time, a much lower F (1s) peak intensity is observed for the OSG substrate as compared to Si. This suggests that the OSG substrate is less fluorinated than the Si substrate, and may be explained by a reduced reactivity of the OSG film relative to Si.

4.3.1.4.3 Comparison of F/C, N/C and O/C Ratios on Si and OSG Substrate

Table 4.1 provides a summary of the F/C, N/C and O/C ratios calculated from the XPS spectra for all the conditions described above. The F/C ratio is defined as[31]:

$$F/C = \frac{\sum_{i=1}^{3} iI(C-F_i)}{I(C-Si) + I(C-C) + \sum_{i=1}^{3} iI(C-F_i)} \qquad (3)$$

where I(…) is the area of the fitted Gaussian function for the chemically shifted contribution indicated between the parentheses. The F/C ratio presented here is the ratio of the fluorine in the FC film to the density of C (1s). The use of the F (1s) peak to estimate the fluorine content of the overlayer is difficult, since some of the fluorine has reacted and is associated with the substrate. The quoted N/C and O/C ratios are obtained from the ratios of the densities of N (1s) or O (1s) to the total density of C (1s), respectively.

	Gas Chemistry	F/C	N/C	O/C
Si	C_4F_8/90%Ar	2.862	N/A	N/A
	(C_4F_8/90%Ar)/10%N_2	2.254	0.245	N/A
	(C_4F_8/90%Ar)/5%O_2	1.909	N/A	2.421
OSG	C_4F_8/90%Ar	1.582	N/A	N/A
	(C_4F_8/90%Ar)/10%N_2	1.578	0.118	N/A
	(C_4F_8/90%Ar)/5%O_2	1.033	N/A	2.008

Table 4.1: Comparison of F/C, N/C and O/C ratio in C_4F_8/90%Ar, (C_4F_8/90%Ar)/10%N_2 and (C_4F_8/90%Ar)/5%O_2 discharges on both Si and OSG substrate.

The F/C ratio measured on OSG is universally lower than the corresponding F/C ratio measured for the Si substrate which can be attributed to the existence of SiO-bonding in the OSG substrate. On both materials, the F/C ratio of the FC film decreases as we add N_2 or O_2 to C_4F_8/90%Ar. The F/C ratio is lowest for the (C_4F_8/Ar)/ O_2 case, and may be explained by a high removal rate of carbon. The N/C

ratio reflects the incorporation of nitrogen in the deposited FC film. A much higher level of nitrogen incorporation can be observed for the Si substrate than for the OSG film. This may be attributed to the reaction of nitrogen and oxygen to form volatile NO molecules, which removes most of the nitrogen atoms that have been incorporated. As discussed above, O_2 addition leads to thin FC film. Therefore, the O/C ratio not only reflects the incorporation of oxygen into the FC film, but also is due to the oxidization of the Si substrate. This makes the interpretation of the O/C ratio data difficult.

4.3.1.4.4. FC Film Treatment in the Completely Shadowed Region

The nitrogen and oxygen incorporated in the FC film may play an important role in controlling sidewall damage of fragile dielectric materials, especially for materials with high porosity[4.7-4.9]. To further understand how oxygen and nitrogen affect the FC film underneath the gap structure, we processed FC films in the completely shadowed region using N_2, O_2, N_2/50%Ar and O_2/50%Ar plasmas. The FC films used for this study were deposited in a pure C_4F_8 plasma at 30 mTorr with 200 W source power and no bias power applied. These films were then treated for 5 minutes at 30 mTorr using the above discharges while located underneath the gap structurewhich prevented ion bombardment. The height of the roof in the gap structure was set at 0.65 mm. Generally, after plasma exposure, the XPS spectra showed a decrease of the C-CF_x peak relative to the C-F_x peaks, consistent with a carbon depletion of the treated FC films[32-34]. The XPS measurements also revealed more significant carbon depletion for the oxygen related gas chemistries than for the

nitrogen related gas chemistries. This is due to the different carbon removal ability of oxygen and nitrogen and is consistent with previous FC film deposition studies using oxygen and nitrogen containing plasmas.

4.3.2. Etching Profile Analysis by Scanning Electron Micrographs (SEM)

Figure 4.13 (a) shows cross-sectional scanning electron micrographs (SEM) of OSG trenches etched using C_4F_8/90%Ar at 30 mTorr. Strong FC film deposition on the sidewalls, especially at the interface between the photoresist and OSG film, is observed. Therefore, a rough and sloped sidewall was induced. Due to the overetch, the SiC etch stop layer is attacked. After etching, an O_2 plasma was used to remove the residual photoresist mask in the same chamber. The flow rate of O_2 was 40 sccm, pressure was 30 mTorr, source power was 200 W and no bias was applied. Figure 4.13 (b) shows the cross-sectional secondary electron micrographs of OSG trenches after in-situ O_2 ashing. The average FC deposition rate measured during 5 minutes in the completely shadowed region is also given. Compared with the SEM micrograph prior to O_2 ashing, complete removal of the FC residue on the sidewall, and a better OSG trench etching profile can be seen. However, severe damage of the low k film is introduced by this in-situ ashing process: a horizontal shrinkage of all features, the collapse of some features and strong undercut at the interface of the bulk material and the etch stop layer. This is due to the FC film deposited on the sidewalls during etching process, which apparently reacts with O_2 during the ashing process and causes damage of the low k material[4.35-4.39]. Some ashing reaction products are left at the bottom of the trench. This indicates that during both etching and ashing processes,

the deposited FC film plays an important role in determining the ultimate etching profile.

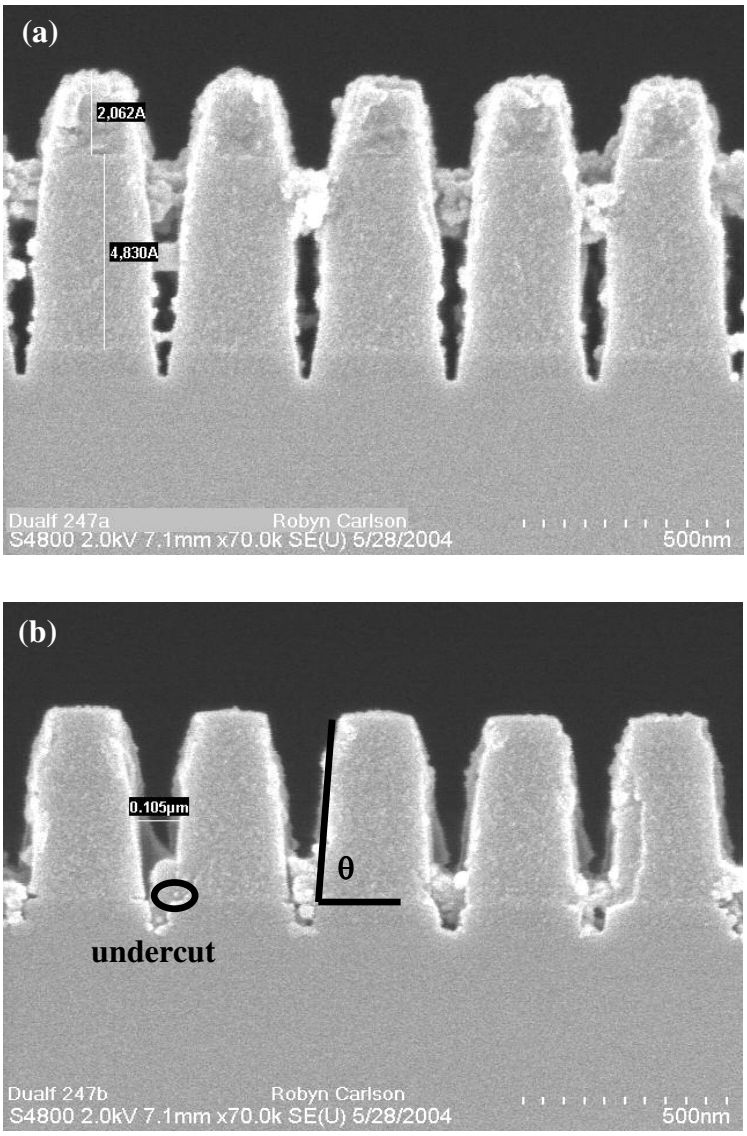

Fig. 4.13: Cross-sectional SEM photographs of patterned photoresist partially etched in C_4F_8/90%Ar plasmas (a) before and (b) after O_2 plasma ashing. The other experimental parameters were: 200 W capacitive power, 30 mTorr and 100 W bias power for etching and without bias for O_2 ashing. The average deposition rate underneath the roof in 5 minutes is 0.3 nm/min.

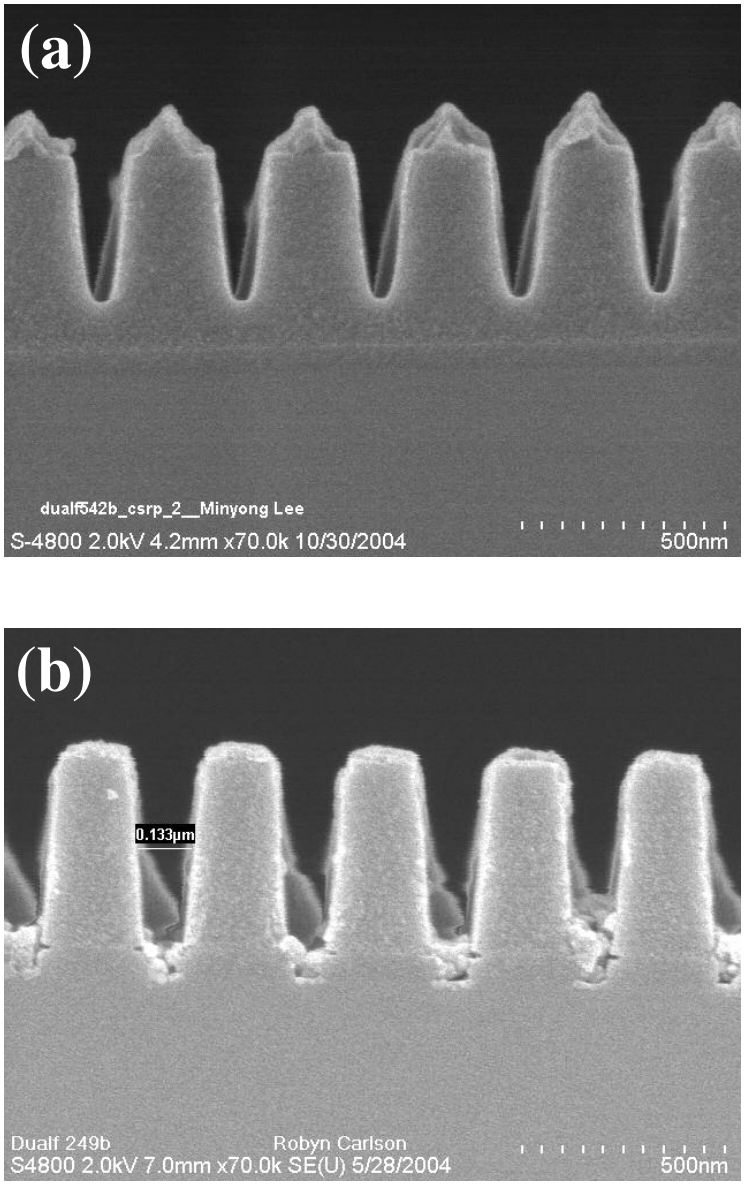

Fig. 4.14: Cross-sectional SEM photographs of patterned photoresist partially etched in (a) (C_4F_8/90%Ar)/10%N_2 and (b) (C_4F_8/90%Ar)/5%O_2 plasmas after O_2 plasma ashing. The experimental parameters were same as in Fig. 15. The average deposition rates underneath the roof in 5 minutes are 0.2 and 0.18 nm/min for N_2 and O_2 addition, respectively.

The addition of both N_2 and O_2 to C_4F_8/90%Ar on trench sidewall angle was studied. As discussed above, 10% N_2 was added since it enables the lowest FC film deposition rate for the (C_4F_8/90%Ar)/N_2 gas chemistry. Only 5% O_2 was added to C_4F_8/90%Ar due to its aggressive attack of the low k material. Figure 4.14 shows cross-sectional SEM micrographs of OSG films partially etched at 30 mTorr using (C_4F_8/90%Ar)/10%N_2 and (C_4F_8/90%Ar)/5%O_2 plasma, followed by in-situ ashing using an O_2 plasma. The experimental conditions for etching and ashing are the same as those employed for the C_4F_8/90%Ar experiments. The average FC deposition rates in 5 minutes measured in the completely shadowed region are 0.2 and 0.18 nm/min for N_2 and O_2 addition to C_4F_8/90%Ar, respectively, which is less than the average deposition rate measured for C_4F_8/90%Ar of 0.3 nm/min. A more vertical etching profile and smoother sidewalls are seen for the trenches formed in (C_4F_8/90%Ar)/10%N_2 discharges as compared to C_4F_8/90%Ar (see Figure 4.13 (b)), and can be related to the reduction of the deposited FC film thickness. Unfortunately, a side effect of nitrogen addition is also shown in Figure 4.14 (a): The modified photoresist which likely contains N_2 cannot be easily removed in an O_2 plasma. A much thinner FC film thickness is observed when O_2 is added. This leads to a more vertical etching profile (see Figure 4.14 (b)), but also produces profile damage near the bottom and at the sidewall of the OSG trench.

More severe FC deposition is observed at 80 mTorr due to the increased residence time of the CF_x film precursors. For (C_4F_8/90%Ar)/10%N_2 plasma, no etching was possible using the above conditions. For C_4F_8/90%Ar and

(C_4F_8/90%Ar)/5%O_2 plasmas operated at 80 mTorr etching was possible, and sidewall angles will be reported. At 80 mTorr, poor etching profiles are seen in the SEM micrographs, but will not be shown.

4.3.3. Discussion: Correlation of Gap Structure Data with SEM Data

Table 4.2 gives a summary of the most important observations made by gap structure measurement and SEM measurement in C_4F_8/Ar, (C_4F_8/Ar)/O_2 and (C_4F_8/Ar)/N_2 plasmas. Overall, in order of C_4F_8/Ar, (C_4F_8/Ar)/N_2 and (C_4F_8/Ar)/O_2, the FC film thickness and F/C ratio of the films deposited in the gap structure decrease and the sidewall angle measured by SEM increase. For all gas chemistries, the etching processes still need to be optimized. In particular, we observe low k material damage and undercut for C_4F_8/Ar and (C_4F_8/Ar)/O_2 discharges, and a difficulty for (C_4F_8/Ar)/N_2 discharges to remove the modified photoresist layer by the in-situ ashing process.

	FC Film Thickness (nm)	F/C ratio of FC Film	OSG Sidewall Angle (Degree)	Ashed Pattern
C_4F_8/90%Ar	1.5	2.862	83	Sidewall damage
(C_4F_8/90%Ar)/10%N_2	1	2.254	84	Modified Resist
(C_4F_8/90%Ar)/5%O_2	0.9	1.909	86	Sidewall damage

Table 4.2: Summary of the observations by gap structure and SEM measurements.

Time dependent FC film growth rates indicate that the relationship between DR_{gap}/ER_{trench} ratio and the sidewall angle depends on the time scale chosen for comparison. For all pattern transfer experiments in this study, the time scales range from 4 to 7 minutes. However, time dependent FC film growth rates also show that the FC film thickness only increases slightly after 2 minutes. Thus, the total FC film thickness deposited at 4 minutes is close to that measured after 7 minutes of plasma processing. For convenience, the FC film thickness measured after 5 minutes of plasma processing is used for the data analysis, along with the the actual process time of the pattern transfer. In general, the etch rate during pattern transfer changes with aspect ratio. ER_{trench} is the average etch rate and obtained from the trench depth measured using the SEM photographs and the actual pattern transfer time.

The FC deposition behavior under the roof has been described in a previous paper from this group[2=4.24]. Briefly, in the exposed region, the film thickness is essentially uniform. In the transition region, the film thickness starts to decrease slowly near the edge of the roof wafer, and decreases strongly underneath the roof wafer. In the completely shadowed region, the FC film thickness decreases slightly with the distance. Overall, the FC film thickness decreases continuously with distance. This is similar to the observation on the sidewall of the feature. To quantitatively simulate the FC deposition on the sidewall, the effect of aspect ratio should be considered**.** Therefore, the position underneath the roof used for analysis should be carefully selected. As shown in Fig. 1, the distance from the edge of the roof to the position used to measure the FC deposition rate is L, while the height of

the gap is H. In our experiment, the ratio between L and H is selected to be same as the aspect ratio of the features etched.

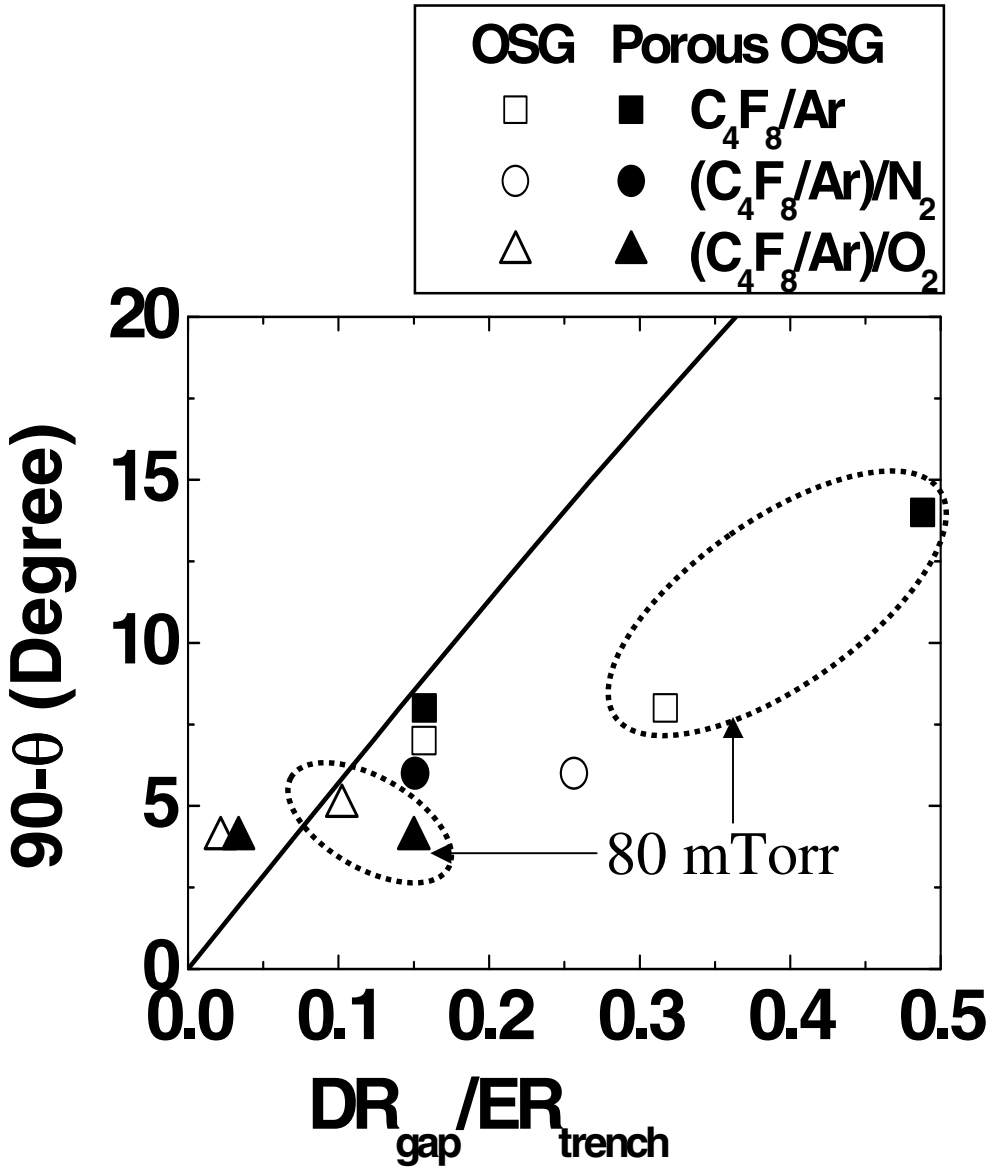

Fig. 4.15: Correlation DR_{gap}/ER_{trench} ratio with "90 degrees minus the sidewall angle", which is the film deposition induced change in the sidewall angle from vertical.

Figure 4.15 compares the sidewall angles acquired with trenches etched into OSG and porous OSG thin films with the ratio DR_{gap}/ER_{trench} obtained from the measurements of DR_{gap} (employing the gap structure) and ER_{trench} (using the SEM profiles). The sidewall angles were measured from the corresponding SEM photographs. Trenches were produced using C_4F_8 based gas mixtures. The solid line is based on the simple model illustrated in Figure 4.2. Overall, for both OSG and porous OSG features, the measured sidewall angles correlate qualitatively with the DR_{gap}/ER_{trench} ratio, consistent with the notion that the sidewall angle is controlled by FC film deposition on the feature sidewall. The lower the FC deposition rate, the more vertical the trench sidewall.

The correlation of sidewall angle with the ratio DR_{gap}/ER_{trench} deviates from the simple model (solid line) in two areas. One, for very small DR_{gap}/ER_{trench} ratios, the measured sidewall angle is less vertical than expected from the model. Second, for very large DR_{gap}/ER_{trench} ratios, the measured sidewall angle is more vertical than predicted by the model. The simplified model is based on the assumption that the etching profile of the low k material is only affected by the FC film deposition rate at the sidewall (lateral deposition rate), along with the value of the vertical etch rate of the low k material. The etch rate ER_{trench} of the low k material used for Figure 4.15 is obtained from the etch depth in the SEM image divided by the actual etch time, and should correctly describe the average etching rates for different etching chemistries that were examined. On the other hand, the FC film deposition rate on the sidewall is estimated from the FC deposition rate measured by the gap structure rather than using

the deposition rate for the actual features. The fact that for small DR_{gap}/ER_{trench} ratios, the actual sidewall angle is less vertical than expected from the DR_{gap}/ER_{trench} ratio indicates that the deposition rate measured using the gap structure is lower than the actual deposition rate on the sidewall. This is seen for trenches etched using (C_4F_8/90%Ar)/5%O_2 plasmas at low pressures. For this gas chemistry little FC film deposition takes place. For etching chemistries with little FC film deposition, redeposition of etch product can start to dominate film deposition on the feature sidewalls, and affect the resulting sidewall profile angle. For these conditions the deposition rates estimated using the gap structure approach deviate strongly from actual sidewall deposition rates. Conversely, for large DR_{gap}/ER_{trench} ratios, Figure 4.15 shows that the actual sidewall angle is greater than expected based on the DR_{gap}/ER_{trench} ratio. This indicates that the deposition rate measured using the gap structure overestimates the actual deposition rate on the sidewall. This is most evident for the C_4F_8/Ar plasma operated at 80 mTorr, which produced the most severe FC film deposition for all the pattern transfer processes examined. The fact that gap structure deposition rate DR_{gap} cannot be used in that condition to predict the actual trench sidewall angle can be attributed to the fact that for strongly sloped trench sidewalls, ion induced etching of the deposited FC films can become important. Ion induced etching is not present for the film deposition underneath the gap structure, giving a value for DR_{gap} that is higher than that the FC deposition rate on the actual sidewall, and explaining the changed profile angle. Non-uniform FC film deposition, e.g. severe FC film deposition near the top of the trench, may also contribute to the deviation.

The gap structure approach captures several important surface chemical trends. At the same time, systematic errors may be introduced by this approach. One of the most important may be that for surfaces without ion bombardment, the FC growth rate is strongly time dependent, which is ignored in the simple model described. It is also possible that for actual features some ion bombardment due to the slightly deflected ions is important, especially near the top part of the trench. This suggests that the gap structure approach may be most applicable to study sidewall processes and predict the sidewall angle of very high aspect ratio features. In addition, errors may be introduced when the deposition rate becomes material dependent, e.g. for nanoporous dielectrics [4.7-4.9]. For the present study this effect does not appear important since the overall FC deposition behavior on OSG is consistent with observations made for Si, except that the FC film formation rate is slightly lower.

4.4. CONCLUSION

A small gap structure has been used to simulate sidewall surface processes occurring during high aspect ratio trench etching. The lack of ion bombardment underneath the gap structure and the need for FC film precursors to make a certain number of collisions with surfaces before they are incorporated in the growing film makes the completely shadowed region similar to a trench sidewall. Three gas chemistries, C_4F_8/Ar, (C_4F_8/Ar)/N_2 and (C_4F_8/Ar)/O_2, with different overall FC chemistries and deposition rates were used for this study. We also report XPS studies of FC films deposited in C_4F_8/Ar, (C_4F_8/Ar)/N_2 and (C_4F_8/Ar)/O_2 plasmas using a gap

structure. A "carbon depletion" effect of the FC film is noted when N_2 or O_2 were added to C_4F_8/Ar. This indicates the addition of N_2 or O_2 not only leads to the decrease of FC film thickness, but also changes the composition of the deposited FC film. A comparison of the deviation from a vertical sidewall, "90^0-θ", with the measured DR_{gap}/ER_{trench} for these important plasma etching chemistries for OSG and porous OSG materials show that the deposition rate measured for the gap structure can be used to qualitatively predict the trench sidewall angles that are formed. We show that a limitation of this method is seen for very low FC film deposition rates, and can be attributed to the lack of etch product redeposition for the gap structure. In addition, when the sidewall angle becomes very large, ion-induced etching of the FC film deposited on the sloped sidewalls can reduce the effective FC film thickness. This leads to a more vertical sidewall profile angle than expected based on the measured gap structure deposition rate DR_{gap}.

ACKNOWLEDGMENTS

Financial support of this work by the Semiconductor Research Corporation's Center for Advanced Interconnect Sciences and Technology (CAIST) and Lam Research Corporation is gratefully acknowledged. We also thank International SEMATECH and Texas Instruments for supply of the materials used in this study.

Chapter 5: CF_4/H_2 Capacitively Coupled Plasmas: Studies of Fluorocarbon Film Deposition Employing A Gap Structure and Correlation with Etched Trench Sidewall Angle

To be submitted to J. Vac. Sci. Technol. A, 2006

Li Ling, X. Hua, G. S. Oehrlein, E. A. Hudson and P. Jiang

Abstract:

We describe studies of CF_4/H_2 based pattern transfer and related surface chemical studies in a dual frequency (40.68/4 MHz) capacitively coupled plasma (CCP) reactor, which is also compared with the previous studies in C_4F_8/Ar based discharges in same system. In current studies, a small gap structure has been used to study surface chemistry aspects of fluorocarbon (FC) film deposition for CF_4/H_2 plasmas and to simulate FC film deposited on feature sidewalls during pattern transfer. The small gap structure provides a completely shadowed region without direct ion bombardment, similar to sidewall surfaces of trench patterns. On both trench sidewalls and the shadowed surface portions of the small gap structure, very thin FC layers are formed by arrival of reactive neutrals. The lack of ion bombardment for the shielded deposition also increases the retention of the chemical structure of the FC film precursors in the deposited films. For CF_4/H_2 discharges, the composition and bonding of deposited FC films are determined as a function of processing conditions using ellipsometry and X-ray photoemission spectroscopy (XPS). The surface chemistry of FC film deposited in the completely shadowed region depends strongly

on discharge chemistry. During etching, film deposition on the sidewall produces a characteristic sidewall slope angle and also can modify the surface characteristics of low k dielectrics. We show that the feature sidewall angles formed for both CF_4/H_2 and C_4F_8/Ar gas chemistries qualitatively correlate with the deposition rates measured for the completely shadowed surfaces of the gap structure: The lower the FC deposition rate on the sidewall, the more vertical the trench sidewall.

5.1. INTRODUCTION

Fluorocarbon gases have been extensively used in the microelectronics industry for etching low k and ultra-low k materials[5.1-5.26]. During etching process, a steady state FC film can be formed on top of low k material. This thin FC film determines the etch rate, etch selectivity and morphology of the low k material[5.7-5.9, 5.14, 5.17]. At the same time, the thin FC film can also be formed on the sidewall of the trench during the pattern transfer and affect the etching profile[5.15-5.18]. Therefore, during the subsequent ashing process, the FC film can react with the deposited FC film on the sidewall and thus cause the damage of the low k film[5.11, 5.15-5.18, 5.27]. If the polymer film is not completely removed, it can also cause other issues for the subsequent device integration, such as fluorine penetration etc.[5.28, 5.29]. Therefore, a careful control of the FC film deposition during etching process is critical.

There is evidence that the properties of the thin FC films are strongly dependent on the gas composition. Previously, we described the use of a gap structure to investigate the influence of ion bombardment on the composition of deposited FC films and to simulate FC deposition on feature sidewalls during pattern transfer in the C_4F_8/Ar based discharges in this capacitively coupled plasma system[27]. The experimental results clearly showed that the ratio of FC deposition rate under the "roof" to the low k material etch rate in the exposed region strongly correlates to the sidewall angle of the etched feature. But in C_4F_8/Ar based discharges, a strong FC deposition is observed on the sidewall of the feature, which leads to the low k material damage in the following ash process. Although O_2 addition can limit the FC deposition, the strong damage of low k material induced by oxygen radical makes it

inapplicable. In the current investigation we have extended this work to the CF_4/H_2 gas chemistry to reduce the FC film deposition. The better etching profile and less damage is observed in this gas chemistry. Therefore, CF_4/H_2 based gas chemistry is a promising candidate for the low k and ultra-low k material etching and also the gap structure can be used to examine surface chemical aspects of sidewall deposition processes controlling etching profiles[5.4-5.6].

5.2. EXPERIMENTAL

The reactor used in this study is a home-built dual frequency capacitively coupled plasma (DF-CCP) reactor, which has been described in an earlier article from this group[5.26, 5.27]. Briefly, it consists of two electrodes (125 mm diameter) to control the plasma generation and ion bombardment energies at the substrate, separately. The gap between the electrodes is 50 mm. The top electrode features a showerhead design for gas distribution and is powered using a 40.68 MHz power supply. Typical powers applied are in the range of 100 to 300 W. The bottom electrode can be powered by a 4 MHz RF power supply. For this study no bias is applied. The wafer is mounted on the cooled bottom electrode and is kept at 10^oC by a low temperature circulator.

CF_4 and CF_4/H_2 plasmas were employed for the present etching and FC film deposition studies. For all experiments described here the total gas flow into the reactor was set at 40 sccm (standard cubic centimeters per minute), and the pressure varied between 20 and 80 mTorr. Both Organosilicate glass (OSG) and porous OSG films were patterned by transferring line and space features formed in 300 nm thick 248 nm photoresist on top of 90 nm bottom antireflection coating (BARC) using

these gas chemistries. A SiC etch stop layer was employed. The applied source power was 200 W and the bias power was kept at 100 W. The OSG and porous OSG films were 20% over-etched. After etching, photoresist was ashed using an in-situ O_2 plasma process in the same reactor. The conditions for the in-situ ashing treatment were: A O_2 gas flow rate of 40 sccm, a pressure of 30 mTorr, and the source power was 200 W. No RF bias was applied.

The gap structure experiments were performed as following. The gap structure used for this study has been extensively described in the previous papers of this group[5.13, 5.14]. FC films were deposited in both exposed and completely shadowed regions for discharges operated without RF bias of the substrate. After the experiments, the base wafer was removed from the plasma chamber and placed on a motor driven stage to determine by ellipsometry (632.8 nm He/Ne laser) the thickness and the refractive index of the deposited FC film as a function of position for both exposed and completely shadowed regions. Deposited FC films on selected specimens for which air exposure was minimized were also analyzed using X-ray photoelectron spectroscopy and enabled determination of surface composition and chemical bonding. These measurements were performed at a 90^o electron take-off angle using a nonmonochromatized Mg K-alpha X-ray source (1253.6 eV).

5.3. RESULTS AND DISCUSSION

5.3.1. Time Dependent FC Film Growth

It is well known that for plasma deposited FC films, chemistry and structure depend strongly on whether the growing film is exposed to ion bombardment during

deposition[5.7, 5.30-5.32]. In general, the deposition rates and the corresponding film properties of the FC films, i.e. bonding, structure etc., don't show evident changes as a function of time when surfaces are exposed to ion bombardment during FC film growth. Previous studies in C_4F_8/Ar gas chemistries showed that in the completely shadowed region (the region without ion bombardment), the FC film deposition rate does show a strong decrease as a function of time[5.27]. At the same time, the properties of FC film also change with the time scale for the film growth. It indicates that without exposure to ion bombardment, FC film growth shows a strong interface effect. For the studies in CF_4/H_2 gas chemistries, a systematic measurement of FC film deposition without ion bombardment was also undertaken by employing the gap structure.

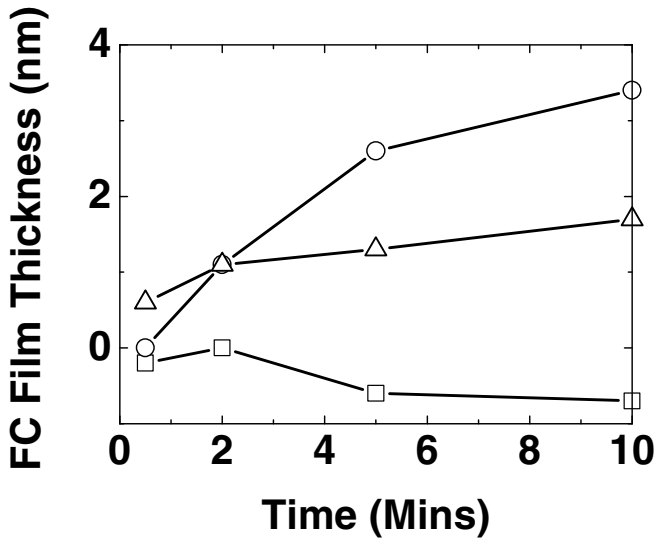

Fig. 5.1: Time dependent FC film thickness obtained in the completely shadowed region for CF_4 ( ), CF_4/40%H_2 (O) and C_4F_8/90%Ar (Δ). The other experimental parameters were: 200 W capacitive power, 20 mTorr for CF_4, CF_4/40%H_2 and 30 mTorr for C_4F_8/90%Ar.

Fig. 5.1 shows the variation of FC film thickness with time under the roof for CF_4 and CF_4/40%H_2 plasmas. For comparison, a FC film growth curve for C_4F_8/90%Ar plasma is included. A major difference is clearly shown between pure CF_4 and C_4F_8/90%Ar due to the different deposition ability of CF_4 and C_4F_8. It is apparent that fluorocarbon-based glow discharge will contain both etchant species such as F and CF_x radicals ($0<x<3$) and other FC combinations that tend to deposit on surfaces forming thin polymeric films. As indicated by J. W. Coburn and H. F. Winters[5.33], the discharge can be operated in an etching or polymerization mode, depending on the stoichiometry of the feed gases (F/C ratio in the fluorocrabon gas chemsitries) at a fixed bias voltage of the substrate. For pure CF_4, due to its high F/C ratio, a significant amount of fluorine is produced and no FC deposition is observed under the roof. Negative film thickness indicates that the native oxide on the Si is removed. While for C_4F_8, there are much less fluorine radicals in the discharge, which leads to the continuous growth of the FC film. The addition of H_2 can lead to the lower F/C ratio of the feed gas because hydrogen can scavenge the fluorine in the plasma and thus leads to the change of dominant species in the gas phase. Therefore, the deposition behavior of CF_4/H_2 is quite similar to that of C_4F_8/90%Ar. The continuous growth of the FC film and decreased FC deposition rates are observed. This is shown in Fig. 5.1. This observation suggests that when low F/C ratio gas chemistry is used for the pattern transfer, FC deposition on trench sidewalls may be most important as fresh surface elements are initially exposed[5.27]. There are significant differences between CF_4/H_2 and C_4F_8/Ar gas chemistries. For C_4F_8/Ar, the

FC growth is dominant in the beginning and only shows a small increase afterwards; while for CF_4/H_2, although the decreased FC deposition rate is observed, FC deposition rate is not saturated up to 10 minutes. It is much longer than the usual time scale for the pattern transfer, which is around 4 minutes. It suggests that the FC growth behaviors on the sidewall during the pattern transfer are different in these two gas chemistries and there is less importance of plasma exposure of fresh element in CF_4/H_2 plasma.

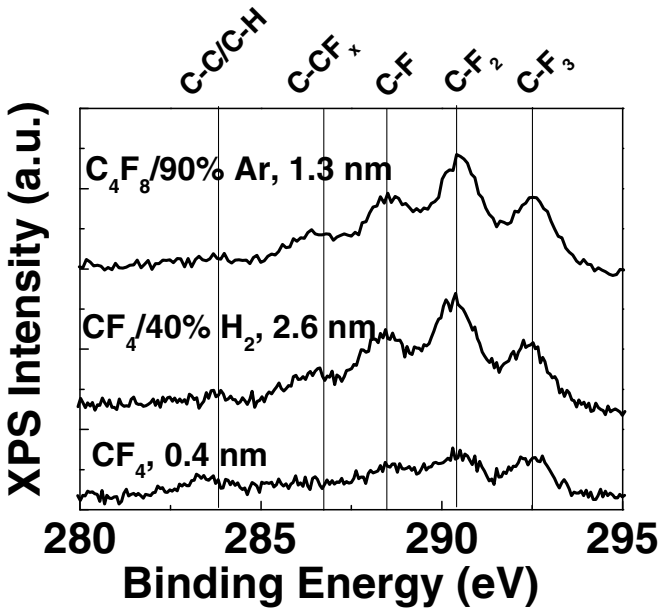

Fig. 5.2: C (1s) photoemission spectra of FC layer in the completely shadowed region on Si substrate in CF_4, $CF_4/40\%H_2$ and $C_4F_8/90\%$Ar plasmas. The experimental parameters were same as Fig. 5.1.

5.3.2. Surface Analysis of Deposited FC Film by XPS

To examine the surface chemistry of FC film deposited on the sidewall during the pattern transfer, FC films deposited underneath the gap structure were examined

by XPS. Fig. 5.2 shows the XPS spectra of the FC layers deposited in both CF_4 and CF_4/40%H_2 plasma, which are compared with the spectrum obtained in C_4F_8/90%Ar. The experimental conditions were 200 W source power and no bias power, 20 mTorr for CF_4 related gas chemistry and 30 mTorr for C_4F_8/Ar. The time used for these depositions is 5 minutes due to the low deposition rate measured underneath the roof. The FC film thicknesses measured by ellipsometry are also marked in Fig. 5.2.

For films deposited in pure CF_4 discharges, the intensities of all C-F_x peaks are much lower than those seen in other two gas chemistries. It is similar to the steady state FC films formed in the etching experiment. In this discharge, the C-F_2 and C-F_3 peaks are still the highest peaks and distinguishable, which contribute to a high F/C ratio. For FC film deposited using CF_4/40%H_2, a strong overall increase in C (1s) intensity is seen. This is consistent with the much greater FC film thickness (2.6 nm) measured for this specimen by ellipsometry. The C (1s) spectrum obtained using CF_4/40%H_2 plasma shows the conventional peaks associated with FC films[5.34], i.e. four peaks (in order of increasing binding energy), assigned to C-CF_x (x=1,2,3), C-F, C-F_2, and C-F_3. In this condition, C-F_2 bonding intensity dominates the C (1s) spectra, C-F_3 and C-F bonding intensities are comparable, and the C-CF_x bonding intensity is weak.

Fig. 5.2 also shows that the XPS spectra obtained in both C_4F_8/90%Ar and CF_4/40%H_2 discharges are quite similar. In C_4F_8/Ar plasma, Ar addition can increase the dissociation of the C_4F_8 and in CF_4/H_2 discharge, hydrogen addition leads to the depletion of fluorine and thus increase the intensity of CF_x radicals. The similar spectra obtained in C_4F_8 and CF_4 related gas chemistries by different gas addition are

the result of the different molecular structure between CF_4 and C_4F_8[5.34]. Combined with the FC film thickness data (2.6 nm at 5 minutes deposition), a sloped sidewall is expected when feature is etched in CF_4/40%H_2 plasma.

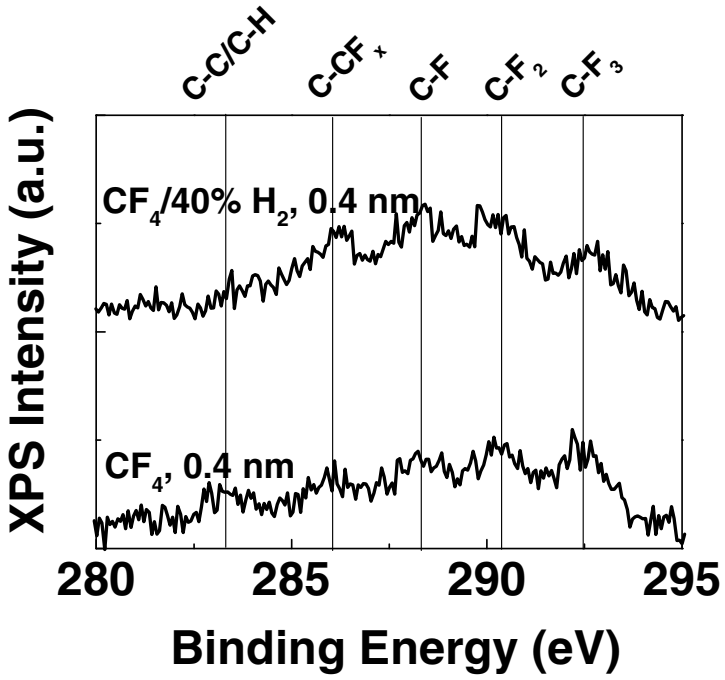

Fig. 5.3: C (1s) photoemission spectra of FC layer in the completely shadowed region on Si substrate in CF_4 and CF_4/40%H_2 plasmas. The experimental parameters were same as Fig. 5.1.

Figure 5.3 compares XPS spectra of FC layers deposited in the completely shadowed region using CF_4 and CF_4/40%H_2 plasmas, but now with a RF bias of 100 W applied. The application of the bias leads to the etching outside of the roof wafer. Therefore, very thin FC films are deposited in the completely shadowed region for both pure CF_4 and CF_4/40% H_2 discharges. The greater change of FC film thickness is observed in CF_4/40%H_2 plasmas than in pure CF_4 plasmas due to the global

depletion of FC deposition precursors as a result of the outside etching process. The change of FC film thickness with bias is not so evident in C_4F_8/Ar plasma due to the stronger deposition ability of C_4F_8 and thus a large amount of deposition precursors. For pure CF_4 plasma, there is little change of the C (1s) spectrum when an RF bias is applied relative to deposition without RF bias. While for CF_4/40%H_2 plasmas, the C (1s) intensity is also strongly changed. All four FC related peaks, C-CF_x (x=1,2,3), C-F, C-F_2, and C-F_3, are of comparable intensity. This indicates that the FC film deposition in CF_4/H_2 gas chemistries can be easily affected due to the much less FC precursors. Therefore, it suggests that FC film growth on the feature sidewall during pattern transfer process may be easily affected by the properties of the mask material.

5.3.3. Etching Profile Analysis by SEM

Figure 5.4 shows the cross-sectional secondary electron micrographs of OSG trenches etched in CF_4 plasma and ashed in O_2 plasma. They are compared with features produced using C_4F_8 containing gas chemistries. When pattern is etched in CF_4 discharge, much less FC deposition on the sidewall is observed, and a smoother sidewall was produced. At the same time, no damage on the sidewall and no undercut between the low-k material and the etch stop layer, which are pronounced for the features produced using C_4F_8 contained gas chemistries, is observed in the present condition. The fact that much less FC deposition occurs on the sidewalls of features using CF_4 etching processes can be explained by the higher F/C ratio of CF_4 and a lower propensity to produce FC film precursors. It is consistent with the FC

deposition rate measurement in the completely shadowed region. The SiC etch stop layer is attacked due to overetching.

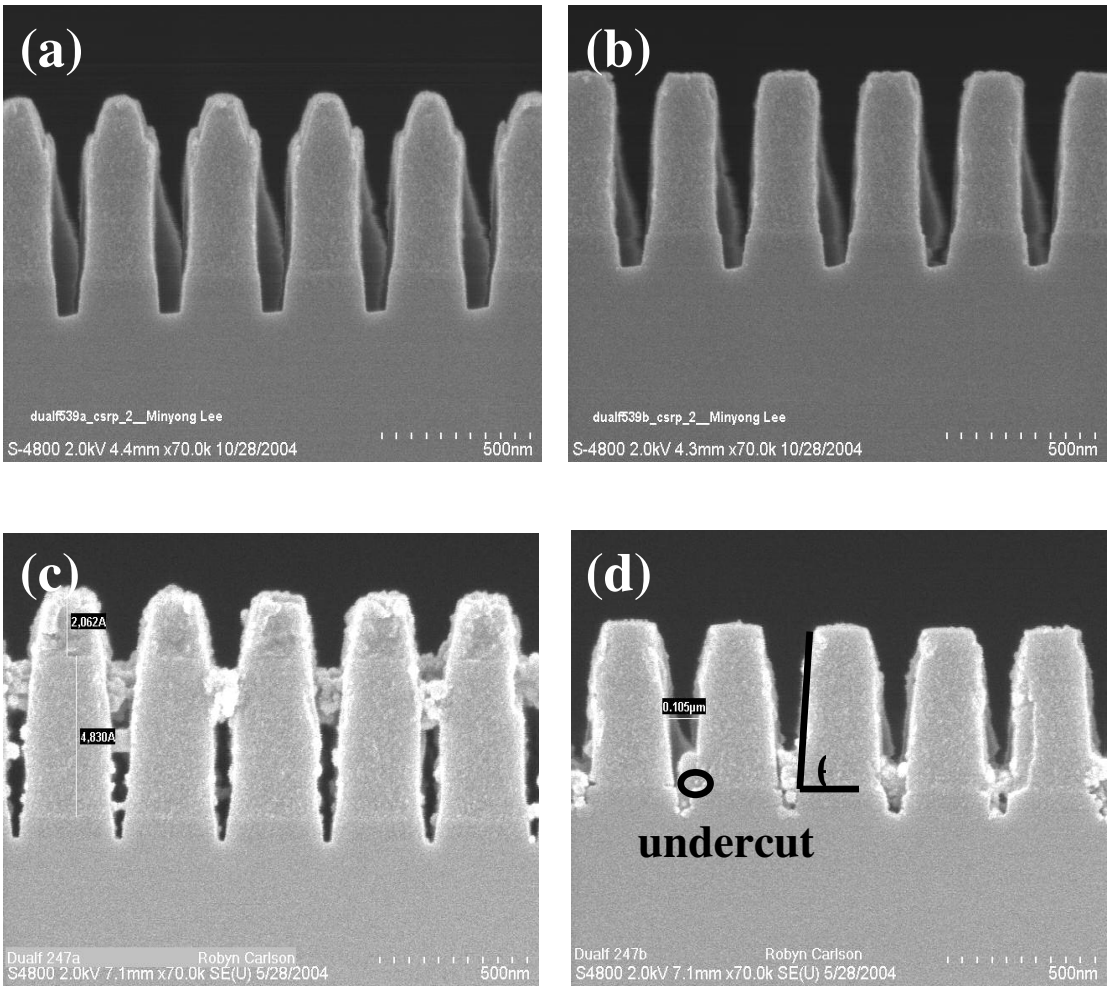

Fig. 5.4: Cross-sectional SEM photographs of patterned photoresist partially etched in CF_4 plasma (a) before and (b) after O_2 plasma ashing and in C_4F_8/90%Ar plasma (c) before and (d) after O_2 plasma ashing. The experimental parameters for plasma etching were same as Fig. 5.1, except that 100 W bias power is applied. For O_2 ashing, the experimental conditions are 30 mTorr, 200 W capacitive power and without bias.

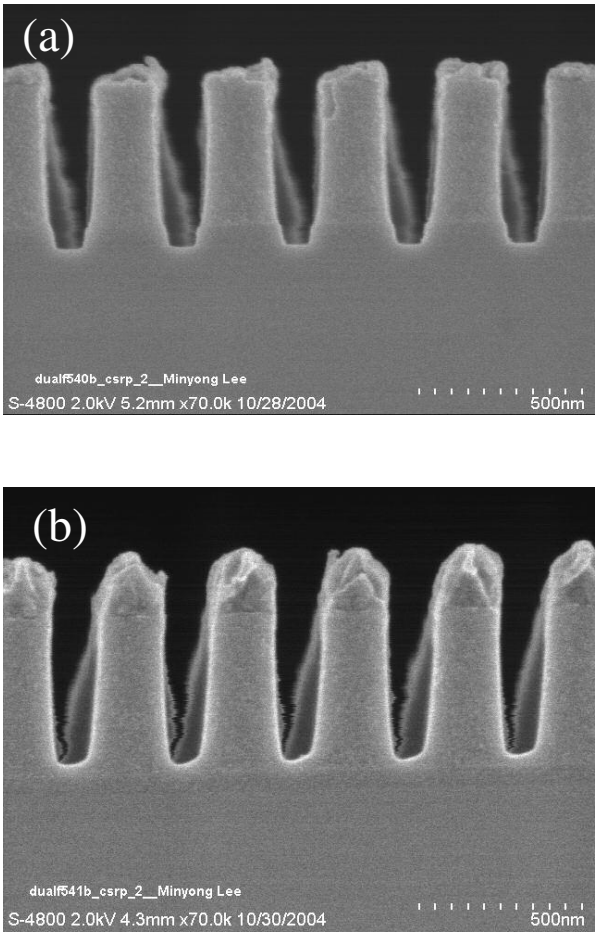

Fig. 5.5: Cross-sectional SEM photographs of patterned photoresist partially etched in (a) CF_4/20%H_2 and (b) CF_4/40%H_2 plasma. The experimental parameters were same as those for pure CF_4 experiment in Fig. 5.4.

H_2 addition to CF_4 can lead to the increase of the FC film deposition on the surface, as discussed in the previous section. Fig. 5.5 (a) and (b) show the corresponding SEM images obtained for patterns etched using 20%H_2 and 40%H_2 addition to CF_4, respectively. From the SEM images it appears that the best etching

profile can be obtained with CF_4/20% H_2 gas mixtures. With further H_2 addition, the etching profile begins to slope. In the latter case, the etching profile is quite similar to that seen for C_4F_8/90%Ar plasmas. It is consistent with the expectation from the data obtained by gap structure. It suggests that the accurate control of the radical species is required by the production of the vertical etching profile. The change of sidewall angle with H_2 addition is consistent with the previous observation in the C_4F_8 based gas chemistries: The lower the FC deposition rate on the sidewall, the more vertical the trench sidewall.

For all patterns produced using CF_4 based chemistries, no sidewall damage is observed after both plasma etching and O_2 ashing process. For C_4F_8 based chemistries, no sidewall damage is observed right after the plasma and the damage is induced after the O_2 ashing. The most significant difference between two gas chemistries is the FC deposition ability. This suggests that the sidewall damage is caused by the FC deposited during etching process reacting with the O_2 plasma during ashing process. But there are some interesting phenomena observed in CF_4/H_2 discharges: One is residual resist left on the etched patterns after the ashing process. This is also observed on the patterned porous OSG sample and it becomes more severe with H_2 addition. It indicates a modification of the photoresist during the etching process. The mechanism that leads to the ashing resistance of the exposed photoresist has not been established. Another interesting phenomenon is all the patterns etched in the CF_4 based chemistries are not symmetric, which is not observed in the C_4F_8 based chemistries. It may be because the pump is installed on one side of the chamber. In CF_4 plasma, there is a much smaller film precursor flux and thus a much thinner film

deposited, which depends much more strongly on the plasma surface interactions. Therefore, this FC film deposition can be easily affected by the other factors.

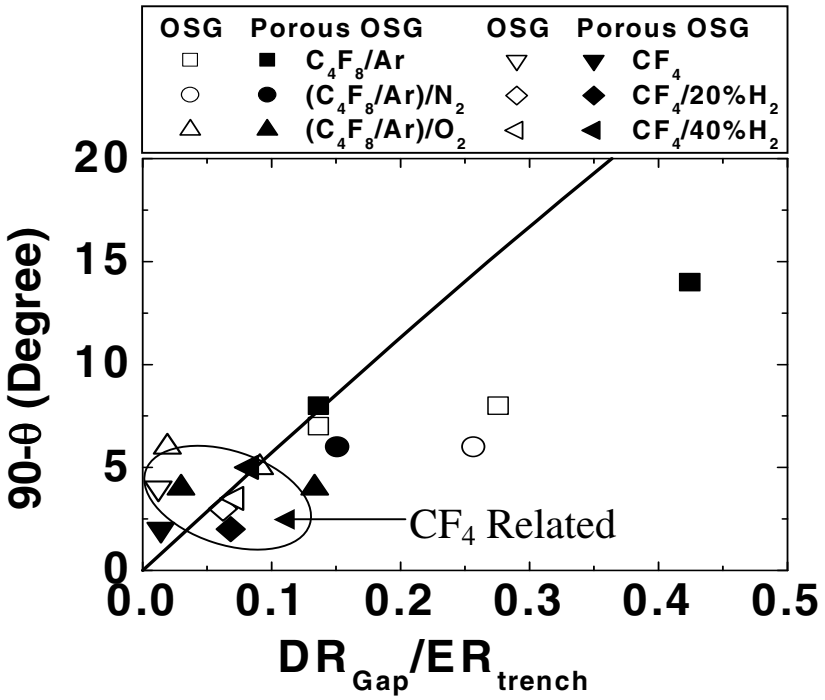

Fig. 5.6: Correlation DR_{gap}/ER_{trench} ratio with "90 degrees minus the sidewall angle", which is the film deposition induced change in the sidewall angle from vertical.

5.3.4. Correlation of Feature Sidewall Angle with DR_{gap}/ER_{trench} Ratio

Fig. 5.6 compares the sidewall angles acquired with trenches etched into OSG and porous OSG thin films with the ratio DR_{gap}/ER_{trench} ratio. The model and the calculation method have been extensively described in the previous paper about employing gap structure to simulate the sidewall angle in C_4F_8/Ar based plasma[5.27].

Briefly, only two dominant processes during the pattern transfer, FC deposition on the sidewall and low k material etch, are considered in this simple model. Generally, these two processes determine the sidewall angle. The FC deposition rate (DR_{gap}) was measured employing gap structure. The etch rate of trench (ER_{trench}) and the sidewall angles were measured from the corresponding SEM photographs. The solid line shows the theoretic relation between sidewall angle and the DR_{gap}/ER_{trench} ratio based on this simple model. Overall, for both OSG and porous OSG features, the measured sidewall angles correlate qualitatively with the DR_{gap}/ER_{trench} ratio. This reflects the fact that the sidewall angle is controlled by FC deposition on the sidewall. The lower the FC deposition rate, the more vertical the trench sidewall.

To get a more complete picture, the data obtained in C_4F_8/Ar based discharges is also included in Fig. 5.6. The data points in the circle are obtained in CF_4/H_2 discharges and the data outside are obtained in C_4F_8/Ar based plasma. Fig. 5.6 clearly shows the data obtained in CF_4/H_2 plasma has a much narrow range and usually has a much lower DR_{gap}/ER_{trench} ratio due to the limited FC deposition ability as discussed previously. Therefore, most data obtained in CF_4/H_2 discharges correlated well with the theoretical prediction. However, for very small DR_{gap}/ER_{trench} ratio, the measured sidewall angle is less vertical than expected from the model, same as the observation in the C_4F_8/Ar based plasma. At the same time, for very large DR_{gap}/ER_{trench} ratios, we observed that in the C_4F_8/Ar gas chemistry, the measured sidewall angle is more vertical than predicted by the model. This is not observed in the CF_4/H_2 discharges. The reason of the deviation has been pointed out in the previous paper about

employing gap structure to simulate the sidewall angle in C_4F_8/Ar based plasma[5.27]: The model only considers the two dominant processes during the feature etching. It couldn't include the effect of the etching product redeposition on the sidewall, which leads to the deviation at low DR_{gap}/ER_{trench} ratios and the effect of the increased ion bombardment on the sloped sidewall, which leads to the deviation at high DR_{gap}/ER_{trench} ratios. These comments are also supported by the current studies in the CF_4/H_2 plasma. But for this plasma, it shows some characteristics different from C_4F_8/Ar based plasma: One is for time dependent FC film growth in the completely shadowed region in $CF_4/40\%H_2$, the deposition rate remains a certain value even in 10 minutes deposition. This may introduce some error into the simulation. But the deposition rate did decrease with time, so this error should be subtle. Second, FC film deposition rate underneath the roof shows a difference at with and without bias condition. This is only observed in $CF_4/40\%H_2$, plasma and not seen in pure CF_4 plasma. For the sake of conciseness, the same calculation method is still used as previously[5.27]. Third, the asymmetry of the etching profile makes the analysis difficult. The sidewall angle used for the analysis is the average of sidewall angles from both left and right sides. The last two points are the unique observation in CF_4 related plasmas, which may be attributed to the different radical species and densities from the C_4F_8 based plasmas.

5.4. CONCLUSION

A small gap structure has been used to simulate sidewall surface processes occurring during high aspect ratio trench etching in a home-built dual frequency

capacitively coupled plasma reactor. The lack of ion bombardment underneath the gap structure and the need for FC film precursors to make a number of collisions with surfaces before they can be incorporated into the growing film makes this completely shadowed region similar to the sidewall of a trench. The gap structure is used to study the surface properties of FC films deposited in CF_4 and CF_4/H_2 discharges. When RF bias power is applied, the FC film properties showed a significant change. This phenomenon is not observed in C_4F_8/Ar gas chemistry. It indicates that for CF_4/H_2 related gas chemistries the etching process is easily affected by the outside factors due to much less FC precursors produced by CF_4. A comparison of the deviation from a vertical sidewall, "90^0-θ", with the measured DR_{gap}/ER_{trench} for important etching chemistries and OSG and porous OSG materials shows that the deposition rate measured for the gap structure can be used to qualitatively predict the trench sidewall angles formed. We also show that a limitation of this method is seen for very low FC film deposition rates, which can be attributed to the lack of etch product redeposition for the gap structure.

ACKNOWLEDGMENTS

Financial support of this work by the Semiconductor Research Corporation's Center for Advanced Interconnect Sciences and Technology (CAIST) and Lam Research Corporation is gratefully acknowledged. We also thank International SEMATECH and Texas Instruments for supply of the materials used in this study.

Chapter 6: Studies of Fluorocarbon Film Growth in C_4F_8/Ar Plasma by Employing a Gap Structure

To be submitted to J. Vac. Sci. Technol. A, 2006

Li Ling, X. Hua, L. Zheng, G. S. Oehrlein and E. A. Hudson

Abstract:

A small gap structure has been used to study surface chemistry aspects of fluorocarbon (FC) film deposition for FC plasmas produced in a mechanically confined dual-frequency capacitively coupled plasma (CCP) reactor. The small gap structure provides a completely shadowed region without direct ion bombardment. The lack of ion bombardment for the shielded deposition increases the retention of the chemical structure of the FC film precursors in the deposited films. For C_4F_8 and C_4F_8/Ar discharges, the deposition rate, composition and bonding of deposited FC films are determined as a function of processing conditions using ellipsometry and X-ray photoemission spectroscopy (XPS). The deposition rate and surface chemistry of FC film deposited in this region depend strongly on discharge chemistry. For pure C_4F_8 plasma at 80 mTorr, low power level and high pressure applied in this capacitively coupled plasma reduce the amount of energy that is available per C_4F_8 molecule. XPS measurement indicates that the FC film produced in the without ion bombardment condition shows nanoscale topography that differs markedly from films produced with simultaneous ion bombardment: Two distinct chemical surface portions are seen, one consisting primarily C-F_2 and C-F_3 bonding, and the other of

C-C or C-H bonding. This is supported by atomic force microscopy (AFM) measurement. The existence of the nanoscale topography can be eliminated by adding Ar and/or increasing the source power. Similar phenomenon is also observed by the corresponding studies in an inductively coupled plasma.

6.1. INTRODUCTION

FC films synthesized by FC plasma polymerization (such as C_4F_8) have been widely applied in the ULSI industry because of many useful properties including low dielectric constants, low vapor permeability, inhibition of bio-film formation, hydrophobicity, and oleophobicity (oil-repellency)[6.1-6.4]. It has been demonstrated that FC film properties can be modified by the careful control of the ion bombardment and the radical production. It is well known that the arrival of both ions and neutrals at the surface can contribute to FC deposition[6.5-6.22]. The most important role of ions in the FC film growth is the production of active site for the radical adhesion. At the same time, ions can lead to the radical production and contribute to the film growth at low energy by direct incorporation. As for the neutrals, CF and CF_2 radicals have been widely reported to be the important FC film precursors[6.17-6.19]. However some studies found thatCF_2 is not only the precursor of FC film growth, but also the product of ion bombardment on the FC film[6.20-6.22]. In this case, larger FC radical species, such as C_2F_6, C_3F_8, etc., play an important role in FC deposition. Therefore, understanding the different roles of individual neutrals and ions in FC film formation is critical. At the same time, the surface morphology and the properties of FC film, such as hydrophobic, oleophobic etc., are strongly dependent on the properties of substrate[6.13, 6.23-6.25]. This becomes more important when the deposited FC film is thin.

We previously described the use of a gap structure to investigate the influence of ion bombardment on the composition of deposited FC films and to simulate FC deposition on feature sidewalls during pattern transfer in capacitively coupled plasma[6.26]. As expected, the FC film bonding and composition shows strong

differences with and without ion bombardment in the plasma etching environment (with the application of bias). The difference of FC film properties plays an important role on the etch selectivity and etch profile control. In the current investigation we focused on the question of ion effects on FC film growth in the plasma deposition environment (without application of bias) by employing gap structure approach. At the same time, different parameters (e.g. power, pressure, gas composition etc.), which may affect the film growth, have been investigated. The corresponding studies in the inductively coupled plasma were also reported for comparison.

6.2. EXPERIMENTAL

Two reactors were used for the film growth study. One reactor is a home-built dual frequency capacitively coupled plasma reactor, which has been described in an earlier article from this group[6.26, 6.27]. Briefly, it consists of two electrodes to control the plasma generation and ion bombardment energies at the substrate separately. The gap between the two electrodes (125 mm diameter) is 50 mm. The electrodes are located in a stainless steel chamber with an inner diameter of 250 mm. The top electrode features a showerhead design for gas distribution and is powered using a 40.68 MHz power supply. Typical powers applied are in the range of 100 to 300 W. The bottom electrode can be powered by a 4 MHz RF power supply. For this study no bias is applied. The wafer is mounted on the cooled bottom electrode and is kept at 10^{o}C by a low temperature circulator. All experiments carried out in CCP were in discharges at pressures ranging from 30 to 80 mTorr, fed with 40 sccm (standard cubic centimeters per minute) total gas flow.

The other reactor, an inductively coupled plasma (ICP) reactor, is used for comparison and has been well described in an earlier articles from this group[6.28, 6.29]. Basically, a planar stove-like coil is placed on top of a quartz coupling window. The coil is powered using a 0–2000 W 13.56 MHz power supply. The silicon wafer is clamped to a 300 mm diameter electrostatic chuck that can be rf powered. The wafer is cooled to 10 °C by a low temperature circulator. For this work no bias is applied. Much higher pressure, 150 mTorr, was applied and maintained by 50 sccm gas flow rate.

To investigate the influence of ion bombardment on the composition of deposited FC films, a gap structure was used, which has been described in the earlier articles from this group[6.26]. It is shown in Figure 6.1. Briefly, the gap structure is formed by placing two rectangular spacers between a roof and a base wafer. The thickness of the Si spacers is 0.65 mm and the length of the roof wafer is about 5 cm. The high aspect ratio prevents the direct ion bombardment underneath the roof. The base wafer is designed to be 15 mm longer than the roof wafer, so that a part of the base wafer forms an exposed region (a region with direct ion bombardment), while the other part is underneath the roof wafer and forms a completely shadowed region (a region without ion bombardment). A transition region exists between the ion bombarded and the shielded areas. Since the FC film deposited in the fully shadowed region was thin (less than 10 nm), the native oxide on the silicon wafers used for FC film growth had been removed by etching in a 1% HF solution.

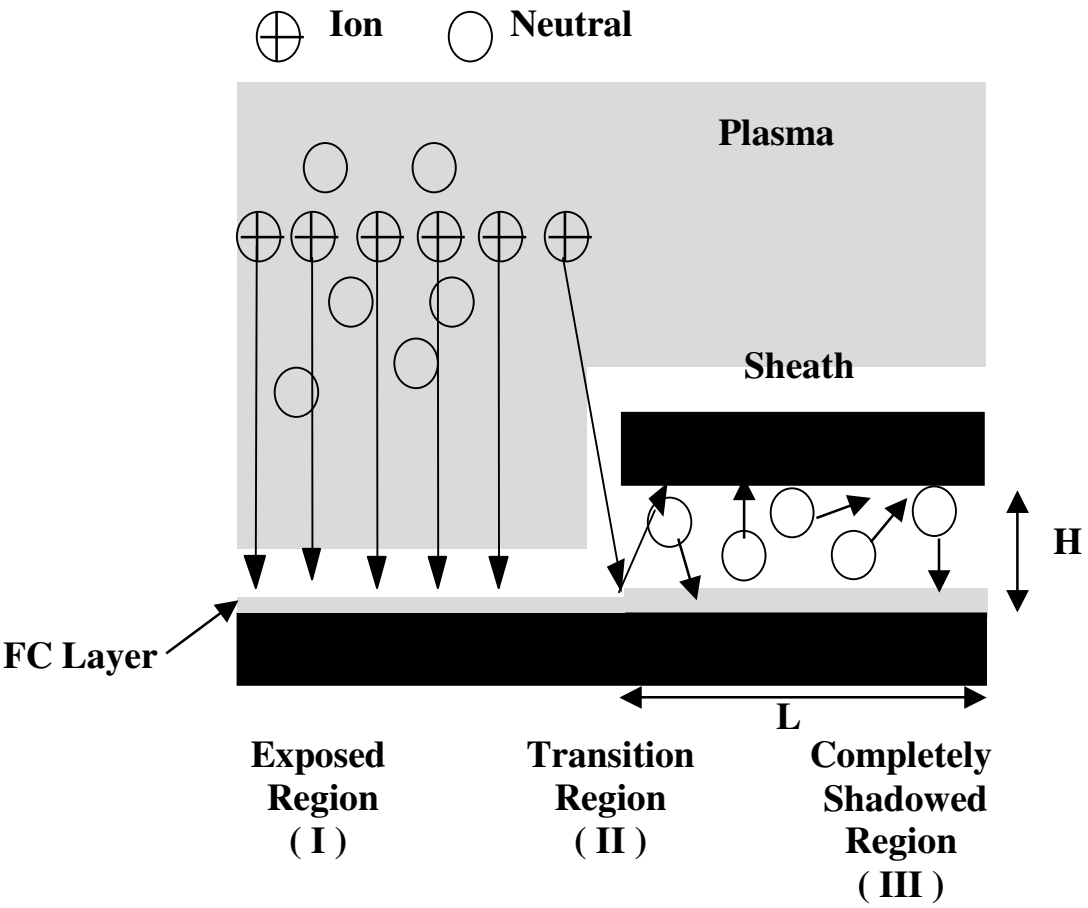

Fig. 6.1: Schematic of small gap structure used in this work.

Previous studies in ICP showed that the addition of Ar could lead to the shift of the electron energy distribution function and promote the dissociation of C_4F_8 molecules in the C_4F_8/Ar plasma[6.30-6.33]. The characterization data for this CCP system, which will be discussed later, showed that pure C_4F_8 and C_4F_8/90%Ar plasmas are two extreme conditions for the FC deposition. Therefore, these two gas chemistries were employed for the present FC film growth studies. FC films were deposited in both exposed and completely shadowed regions for discharges operated without RF bias of the substrate. After the experiment, the base wafer was placed on a

motor driven stage to determine by ellipsometry (638.2 nm He/Ne laser) the deposited FC film thickness and the refractive index as a function of position for exposed and completely shadowed regions. Deposited FC films on specimens for which the air exposure was minimized were also analyzed using X-ray photoelectron spectroscopy (XPS) and enabled surface composition and chemical bonding determination. These measurements were performed at a 90^{o} electron take-off angle using a nonmonochromatized Mg K-alpha X-ray source (1253.6 eV). Selected samples were analyzed by atomic force microscopy (AFM) and optical microscope to examine the morphology of the deposited FC film, and a goniometer to determine the water contact angle. For this water contact angle measurement, a 2 μL drop of distilled water was placed on the surface of the FC film by a microsyringe and then the water contact angle was measured. It was repeated 5 times to get the average.

6.3. RESULTS AND DISCUSSION

6.3.1. Characterization of Capacitively Coupled Plasma

The dual frequency CCP system used for this work has been characterized using a variety of techniques and present here selected results. We report measured ion current densities (ICD) and FC deposition rates for different source power levels, and compare these data with measruements obtained in a well characterized inductively coupled plasma system[6.30-6.33].

Figure 6.2 shows the dependence of ICD on the percentage of Ar added to C_4F_8. The plasma was operated at 300 W capacitive power and a pressures of 30 mTorr. The current was measured using a Langmuir probe, which is positioned at the

center of the chamber and biased to – 100V. A strong increase of ICD is observed as Ar is added to C_4F_8. For Ar-rich plasmas ionization becomes an important inelastic electron collision process, whereas for C_4F_8-rich discharges, dissociation processes may be most important. Addition of Ar can lead to a shift in the electron energy distribution function, which increases the degree of dissociation of C_4F_8 in C_4F_8/Ar plasma with a high proportion of Ar[6.30-6.33]. Overall, a higher ion/neutral flux ratio at the wafer surface will be seen when the Ar proportion in C_4F_8,/Ar becomes large, which is expected to lead to changes of the surface chemistry. The higher plasma density seen for Ar-rich C_4F_8/Ar discharges also will lead to a higher photon flux, and a higher flux of metastables to the surface, which can affect the dangling bond density at the surface of a growing FC film.

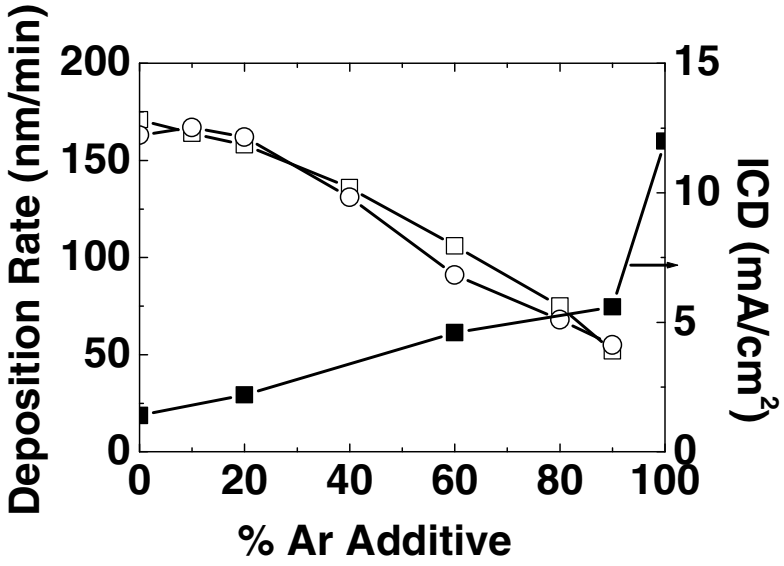

Fig. 6.2: FC deposition rate at both 30 ( ) and 80 (O) mTorr and ICD at 30 mTorr (■) measured as a function of Ar addition. The source power is 200 W for deposition measurement and 300 W for ICD measurement.

Figure 6.2 also displays the FC deposition rate as a function of Ar percentage in C_4F_8/Ar at both 30 and 80 mTorr. The applied source power is fixed at 200 W. The FC film deposition rates show a strong dependence on feedgas composition but are roughly the same for both pressures. At both pressures, the deposition rate remains nearly constant when up to 20% of Ar is added to C_4F_8. For 40% of Ar and higher, an overall trend towards much lower FC film deposition rates is observed, and may be explained by the limited supply of FC film precursors due to the reduced flow rate of C_4F_8.

To investigate the power coupling efficiency to the discharge, we compared measured ICD and FC deposition rate for both CCP system and data obtained in a well-characterized inductively coupled plasma (ICP) system in our lab[6.30-6.33]. Our ICP reactor was operated at higher source power and lower pressure, i.e. 600 W and 10 mTorr. Therefore, we compare the average energy required to produce one ion (expressed in eV/ion) for each reactor. This is shown in Figure 6.3 (a). We also show the energy cost to produce each CF_2 groups of FC film (expressed in eV/CF_2) for each system in Figure 6.3 (b). To simplify the calculation, we suppose the FC film to contain CF_2 groups only. This is because the dominant bonding in the deposited FC film is C-F_2, which will be shown in the XPS spectra and will be discussed later. The average energy necessary to produce each ion decreases with Ar addition. This is the result of the strongly increased ion density as Ar is added to C_4F_8/Ar. At the same time, the amount of FC film deposited per eV strongly increases for a high percentage of Ar in C_4F_8/Ar. Overall, we find that both the efficiency of producing ions and depositing FC films are similar for the CCP and ICP reactors if we employ Ar-rich

C_4F_8/Ar discharges. For pure C_4F_8 discharges, the ICP and CCP reactor show different efficiencies. For the ICP reactor we observe more efficient ionization and less efficient FC film deposition for each eV energy coupled to the plasma relative to the CCP reactor if we use pure C_4F_8 discharges.

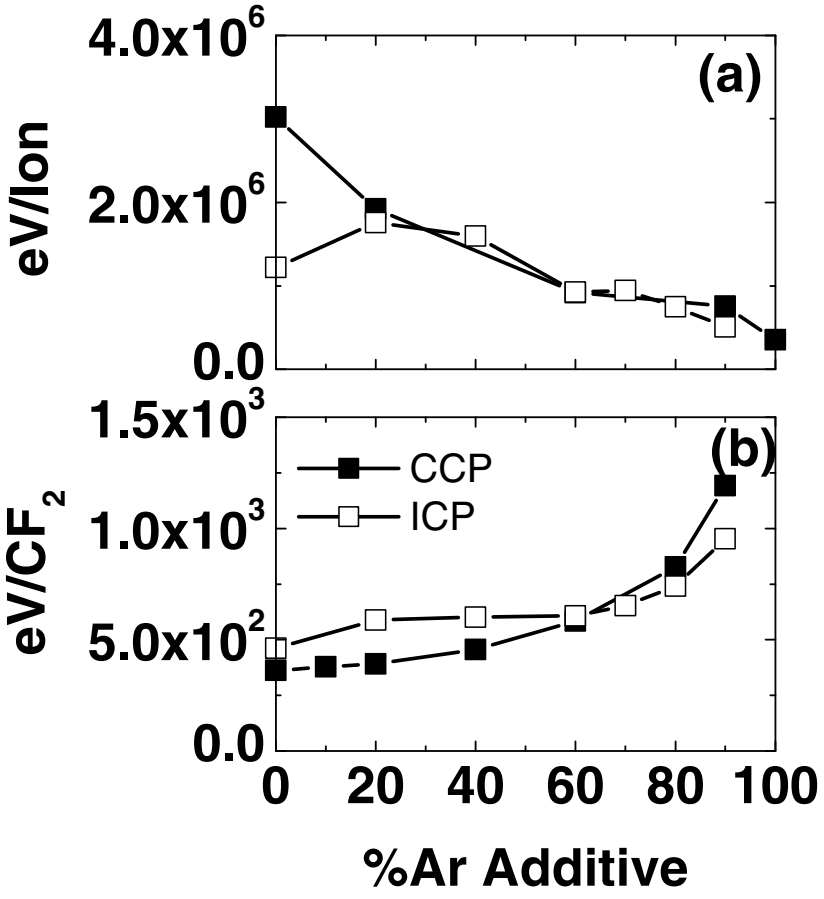

Fig. 6.3: (a) The calculated average energy required to produce each ion and (b) to deposit each CF_2 group in the FC film as a function of gas composition are compared in both capacitively (■) and inductively ( ) coupled plasma.

6.3.2. FC Deposition Rate

It is well known that for plasma deposited FC films, chemical structure strongly depends on the ion bombardment during deposition[6.5, 6.9, 6.34-6.36]. We first report the influence of the discharge chemistry and ion bombardment on the deposition rate measured in the CCP system. In Figure 6.4 we compare the FC deposition rates in the open area with that in the completely shadowed region for pure C_4F_8 and C_4F_8/90%Ar plasmas. For these experiments the gas flow was fixed at 40 sccm, the pressure was in the range of 30 to 80 mTorr and the applied source power was 200 W. No RF bias power was applied to the substrate. The deposition rate in the open area is measured directly by the in-situ ellipsometer and that in the completely shadowed region is the average deposition rate over 5 minutes measured by the ex-situ ellipsometer. The FC deposition rates measured for the ion exposed region are about two orders of magnitude higher than those measured for the completely shadowed region. This suggests that the FC deposition mechanism is strongly ion-assisted. For both substrate locations, the FC deposition rates vary strongly with gas chemistry and the dependence is similar. The higher deposition rate is observed for pure C_4F_8 plasmas. When a significant amount of Ar is added to C_4F_8, the FC deposition rate decreases significantly which can be explained by the largely reduced supply of C_4F_8 molecules to the reactor. FC deposition rate remains nearly constant with the increases of pressure in the exposed region, but there is no evident pressure dependence seen in the completely shadowed region. Without ion bombardment, the average deposition rate increases with pressure for C_4F_8/90%Ar and decreases for

pure C_4F_8. This may be due to the strong time dependence of FC film growth underneath the roof, which will be discussed in the following section.

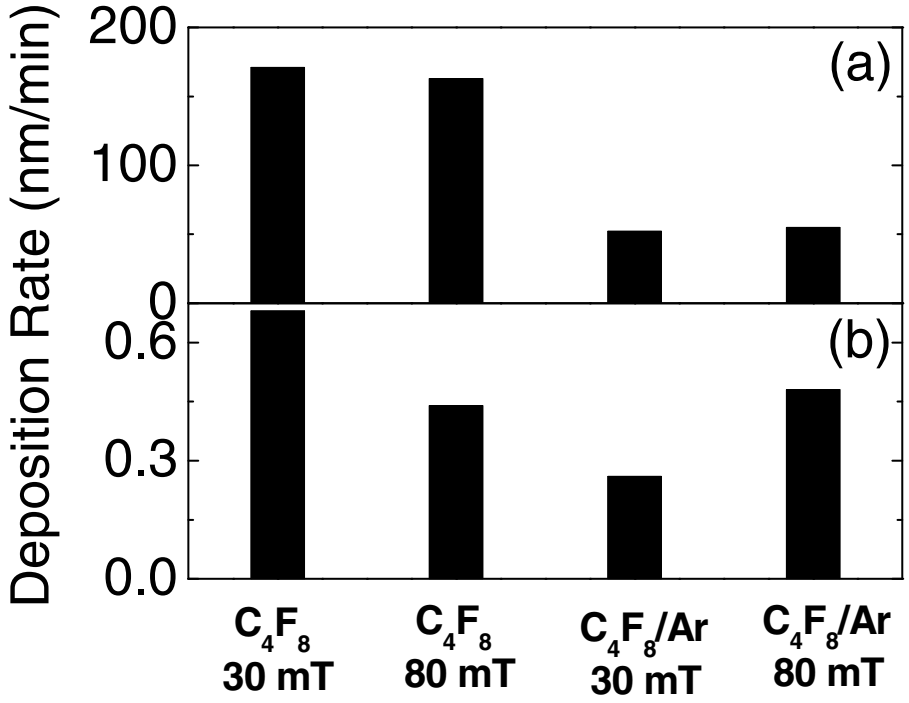

Fig. 6.4: Deposition rates of FC film both (a) in the exposed region and (b) completely shadowed region for C_4F_8 and C_4F_8/90%Ar at both 30 and 80 mTorr pressure. The other experimental parameters were: 200 W capacitive power, 40 sccm gas flow, without bias (All the experimental parameters in the following figures are same unless otherwise indicated.).

6.3.3. Time Dependent FC Film Growth

The time-averaged FC deposition rates shown in Figure 6.4 were measured after a 5 min deposition. In general, the FC film deposition rate is constant as a

function of time when surface is exposed to ion bombardment during film growth. For FC film growth without ion bombardment, the deposition rate varies strongly with time[6.26, 6.27]. Using the gap structure, a systematic study of FC film deposition without ion bombardment was undertaken by performing the deposition for various times, and then measuring the resulting FC film thickness.

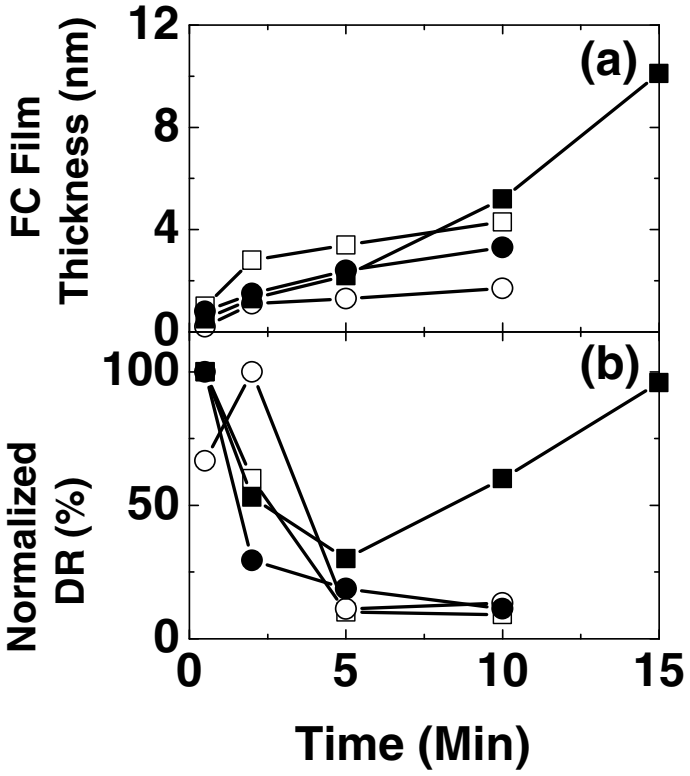

Fig. 6.5: Time dependent (a) FC film thickness and (b) Normalized FC deposition rates in the completely shadowed region for C_4F_8 ( ) and C_4F_8/90%Ar at both 30 (solid) and 80 (void) mTorr pressure.

Figure 6.5 (a) shows the variation of FC film thickness with time under the roof for pure C_4F_8 and C_4F_8/90%Ar plasmas at both 30 and 80 mTorr. The

experimental conditions were same as those in Figure 6.4 for the average deposition rates measurement. In Figure 6.5 (b) the normalized deposition rates are shown for the same experiments. Although continuous growth of FC films is observed for all conditions, the normalized deposition rates for C_4F_8/Ar plasmas show a strong initial decrease and subsequently saturates. This is consistent with the idea that continuous ion bombardment during film growth is important for high deposition rates[6.11-6.13, 6.36]. Same trend is also observed in pure C_4F_8 plasma at lower pressure. Conversely, for pure C_4F_8 at higher pressure the normalized deposition rate decreases initially and then shows a strong increase for longer experimental times. This suggests that the FC film growth shows strong substrate-dependence, which may be attributed to the different sticking coefficients of the FC precursors on bare Si and on FC film[6.26]. Therefore, for the FC film growth without ion bombardment, the real-time deposition rate is more important than the average FC deposition rate.

6.3.4. XPS Analysis of FC Films

To understand the dissociation mechanism of the C_4F_8 molecule in the capacitively coupled plasma, the deposited FC films were examined by XPS. Before we discuss FC films deposited underneath the gap structure, we first report the FC films deposited in the exposed areas. Figure 6.6 compares XPS spectra of FC layers for C_4F_8 and C_4F_8/90%Ar deposited in the exposed regions at 30 and 80 mTorr, respectively. The C (1s) spectra obtained in these conditions are similar to the spectra of the conventional FC films deposited directly by plasma process[6.30]. Four peaks (in order of increasing binding energy), assigned as C-CF_x (x=1,2,3), C-F, C-F_2, and C-

F_3, can be clearly identified. At both pressures, the bond intensities of all four peaks are comparable for pure C_4F_8. When Ar is added, there is a strong increase of C-F_2 intensity compared with the other three peaks, resulting in the increase of the F/C ratio. This is more evident at higher pressure. It is different from the observation of that in the ICP system reported in an earlier article of this group[6.32], in which Ar addition leads to F-loss of the deposited FC film. The power level and pressure for the current study were 200 W and 30 to 80 mTorr, while they were 600 to 1400 W and 6 to 20 mTorr in ICP, respectively. The low power level and the high pressure reduce the amount of energy that is available for each C_4F_8 molecule and increase the retention of the molecular structure of the excited gas, which may contribute to this difference.

Figure 6.7 shows the corresponding XPS spectra of films deposited in the completely shadowed region for the same conditions as in Figure 6.6. As previously introduced, there is no ion bombardment during this FC film growth. The film growth is due to the arrival of long-lived neutral species produced in the plasma. The direct result is the deposited FC film is much thinner as compared to the exposed region. For all conditions, there is a strong decrease of C-CF_x peak and a strong increase of C-F_2 bond as compared to the exposed region. This leads to a higher F/C ratio in the completely shadowed region for all conditions. On the other hand, the addition of Ar also results in the increase of the F/C ratio in the completely shadowed region although it is not as evident as in the exposed region. These differences are likely due to the shift in the electron energy distribution function as Ar is added, which promotes the dissociation of C_4F_8 molecules in the C_4F_8/Ar discharge[6.30-6.33].

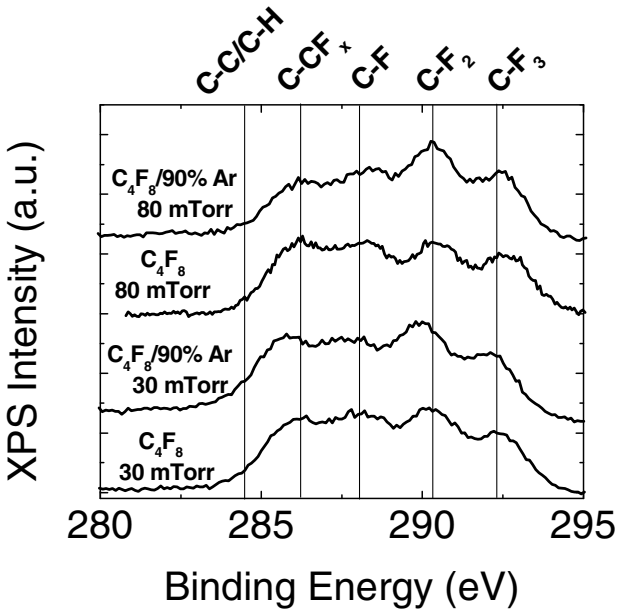

Fig. 6.6: C (1s) photoemission spectra of FC layer in the exposed region for C_4F_8 and C_4F_8/90%Ar plasmas at both 30 and 80 mTorr pressure.

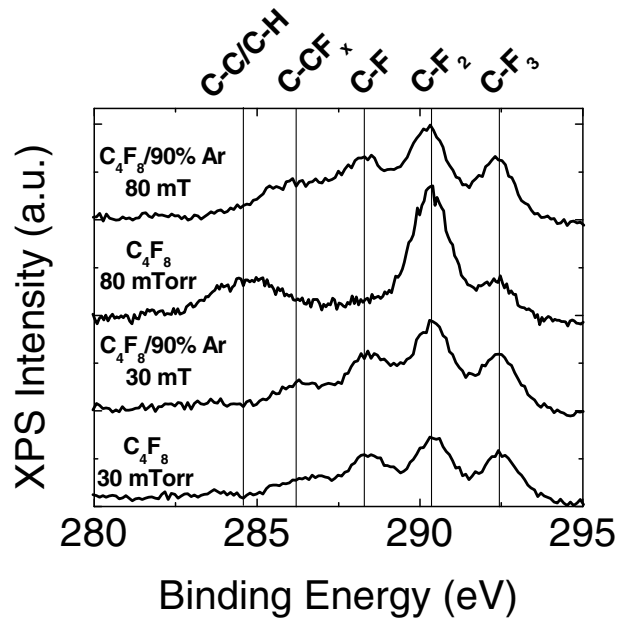

Fig. 6.7: C (1s) photoemission spectra of FC layer in the completely shadowed region for C_4F_8 and C_4F_8/90%Ar plasmas at both 30 and 80 mTorr pressure.

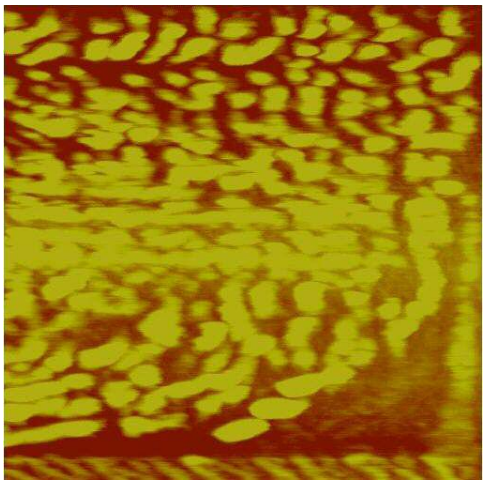

(a)

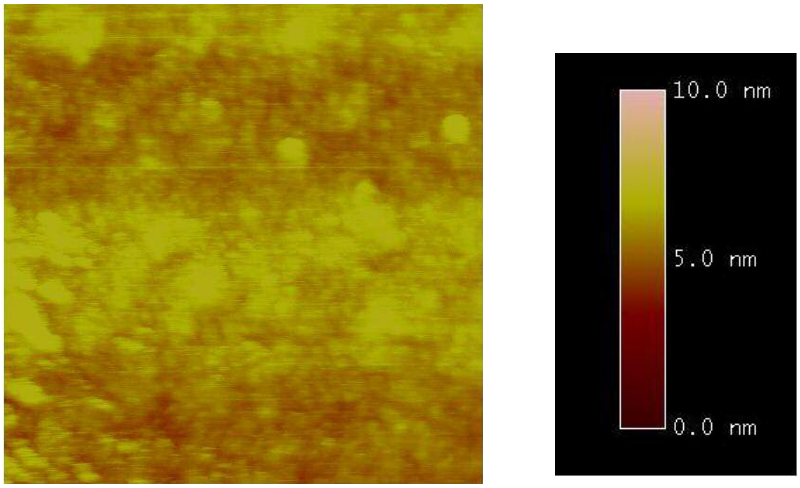

(b)

Fig. 6.8: AFM images obtained on the surface of FC film deposited in the a) completely shadowed region and b) exposed region in pure C_4F_8 plasma at 80 mTorr. The time scale used for deposition was 5 minutes.

A new peak is introduced into the C (1s) spectrum obtained underneath the gap structure for pure C_4F_8 at 80 mTorr, which can be assigned to C-C/C-H bonding.

But in this condition, there is still no evident C-CF_x bonding observed. It indicates that there are two distinct chemical portions formed on the Si substrate: One consisting primarily of C-F_2 and C-F_3 bonding, while the other consisting of C-C or C-H bonding. This is because if the C-C or C-H bonding is bonded with C-F_2 or C-F_3, then a significant amount of C-CF_x bonding must exist. This is not observed in the XPS spectrum. So the C-C/C-H bonding and C-F_x (x=2, 3) bonding must exist in the different regions. The existence of an unusual morphology compared to typical FC films is supported by the AFM measurement obtained for the same specimen surface on which XPS spectrum has been taken. It is shown in Figure 6.8 (a). The scan area is 1×1 μm. It indicates that the surface of the film is heterogeneous and two distinct regions do exist simultaneously. In contrast, most plasma polymerized FC films are smooth and homogenous. This is clearly seen in Figure 6.8 (b), which is the AFM image of the FC film deposited in the exposed region using the same experimental conditions. This difference in surface topography may shed light on FC film growth mechanism. In the following sections, we will focus on the investigation of the properties of the FC film deposited in this condition.

6.3.5. Different Effects during FC Film Growth

All the previous discussed results have been obtained from experiments in the capacitively coupled plasma. We also did the similar studies in an inductively coupled plasma as a comparison. It is well known that inductively coupled plasmas are commonly applied high-density plasmas, which are usually operated at high power and low pressure. The inductively coupled plasma system in our lab has been

well characterized and described in the previous papers in this group[6.28]. The pressure used for the previous studies ranged from 6 to 20 mTorr and the applied power was from 600 to 1400 W. In this condition, even in pure C_4F_8, the dominant fluorocarbon species in the gas phase is CF_2 and the FC film deposited is conventional: C-CF_x, C-F, C-F_2, and C-F_3 can be clearly identified and no C-C/C-H bonding is observed. This may be due to the much higher energy available for each C_4F_8 molecule. Therefore, for the current study of FC film deposition underneath the roof, a much higher pressure (150 mTorr) and/or a lower power (300 W) were applied. All the following experiments were studied in the capacitively coupled plasma reactor unless otherwise indicated.

6.3.5.1. Effect of FC Film Thickness (Effect of Interface)

Time dependent FC film growth measured by ellipsometer indicated the deposition rate underneath the gap structure shows a strong time dependence. This may be due to the interface effect. But the ellipsometer measurement couldn't accurately point to how the films properties change with time because the FC film is so thin that the refractive index is difficult to be accurately determined. To study this, the FC films deposited for different time scales were analyzed byXPS.

Figure 6.9 shows the XPS spectra of FC films deposited in 1, 5 and 15 minutes for pure C_4F_8 plasma at 80 mTorr. The corresponding thickness, which are marked in Figure 6.9, are 0.8, 2.2, 10.1 nm, respectively. The signatures of FC films show strong dependence on the FC film thickness. The C-C or C-H bonding only exists in a certain range of film thickness. It is absent for very thin FC film, and is no

longer observed in thick FC film thickness. Since the C-C or C-H bonding is much weaker for the FC film deposited at 1 minute than that deposited at 5 minutes, it cannot come from the substrate and therefore, must come from the gas phase. This can be attributed to the low power and high pressure in pure C_4F_8, which leads to the less energy available for each C_4F_8 molecule. When the deposited FC film becomes thick enough, i.e. at 10.1 nm, the C-C/C-H bonding disappears. It may indicate that the interface plays a very important role for FC film growth, and that the plasma-surface interactions and the FC film deposition mechanism change with film thickness.

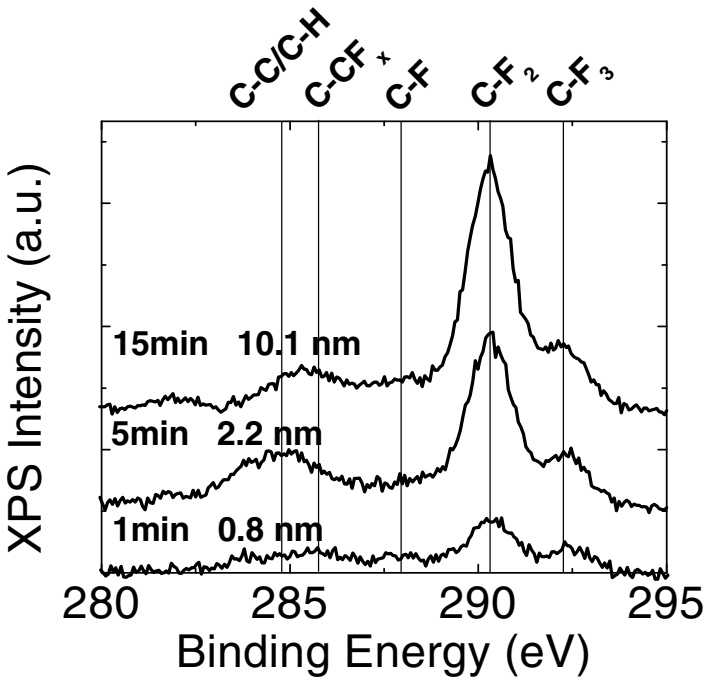

Fig. 6.9: Time dependent (1, 5 and 15 minutes deposition) C (1s) photoemission spectra of FC layer in the completely shadowed region in pure C_4F_8 plasma at 80 mTorr.

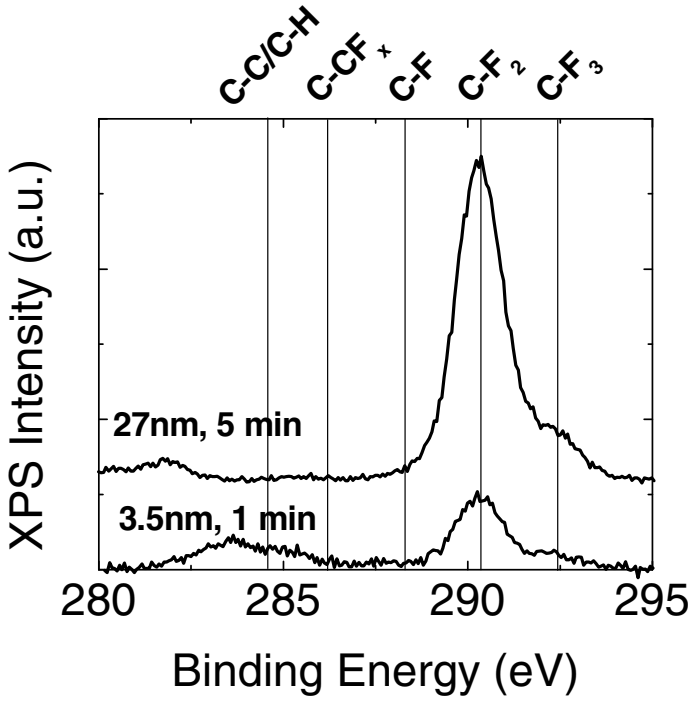

Fig. 6.10: Time dependent (1 and 5 minutes deposition) C (1s) photoemission spectra of FC layer in the completely shadowed region in pure C_4F_8. The other experimental parameters were: 1000 W inductive power, 50 sccm gas flow, 150 mTorr, without bias.

A corresponding study was made in the inductively coupled plasma. The power level used for this study was 1000 W. Since the deposition rate was higher in ICP, the time scales were reduced to 1 and 5 minutes. The measured C (1s) spectra are shown in Figure 6.10 and the corresponding film thickness are labeled on the graph. The deposited FC film thickness is 3.5 nm in the first minute, close to the FC deposited in the first 5 minutes (2.2 nm) in the capacitively coupled plasma. At this thickness, the XPS spectra look quite similar, i.e. C-F_2 bonding is dominant in the spectra and a clear C-C/C-H bonding can be observed. When the time scale for

deposition is increased to 5 minutes, the thickness of FC film also increases to 27 nm. The XPS spectra showed that C-F_2 bonding dominates the spectra. Besides the C-F_2 peak, there is a much weaker C-F_3 peak and no C-C/C-H, C-CF_x or C-F bonding is present. This observation is also similar to the C (1s) spectrum measured at 15 minutes in the capacitively coupled plasma although there is still a small C-CF_x peak distinguishable. At the same time, the thickness of the deposited FC film should be noticed: the average deposition rate at 5 minutes is much higher than that in the first minute. It supports a higher FC deposition rate on the FC film than that on the bare Si substrate and suggests that the FC growth mechanism may change with the interface. Overall, the observations in the inductively coupled plasma are consistent with the observations seen in the capacitively coupled plasma.

6.3.5.2. Effect of Ar Addition

XPS measurement in the previous section showed that in the C_4F_8/90%Ar plasma, the FC deposited film showed little C-C/C-H bonding. A possible interpretation can be provided by the surface activation model, which has been discussed by many people[5.15, 5.37-5.38]. Generally, the radicals can only adsorb at sites that have been activated or "damaged". The active sites can be produced by either ion bombardment, or by the attack of photons or metastables. Figure 6.11 shows the schematics of the active site formation with and without ion bombardment. In the exposed region, the dominant mechanism of active site formation is the ion bombardment and the effects of photons and metastables are negligible. Usually, the ion bombardment is uniform and continuous in the plasma. Therefore, the active site

is dense and uniform on the substrate and it will not limit the growth of the FC film. While in the completely shadowed region shown in Figure 6.11 (b), the ion bombardment is absent. The dominant mechanism of active site formation is the attack of the photons and/or metastables. Thus, the distribution of the active site is strongly dependent on the density of the available photons and/or metastables. In pure C_4F_8, few available metastables leads to the discontinuous formation of the active site and thus discontinuous growth of the FC film. When a significant amount of Ar is added, the long-live Ar^* can provide energy for the active site generation, which leads to the continuous formation of the FC film.

For better understanding how the Ar addition affects the FC film growth in the condition without ion bombardment, smaller amount of Ar, i.e. 20% and 40% Ar, were added to the pure C_4F_8. Figure 6.12 compares the XPS spectra of FC films got from the completely shadowed region. With 20%Ar addition, the decrease of the C-C/C-H peak can be immediately seen. When Ar is increased to 40%, no C-C/C-H peak can be recognized. At the same time, the intensity of $C-F_2$ bonding, which is the dominant bonding in all cases, decreases with the Ar addition. This can be attributed to the decrease of available FC deposition precursors. It results to the decrease of the FC film thickness, which is 2.2 nm for pure C_4F_8 and decreases to 2 and 1.3 nm with 20% and 40% Ar addition. On the other hand, $C-CF_x$ and C-F bonding, which is not clear in the pure C_4F_8 and C_4F_8/20%Ar conditions, become distinguishable. This is consistent with the expectation that Ar addition can promote the dissociation of C_4F_8 molecules.

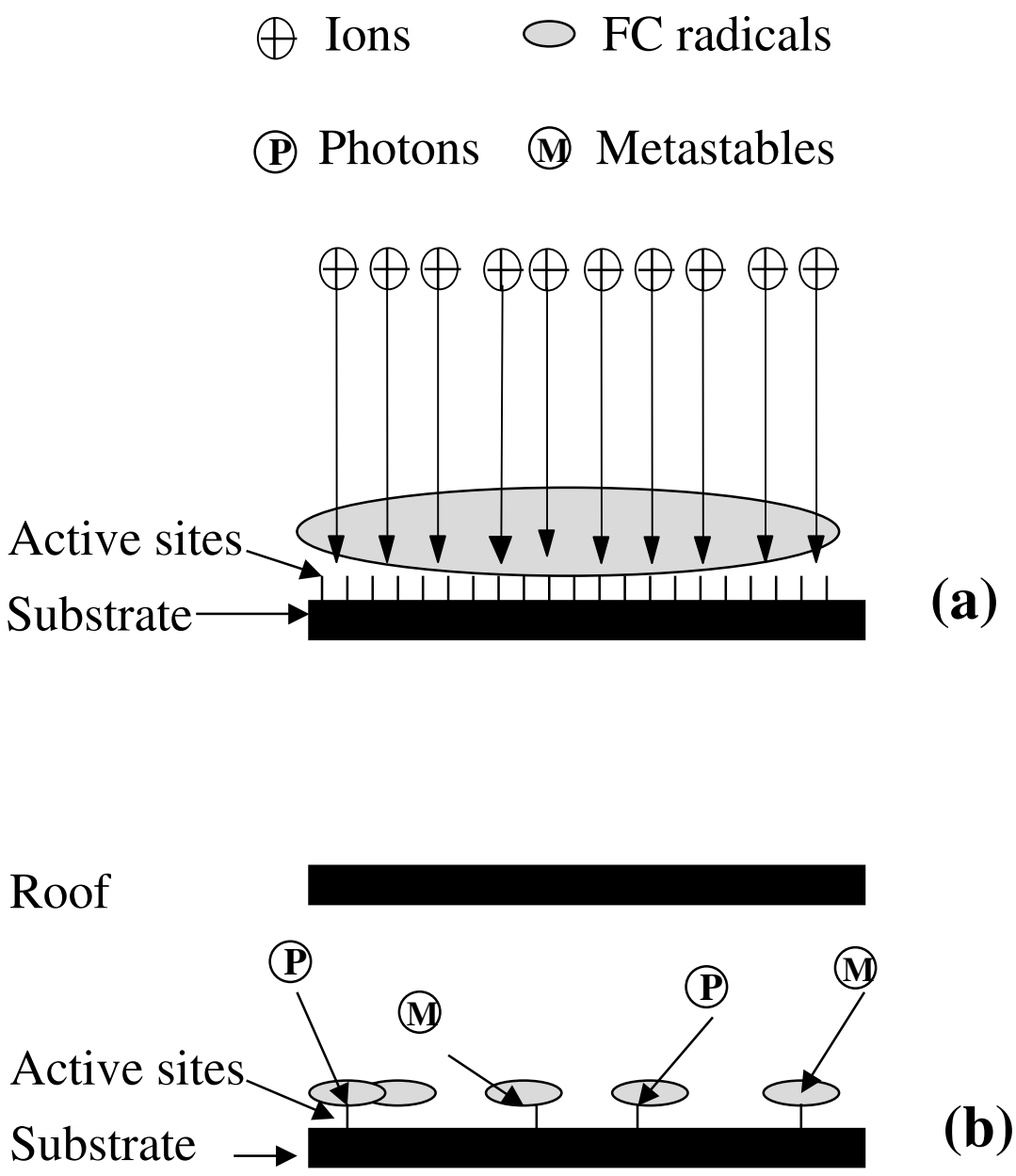

Fig. 6.11: Schematic of FC film growth (a) in the exposed region and (b) in the completely shadowed region.

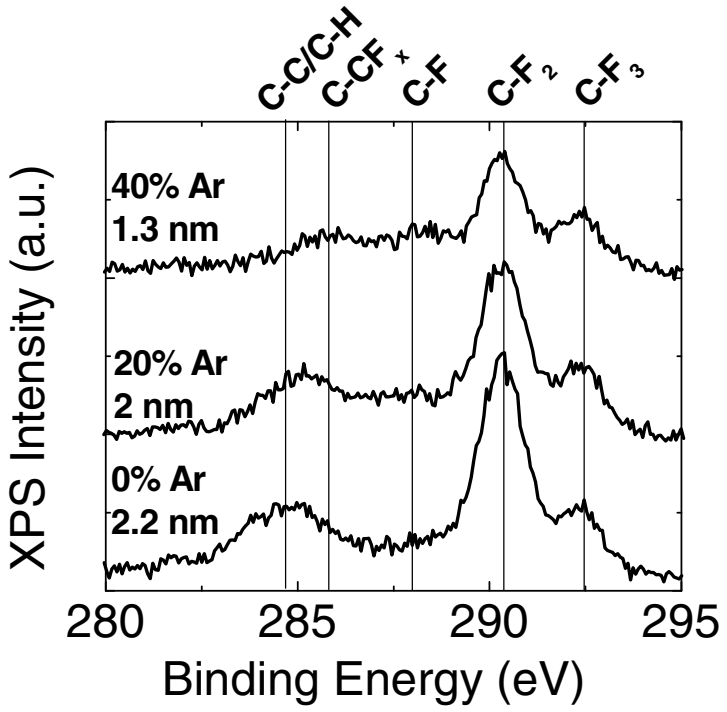

Fig. 6.12: Ar dependent C (1s) photoemission spectra of FC layer in the completely shadowed region deposited in C_4F_8/Ar plasma at 80 mTorr. The time scale used for deposition was 5 minutes.

6.3.5.3. Effect of Power

We also studied the FC film deposition underneath the gap structure at different power levels: 100, 200 and 300 W. The measured XPS spectra are compared in Figure 6.13. With the increase of source power, the thickness of FC film increases from 1.7 to 2.3 nm, which are labeled on the Figure 6.13. The intensity of the XPS spectra also shows a small increase. The XPS spectra measured at 100 W and 200 W show similar characteristics: They have the highest intensity in C-F_2 bonding and also have an evident C-C/C-H bonding. When the power is increased to 300 W, the

measured XPS spectra looks quite similar to that measured with 40%Ar addition: No C-C/C-H bonding is observed, four other peaks (C-CF_x, C-F, C-F_2, and C-F_3) exist, and among which C-F_2 bonding dominates. This may be explained by the increased plasma density and thus increased photons available for the active site generation. Additionally, the increased dissociation due to the increase of power may be another reason for this difference due to the different sticking coefficient of the different FC radicals.

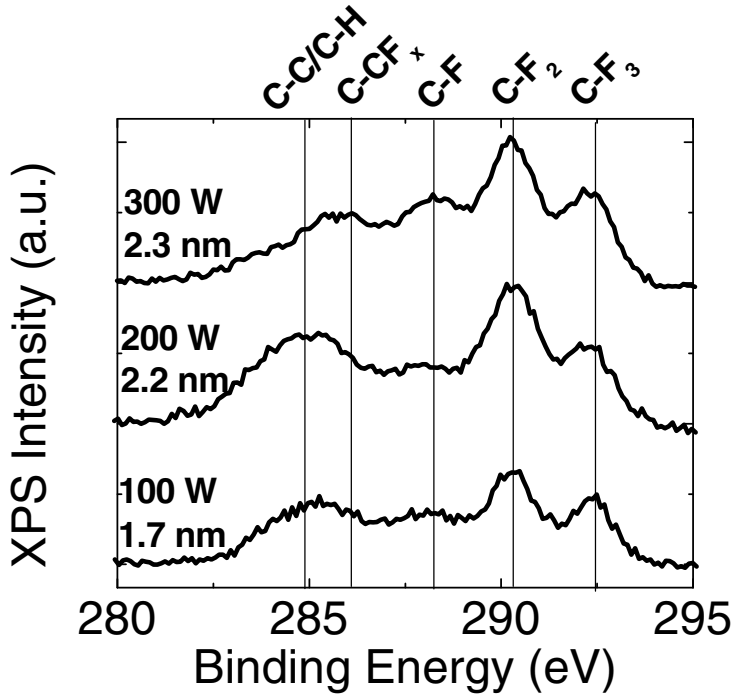

Fig. 6.13: Power dependent C (1s) photoemission spectra of FC layer in the completely shadowed region in pure C_4F_8 at 80 mTorr. The time scale used for deposition was 5 minutes.

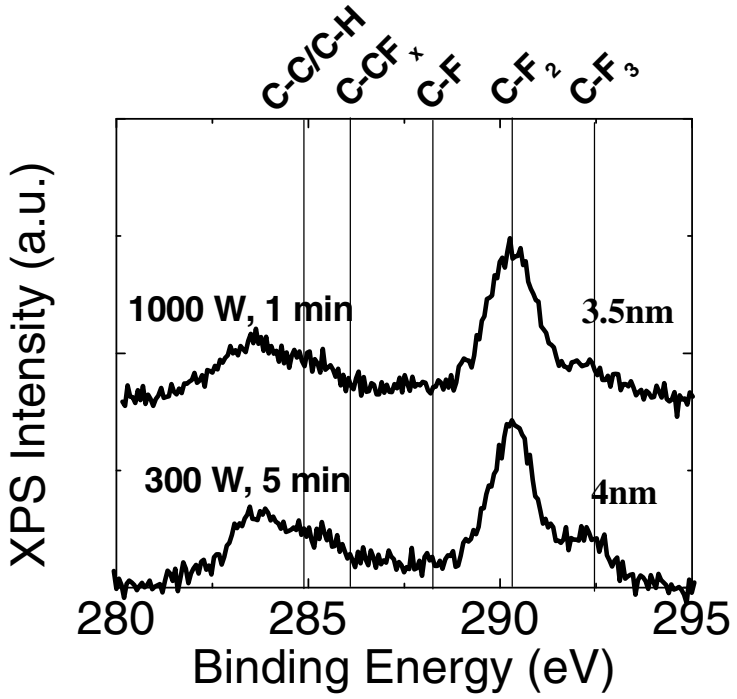

Fig. 6.14: Power dependent C (1s) photoemission spectra of FC layer in the completely shadowed region in pure C_4F_8. The other experimental parameters were: inductive power, 50 sccm gas flow, 150 mTorr, without bias.

As in the capacitively coupled plasma, the effect of power was also studied in the inductively coupled plasma. Since the time dependent studies showed that the C-C/C-H bonding only exists for a certain FC film thickness, the FC film for this study is limited to be about 4 nm so that the time scales used for different power levels are different. Figure 6.14 shows the XPS spectra of the FC films deposited in the inductively coupled plasma. The applied source powers were 300 and 1000 W, respectively. For the higher power level, the deposition time is 1 minute and the FC film thickness is 3.5 nm; while for the lower power, the corresponding time and thickness are 5 minutes and 4 nm, respectively. Both spectra have the same

characteristics as those obtained in the capacitively coupled plasma: a dominant C-F_2 bonding and a significant C-C/C-H bonding. The difference between the XPS spectra of the FC film deposited at different power levels is that the intensity of the C-C/C-H and C-F_3 bonding decreases with the increase of power. Compared with the experiments in CCP, the power level used for experiments in ICP is quite high. But it's not a surprise because of the different sizes of the electrodes and chamber: The diameter of the electrode used in ICP chamber is 300 mm and the diameter of the electrode used in the CCP reactor is 125 mm. The much bigger size of the chamber leads to a lower power density in the inductively coupled plasma, even at 1000 W source power, compared to the capacitively coupled plasma at 200 W source power.

6.3.6. FC Film Growth in Different Height Gap Structure

Previous studies showed that using gap structure approach in both capacitively and inductively coupled plasmas, a C-F_2 dominant FC film could be deposited. It results in a higher F/C ratio than the FC film deposited in the exposed region. With an increase of time, C-C/C-H bonding became weaker and weaker, and eventually vanishing. This causes a further increase of the F/C ratio. As is well known, the increase of the F/C ratio in the coated FC film remarkably improves hydrophobicity, i.e, can be made effectively waterproof. Unfortunately, the previously discussed studies were based on a very thin gap structure, i.e. the roof height is 0.65 mm, and the FC film deposition rate is too low to be applicable. Thus, finding a way to deposit the thicker FC film underneath the gap structure is necessary.

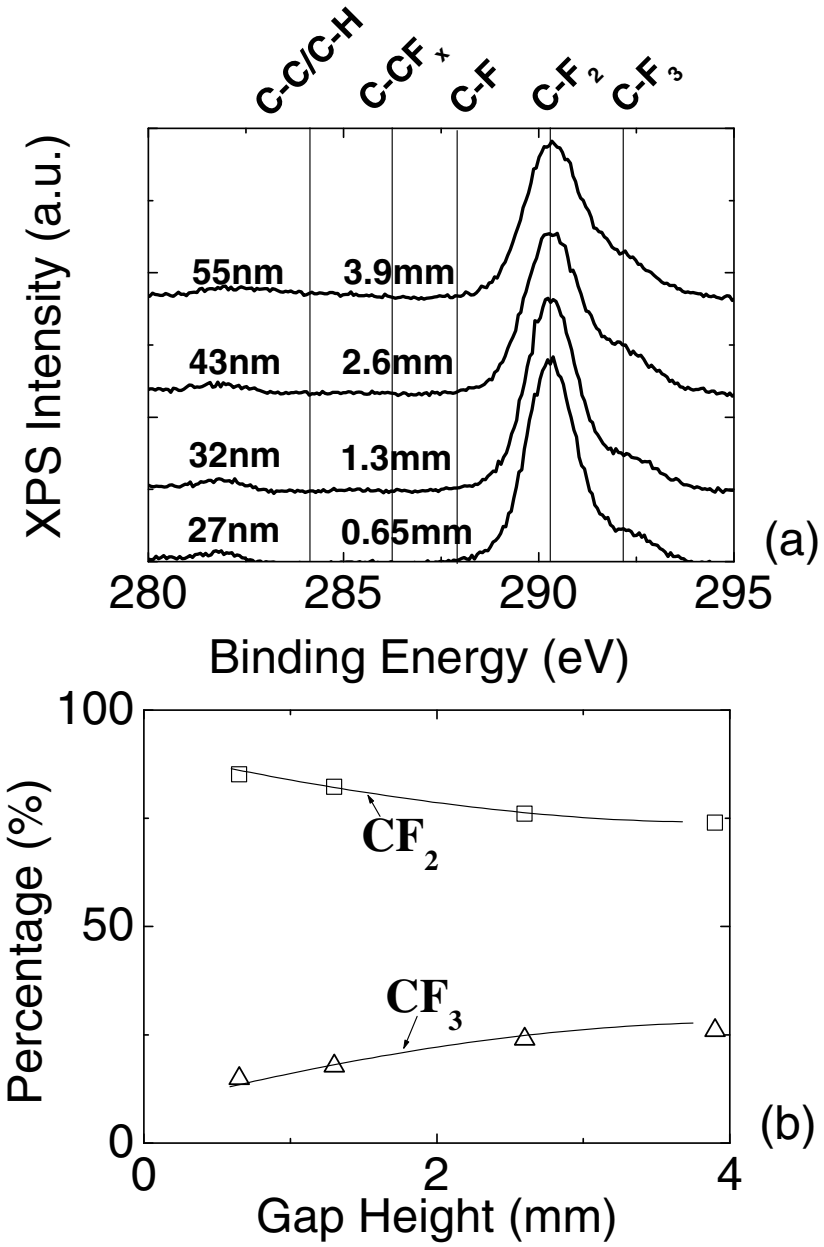

Fig. 6.15: (a) C (1s) photoemission spectra and (b) corresponding change of C-F_2 and C-F_3 bonding of FC layer deposited in the completely shadowed region using different height gap structures in pure C_4F_8. The other experimental parameters were: 1000 W inductive power, 50 sccm gas flow, 150 mTorr, without bias, 5 minutes deposition.

Increasing the height of the gap structure is straightforward because more neutral species will be able to diffuse onto the substrate. When the gap height is higher than 5 mm, glow discharge can be observed in the region underneath the roof. In that case, the FC film growth is no longer without ion bombardment. Therefore, the gap height was restricted to be no greater than 5 mm. Figure 6.15 (a) shows the XPS spectra of the FC films deposited under the different height gap structure in ICP. The time used for the film growth was fixed at 5 minutes. The gap heights used for the study were 0.65, 1.3, 2.6, and 3.9 mm. The corresponding FC film thicknesses are 27, 32, 43, and 55 nm, respectively. Both gap height and the deposited FC film thickness are marked on the figure. Since the deposited FC film is thick, no C-C/C-H bonding is observed for all conditions. As expected, with the increase of gap height, the deposited FC film thickness also increases, which is the direct result of increased CF_x radicals able to reach the substrate. For all conditions, the dominant bonding in the FC films, are C-F_2 and C-F_3. Other peaks are very weak and indistinguishable. At the same time, the peak at the C (1s) spectrum becomes broader with the increase of the gap height, which is the result of increased intensity of C-F_3 bonding relative to that of C-F_2 bonding. This can be clearly seen in Figure 6.15 (b). It compares the relative change of C-F_2 and C-F_3 intensities with the gap height, which was computed from the simulation of the XPS spectra. This indicates that a higher gap may not only increase the growth rate of FC film, but also increase the F/C ratio of the FC film and further improve the hydrophobicity of the FC coating. This was supported by water contact angle measurements performed by a goniometer. The measurements indicated that the film deposited in the exposed region had a degree contact angle of 95 degrees,

while the film deposited using 0.65 mm and 3.9 mm gap had contact angles of 115 and 165 degrees, respectively.

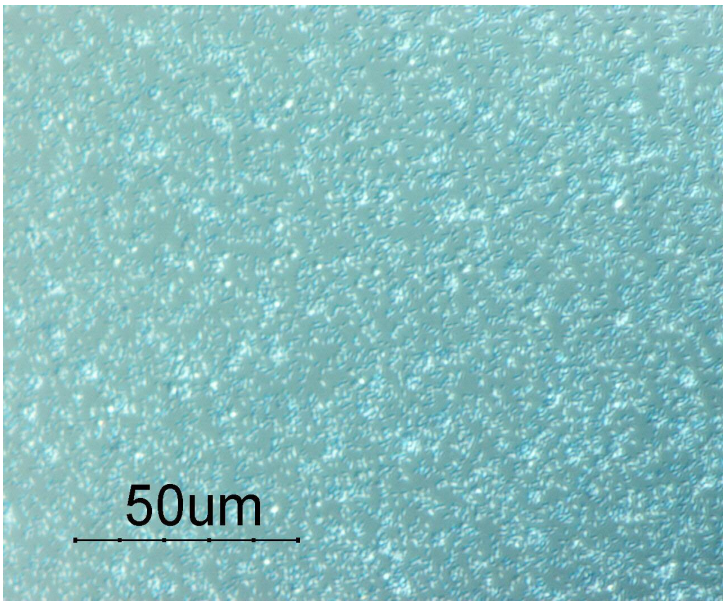

Fig. 6.16: Optical microscopic images obtained on the surface of FC film deposited in the completely shadowed region in pure C_4F_8 plasma. The experimental parameters were same as in Fig. 6.15.

The surface image of the FC film deposited using 3.9 mm gap is shown in Figure 6.15, which was measured by an optical microscope. The surface of the FC film is pretty rough, similar to the observation in Figure 6.8 by AFM. We should notice that the scan area is about 150×150 μm, which is much larger than the scan area by AFM. The roughness of the surface may also contribute to the hydrophobicity of the deposited FC film. This may limit the application for this coating. How to improve this still needs to be studied further.

6.4. CONCLUSION

A gap structure was designed to investigate the influence of ion bombardment on the composition of deposited FC films. The deposition rate, composition and bonding of deposited FC films are determined as a function of processing conditions using ellipsometry and X-ray photoemission spectroscopy in both an inductively and capacitively coupled plasmas. The deposition rate and surface chemistry of FC films deposited in the completely shadowed region depend strongly on discharge chemistry and are significantly different from that of films deposited in the exposed region. A novel feature with two distinct regions existing simultaneously is seen, one consisting primarily C-F_2 and C-F_3 bonding and the other of C-C or C-H bonding, which is produced in pure C_4F_8 at 80 mTorr. This is the result of the low power and high pressure applied, which reduces the amount of energy available per C_4F_8 molecule and increases the retention of the molecular structure of the excited gas. The significant nanoscale topography is also supported by AFM measurement. The subsequent water contact angle measurements indicate that an excellent hydrophobicity of the FC film due to the high F/C ratio of the coating. The existence of two distinct chemical surface portions can be eliminated by either adding Ar or increasing the source power, both of which can increase the energy available for each C_4F_8 molecule.

ACKNOWLEDGMENTS

Financial support of this work by Lam Research Corporation and by Maryland Technology-Development Corporation (TEDCO) is gratefully acknowledged. We

also thank Mr. Bryan Orf for helpful discussions and assistance with water contact angle measurements.

Chapter 7: Overall Conclusions

The thesis summarizes results obtained during studies of plasma processing of advanced electronic materials using both inductively and capacitively coupled plasma reactors. Based on the experimental measurements our understanding of basic etching mechanism of dielectric materials was improved.

Using an inductively coupled plasma system, we studied the effect of CO addition to C_4F_8/Ar discharges to enable selective etching of OSG over etch stop layers. In addition, we investigated the origin of the surface roughness for an advanced 193 nm photoresist material. The conclusions that can be drawn from that part of the work presented are:

- CO addition to C_4F_8 decreases the etch rates, but the etching selectivity of OSG relative to Si_3N_4 or SiC etch stop layers remains nearly constant. This is explained by the high stability of the CO molecule as compared to C_4F_8, which minimizes the dissociation of CO. For CO addition to Ar rich C_4F_8/Ar gas mixtures, the dissociation of CO is strongly increased. It leads to loss of the OSG/SiC etching selectivity. The relative magnitudes of the energy thresholds of electron induced dissociation and ionization in the C_4F_8/CO and C_4F_8/Ar/CO gas mixtures were used to explain these observations.

- The dry etching characteristics of a 193 nm and a 248 nm photoresist material were investigated using inductively coupled plasmas fed with Ar, C_4F_8, C_4F_8/Ar and O_2. The plasma durability of the 248 nm photoresist was better than that of 193 nm photoresist material, both in terms of etching resistance and surface smoothness. Our results indicate that the origin of the surface roughness for the 193

nm photoresist can be attributed to the removal of carbonyl groups and simultaneous fluorine penetration during the etching process.

A small gap structure was designed to simulate sidewall surface processes occurring during high aspect ratio trench etching and to study surface chemistry aspects of fluorocarbon film deposition with and without ion bombardment. This structure was used to investigate these processes in capacitively coupled fluorocarbon plasmas. Our work lead to the following conclusions:

- Both C_4F_8/Ar and CF_4/H_2 based gas chemistries were used for the pattern transfer, and we studied time-dependent deposition rates, surface chemistry using the gap structure, and actual structure etching and profile evolution for organosilicate glass. From a comparison of the data obtained using the gap structure and SEM analysis of the etched features, we show that the feature sidewall angles qualitatively correlates with the deposition rates measured for completely shadowed surfaces of the gap structure: The lower the FC deposition rate on the sidewall, the more vertical the trench sidewall. This approach also allowed us to investigate the effect of O_2 and N_2 addition to C_4F_8/Ar on surface chemistry and profile shape.

- For the gap structure, the deposition rate and surface chemistry of FC films strongly depend on the substrate location and discharge chemistry. A novel feature that has been observed here for the first time are two distinct regions on the substrate surface. One of these exhibits primarily C-F_2 and C-F_3 bonding whereas the other is characterized by C-C or C-H bonding. These phenomena are characteristic of pure C_4F_8 discharges produced in a capacitively coupled plasma system at 80 mTorr. Atomic force microsocpy data show corresponding nanoscale structure for the films

deposited under these conditions. The existence of the nanoscale topography can be eliminated by adding Ar, and/or increasing the source power.

List of Reference

Chapter 1:

[1.1] B. Chapman, *Glow discharge Process*, (John Wiley& Sons, Inc., New York, 1980).

[1.2] M.A. Lieberman and A.J. Lichtenberg, *Principles of Plasma Discharges Materials Processing*, (John Wiley & Sons, Inc., New York, 1994).

[1.3] A. Grill, *Cold Plasma Materials Fabrication: From Fundamentals to Applications*, (Wiley-IEEE Press, New York, 1994).

[1.4] D. M. Manos and D. L. Flamm (Eds), *Plasma Etching*, (Academic, San Diego, 1988)

[1.5] R. J. Shul and S. J. Pearton (Eds.) *Handbook of Advanced Plasma Processing Techniques*, (Springer, 2000).

[1.6]R. d'Agostino, F. Cramarossa, F. Fracassi, and F. Illuzzi, *Plasma Deposition, Treatment and Etching of Polymers*, (Academic, San Diego, 1990).

[1.7]R. d'Agostino, P. Favia and F. Fracassi, *Plasma Processing of Polymers*, (Kluwer Academic, Boston, 1997).

[1.8]S. Wolf, *Silicon Processing for the VLSI Era*, (Lattice, Sunset Beach, CA, 2004).

[1.9]J. H. Keller, J. C. Forster and M. S. Barnes, J. Vac. Sci. Technol. A **11**, 2487 (1993).

[1.10] O. A. Popov (Eds.) *High density plasma sources: design, physics, and performance*, (Noyes, Park Ridge, NJ 1996).

Chapter 2:

[2.1]S.Seta, M. Sekine, H. Hayashi, and Y. Yoshida, Jpn. J.Appl. Phys. **40,** 2501 (2001).

[2.2]H. Doh, C. Chu, K. Chi, and J. Moon, Jpn. J.Appl. Phys. **40,** 6109 (2001).

[2.3]H. Hayashi and M.Sekine, Jpn. J.Appl. Phys. **38,** 4910 (1999).

[2.4]H. Hayashi, K. Kurihara and M. Sekine, Jpn. J.Appl. Phys. **35,** 2488 (1996).

[2.5]N. Omori, H.Matsuo, S. Watanabe, and M. Puschmann, Surf. Sci. **352**, 988 (1996).

[2.6]Y. Hakosaka, M. Nakamura and H. Sugai, Jpn. J.Appl. Phys. **33,** 2157 (1994).

[2.7]T. Akimoto, S. Furuoya, K. Harasima, and E. Ikawa, Jpn. J.Appl. Phys. **33**, 2151 (1994).

[2.8]X. Hua, X. Wang, D. Fuentevilla, G. S. Oehrlein, F. G. Celii, and K. H. R. Kirmse, J. Vac. Sci. Technol. A. **21**, 1708 (2003).

[2.9]Y. Wang and J. K. Olthoff, J. Appl. Phys. **85**, 6358 (1999).

[2.10]Y. Wang R. J. Van Brunt and J. K. Olthoff, J. Appl. Phys. **83**, 703 (1998).

[2.11]M. Schaepkens, T. E. F. M. Standaert, N. R. Rueger, P. G. M. Sebel, G. S. Oehrlein, and J. M. Cook, J. Vac. Sci. Technol. A. **17**, 26 (1999).

[2.12]X. Li, L. Ling, X. Hua, M. Fukusawa, and G. S. Oehrlein, J. Vac. Sci. Technol. A. **21**, 284 (2003).

[2.13]X. Li, X. Hua, L. Ling, G. S. Oehrlein, M. Barela, and H. M. Anderson, J. Vac. Sci. Technol. A. **20**, 2052 (2002).

[2.14]M. Matsui, F. Uchida, M. Kojima, T. Tokunaga, F. Yano, and M. Hasegawa, J. Vac. Sci. Technol. A. **20**, 117 (2002).

[2.15]T. E. F. M. Standaert, M. Schaepkens, N. R. Rueger, P. G. M. Sebel, G. S. Oehrlein, and J. M. Cook, J. Vac. Sci. Technol. A. **16**, 239 (1998).

[2.16]*CRC handbook of chemistry and physics, 82nd Ed.,* CRC Press, Cleveland (2001-2002)

[2.17]G. I. Font, W. L. Morgan and G. Mennenga, J. Appl. Phys. **91**, 3530 (2002).

[2.18]W. Liu and G. A. Victor, The Astrophysics Journal, **435**, 909, (1994)

[2.19]V. A. Godyak, R. B. Piejak and B. M. Alexandrovich, Plasma Sources Sci. T. **11**, 397 (2002).

Chapter 3:

[3.1]H. Ito, IBM J. Res. Dev. **45,** 683 (2001).

[3.2]T. Kajita, Y. Nishimura, M. Yamamoto, H. Ishii, A. Soyano, A. Kataoka, M. Slezak, M. Shimizu, P. Varanasi, G. Jordhamo, M. Lawson, R. Chen, W. Brunsvold, W. Li, R. Allen, H. Ito, H. Truong, and T. Wallow, Proc. SPIE **4345,** 712 (2001).

[3.3]H. Ito, IBM J. Res. Dev. **41,** 69 (1997).

[3.4]E. Reichmanis, O. Nalamasu, F.M. Houlihan, T.I. Wallow, A.G. Timko, R. Cirelli, G. Dabbagh, R.S. Hutton, A.E. Novembre, and B.W. Smith, J. Vac. Sci. Technol. B **15,** 2528 (1997).

[3.5]W. Zhao, T. Ohfuji, M. Sasago, and S. Tagawa, Proc. SPIE, **3333**, 53 (1998).

[3.6]T. Kudo, E. Alemy, R. Dammel, W. Kim, T. Kudo, S. Lee, S. Masuda, D. McKenzie, M. Rahman, A. Romano, M. Padmanaban, J. Chun, J. Jun, S. Lee, K. Shin, and H. Kim, J. Photopolym. Sci. Technol. **15**, 549 (2002).

[3.7]M. Padmanaban, E. Alemy, R. Dammel, W. Kim, T. Kudo, S. Lee, D. Rahman, W. Chen, R. Sadjadi, W. Livesay, and M. Ross, J. Photopolym. Sci. Technol. **15**, 521 (2002).

[3.8]T. Kudo, J. Bae, R. Dammel, W. Kim, D. McKenzie, M. Rahman, and M. Padmanaban, Proc. SPIE, **4345**, 179 (2001).

[3.9]T. Kajita, Y. Yamamoto, H. Ishii, A. Soyano, A. Kataoka, M. Slezak, M. Shimizu, P. Varanasi, G. Jordahamo, M. Lawson, R. Chen, W. Brunsvold, W. Li, R. Allen, H. Ito, H. Truong, and T. Wallow, Proc. SPIE, **4345**, 712 (2001).

[3.10]Y. Hu, W. He, K. Gonsalves, and L. Merhari, Proc. SPIE, **4345**, 881 (2001).

[3.11]T. Ohfuji, M. Endo, M. Takahashi, T. Naito, T. Tatsumi, K. Kuhara, and M. Sasago, Proc. SPIE, **3333**, 595 (1998).

[3.12]T. Wallow, P. Brock, R. Pietro, R. Allen, J. Opitz, R. Sooriyakumaran, D. Hofer, J. Meute, J. Byers, G. Rich, M. McCallum, S. Schuetze, S. Jayaraman, K. Hullihen, R. Vicari, L. Rhodes, B. Goodall, and R. Shick, Proc. SPIE, **3333**, 92 (1998).

[3.13]E. A. Hudson, Z. Dai, Z. Li, S. Kang, S. Lee, W. Chen, and R. Sadjadi , Proc. Of International Symposium on Dry Process, Tokyo, Institute of Electrical Engineers of Japan, 253 (2003).

[3.14]M. Schaepkens, T. E. F. M. Standaert, N. R. Rueger, P. G. M. Sebel, G. S. Oehrlein, and J. M. Cook, J. Vac. Sci. Technol. A. **17**, 26 (1999).

[3.15]J.C. Vickerman, in *ToF-SIMS Surface Analysis by Mass Spectrometry*, J.C. Vickerman and D. Briggs (eds.), IM Publication and Surface Spectra Lim, 2001.

[3.16]X. Li, L. Ling, X. Hua, M. Fukasawa, G. S. Oehrlein, M. Barela, and H. M. Anderson, J. Vac. Sci. Technol. A. **21**, 284 (2003).

[3.17]Xi Li, X. Hua, L. Ling, G. S. Oehrlein, M. Barela, and H. M. Anderson, J. Vac. Sci. Technol. A. **20**, 2052 (2002).

[3.18]H. Gokan, S. Esho and Y. Ohnishi, J. Electrochem. Soc. **130**, 143 (1983).

[3.19]H. Gokan, Y. Ohnishi and K. Saigo, Microelectronic Engineering, **1**, 251, (1983).

[3.20]F. L. McCrackin, NBS Tech. Note 479, 1969 (National Bureau of Standards, U. S. Department of Commerce, Washington, DC).

[3.21]R. Kwong, W. Moreau and W. Yan, Proc. SPIE, **3678**, 1209 (1999).

[3.22]T. Sarubbi, M. Ross, M. Neisser, T. Kocab, B. Beauchemin, W. Livesay, S. Wong, and W. Ng, Proc. SPIE **4345**, 21 (2001).

[3.23]M. S. Kim, J. W. Park, H. J. Kim, B. J. Jun, M. G. Gil, B. H. Kim, M. Ross, and W. Livesay, Proc. SPIE **4345**, 737 (2001).

[3.24]T. E. F. M. Standaert, P. J. Matsuo, X. Li, G. S. Oehrlein, T. M. Lu, R. Gutmann, C. T. Rosenmayer, J. W. Bartz, J. G. Langan, and W. R. Entley, J. Vac. Sci. Technol. A, **19**, 435 (2001).

[3.25]R. Dammel, Semiconductor International, **26** (13), 2003.

Chapter 4:

[4.1]P. Jiang, F. G. Celii, W. W. Dostalik, K. J. Newton, and H. Sakima, J. Vac. Sci. Technol. A **19**, 1388 (2001).

[4.2]H. L. Maynard, C. S. Pai, C. B. Case, R. O. Adebanjo, M. R. Baker, W. W. Tai, and R. Liu , IEEE IITC Proc. 212, (1999).

[4.3]S. Vanhaelemeersch, C. Alaerts, M. Baklanov, and H. Struyf, IEEE IITC Proc. 97, (1999).

[4.4]G. S. Oehrlein and H. L. Williams, J. Appl. Phys. **62**, 662 (1987).

[4.5]O. Joubert, G. S. Oehrlein and Y. Zhang, J. Vac. Sci. Technol. A **12**, 658 (1994).

[4.6]K. Takahashi, M. Hori, S. Kishimoto, and T. Goto, Jpn. J. Appl. Phys. **33**, 4181 (1994).

[4.7]A. Sankaran and M. J. Kushner, J. Appl. Phys. **97**, No. 023307 (2005).

[4.8]A. Sankaran and M. J. Kushner, J. Vac. Sci. Technol. A **22**, 1242 (2004).

[4.9]A. Sankaran and M. J. Kushner, J. Vac. Sci. Technol. A **22**, 1260 (2004).

[4.10]A. Sankaran and M. J. Kushner, App. Phys. Lett. **82**, 1824 (2003).

[4.11]D. Zhang and M. J. Kushner, J. Vac. Sci. Technol. A **18**, 2661 (2000).

[4.12]D. Zhang and M. J. Kushner, J. Vac. Sci. Technol. A **19**, 524 (2001).

[4.13]J. P. Booth, G. Cunge and P. Chabert, J. Appl. Phys. **85**, 3097 (1999).

[4.14]R. d'Agostino, F. Cramarossa, F. Fracassi, and F. Illuzzi, *Plasma Deposition, Treatment and Etching of Polymers*, (Academic, San Diego, 1990).

[4.15]M. Schaepkens, G. S. Oehrlein and J. M. Cook, J. Vac. Sci. Technol. B **18**, 848 (2000).

[4.16]K. Williams, I. Martin and E. Fisher, J. Am. Soc. Mass Spectrum **13**, 518 (2002).

[4.17]I. Martin and E. Fisher, J. Vac. Sci. Technol. A **22**, 2168 (2004).

[4.18]C. Abrams and D. Graves, J. Vac. Sci. Technol. A **19**, 175 (2001).

[4.19]G. Cunge and J. P. Booth, J. Appl. Phys. **85**, 3953 (1999).

[4.20]D. Gray, V. Mohindra and H. Sawin, J. Vac. Sci. Technol. A **12**, 354 (1994).

[4.21]G. S. Oehrlein, Y. Zhang, D. Vender, and M. Haverlag, J. Vac. Sci. Technol. A **12**, 323 (1994).

[4.22]S. Agraharam, D. Hess, P. Kohl, and S. Allen, J. Vac. Sci. Technol. A **17**, 3265 (1999).

[4.23]C. B. Labelle, K. K. S. Lau, and K. K. Gleason, Mater. Res. Soc. Symp. Proc. **511**, 75 (1998).

[4.24]L Zheng, L. Ling, X. Hua, and G. S. Oehrlein, J. Vac. Sci. Technol. A **23**, 634 (2005).

[4.25]W. Tsai, G. Mueller, R. Lindquist, B. Frazier, and V. Vahedi, J. Vac. Sci. Technol. B **14**, 3276 (1994).

[4.26]O. A. Popov, High *Density Plasma Sources: Design, Physics, and Performance*, (Noyes Publications, Park Ridge, NJ, 1995).

[4.27]S. Rauf and M. J. Kushner, IEEE Trans. Plasma Sci., **27,** 1329 (1999).

[4.28]J. Jolly and J. P. Booth, J. Appl. Phys., **97**, 103305 (2005).

[4.29]K. Bera, D. Hoffman, S. Shannon, G. Delgadino, and Y. Ye, IEEE Trans. Plasma Sci., **33,** 382 (2005).

[4.30]X. Hua, X. Wang, D. Fuentevilla, G. S. Oehrlein, F. G. Celii, and K. H. R. Kirmse, J. Vac. Sci. Technol. A **21**, 1708 (2003).

[4.31]M. Schaepkens, T. E. F. M. Standaert, N. R. Rueger, P. G. M. Sebel, G. S. Oehrlein, and J. M. Cook, J. Vac. Sci. Technol. A. **17**, 26 (1999).

[4.32]Y. Furukawa, R. Wolters, H. Roosen, J.H.M. Snijders, and R. Hoofman, Microelectron. Eng. **76,** 25 (2004).

[4.33] J. Kim, H. Park and S. Hyun, Thin Solid Films **377-378**, 525 (2000).

[4.34] S. T. Chen, G. S. Chen, T. J. Yang, T. C. Chang, and W. H. Yang, Electrochemical and Solid-State Letters **6**, F4 (2003).

[4.35]O. Louveau, C. Bourlot, A. Marfoure, I. Kalinovski, J. Su, G. Hills, and D. Louis, Microelectron. Eng. **73-74**, 351 (1999).

[4.36]P. T. Liu, T. C. Chang, H. Su, Y. S. Mor, Y. L. Yang, Henry Chung, J. Hou, and S. M. Sze, J. Electrochem. Soc. **148**, F30 (2001).

[4.37]P. T. Liu, T. C. Chang, S. M. Sze, F. M. Pan, Y. J. Mei, W. F. Wu, M. S. Tsai, B. T. Dai, C. Y. Chang, F. Y. Shih, and H. D. Huang, Thin Solid Films **332**, 345 (1998).

[4.38] T. C. Chang, Y. S. Mor, P. T. Liu, T. M. Tsai, C. W. Chen, Y. J. Mei, and S. M. Sze, J. Electrochem. Soc. **149**, F81 (2002).

[4.39]D. Shamiryan, M. R. Baklanov, S. Vanhaelemeersch, and K. Maex, J. Vac. Sci. Technol. B **20**, 1923 (2002).

Chapter 5:

[5.1]L. M. Ephrath and E. J. Petrillo, J. Electrochem. Soc. **129**, 2282 (1982).

[5.2]M. Kojima, H. Kato and M. Gatto, J. Appl. Phys. **75**, 7507 (1994).

[5.3]O. Joubert, G. S. Oehrlein and Y. Zhang, J. Vac. Sci. Technol. A **12**, 658 (1994).

[5.4]G. S. Oehrlein and H. L. Williams, J. Appl. Phys. **62**, 662 (1987).

[5.5]G. S. Oehrlein and Y. H. Lee, J. Vac. Sci. Technol. A **5**, 1585 (1987).

[5.6]G. S. Oehrlein, K. K. Chan and M. A. Jaso, J. Appl. Phys. **64**, 2399 (1988).

[5.7]G. S. Oehrlein, Y. Zhang, D. Vender and M. Haverlag, J. Vac. Sci. Technol. A **12**, 323 (1994).

[5.8]T. E. F. M. Standaert, M. Schaepkens, N. R. Rueger, P. G. M. Sebel, G. S. Oehrlein, and J. M. Cook, J. Vac. Sci. Technol. A **16**, 239 (1998).

[5.9]X. Hua, X. Wang, D. Fuentevilla, G. S. Oehrlein, F. G. Celii, and K. H. R. Kirmse, J. Vac. Sci. Technol. A **21**, 1708 (2003).

[5.10]K. Takahashi, M. Hori, S. Kishimoto, and T. Goto, Jpn. J. Appl. Phys., Part 1 **33**, 4181 (1994).

[5.11]P. Jiang, F. G. Celii, W. W. Dostalik, K. J. Newton, and H. Sakima, J. Vac. Sci. Technol. A. **19**, 1388 (2001).

[5.12]S. C. McNevin and M. Cerullo, J. Vac. Sci. Technol. A **15**, 659 (1997).

[5.13]K. Kubota, H. Matsumoto, S. Shingubara, H. Shindo, and Y. Horiike, Jpn. J. Appl. Phys., Part 1 **34**, 2119 (1995).

[5.14]K. Takahashi, M. Hori, S. Kishimoto, and T. Goto, Jpn. J. Appl. Phys. **33**, 4181 (1994).

[5.15]A. Sankaran and M. J. Kushner, J. Appl. Phys. **97**, No. 023307 (2005).

[5.16]A. Sankaran and M. J. Kushner, J. Vac. Sci. Technol. A **22**, 1242 (2004).

[5.17]A. Sankaran and M. J. Kushner, J. Vac. Sci. Technol. A **22**, 1260 (2004).

[5.18]A. Sankaran and M. J. Kushner, App. Phys. Lett. **82**, 1824 (2003).

[5.19]D. Zhang and M. J. Kushner, J. Vac. Sci. Technol. A **18**, 2661 (2000).

[5.20]D. Zhang and M. J. Kushner, J. Vac. Sci. Technol. A **19**, 524 (2001).

[5.21]K. Williams, I. Martin and E. Fisher, J. Am. Soc. Mass Spectrum **13**, 518 (2002).

[5.22]I. Martin and E. Fisher, J. Vac. Sci. Technol. A **22**, 2168 (2004).

[5.23]C. Abrams and D. Graves, J. Vac. Sci. Technol. A **19**, 175 (2001).

[5.24]G. Cunge and J. P. Booth, J. Appl. Phys. **85**, 3953 (1999).

[5.25]J. P. Booth, G. Cunge and P. Chabert, J. Appl. Phys. **85**, 3097 (1999).

[5.26]D. Gray, V. Mohindra and H. Sawin, J. Vac. Sci. Technol. A **12**, 354 (1994).

[5.27]Li Ling, X. Hua, L. Zheng, G.S. Oehrlein, E. A. Hudson, and P. Jiang, manuscript in preparation, J. Vac. Sci. Technol. (2006).

[5.28]S. J. Fonash, J. Electrochem. Soc., **137**, 3885 (1990).

[5.29]Y. Wnag, S. W. Graham, L. Chan, and S. Loong, J. Electrochem. Soc., **144**, 1552 (1997).

[5.30]R. d'Agostino, F. Cramarossa, F. Fracassi, and F. Illuzzi, *Plasma Deposition, Treatment and Etching of Polymers*, (Academic, San Diego, 1990).

[5.31]S. Agraharam, D. Hess, P. Kohl, and S. Allen, J. Vac. Sci. Technol. A **17**, 3265 (1999).

[5.32]C. B. Labelle, K. K. S. Lau, and K. K. Gleason, Mater. Res. Soc. Symp. Proc. **511**, 75 (1998).

[5.33]J. W. Coburn and H. F. Winters, J. Vac. Sci. Technol. A **16**, 391 (1979).

[5.34]X. Li, X. Hua, L. Ling, G. S. Oehrlein, M. Barela, and H. M. Anderson, J. Vac. Sci. Technol. A **20**, 2052 (2002).

Chapter 6:

[6.1]C. B. Labelle and K. K. Gleason, J. Vac. Sci. Technol. A **17**, 445 (1999).

[6.2]M. Walker, K. M. Baumgartner, M. Kaiser, S. Lindenmaier, and E. Rauchle, Surf. Coat. Technol. **97**, 291 (1997).

[6.3]E. P. J. M. Everaert, H. C. van der Mei, and H. J. Busscher, Colloids Surf. B **10**, 179 (1998).

[6.4]N. Inagaki, S. Tasaka and Y. Takami, J. Appl. Polym. Sci. **41**, 965 (1990).

[6.5]G. S. Oehrlein, Y. Zhang, D. Vender, and M. Haverlag, J. Vac. Sci. Technol. A **12**, 323 (1994).

[6.6]A. J. Bariya, C. W. Frank and J. P. McVittie, J. Electrochem. Soc. **137**, 2575 (1990).

[6.7]M. Inayoshi, M. Ito, M. Hori, T. Goto, and M. Hiramatsu, J. Vac. Sci. Technol. A **16**, 233 (1998).

[6.8]S. Arai, K. Tsujimoto and S. Tachi, Jpn. J. Appl. Phys., Part 1 **31**, 2011 (1992).

[6.9]M. Schaepkens, G. S. Oehrlein and J. M. Cook, J. Vac. Sci. Technol. B **18**, 848 (2000).

[6.10]S. Samukawa, Jpn. J. Appl. Phys., Part 1 **33**, 2133 (1994).

[6.11]D. Zhang and M. J. Kushner, J. Vac. Sci. Technol. A **18**, 2661 (2000).

[6.12]D. Zhang and M. J. Kushner, J. Vac. Sci. Technol. A **19**, 524 (2001).

[6.13]J. P. Booth, G. Cunge and P. Chabert, J. Appl. Phys. **85**, 3097 (1999).

[6.14]C. Butoi, N. Mackie, K. Williams, N. Capps, and E. Fisher, J. Vac. Sci. Technol. A **18**, 2685 (2000).

[6.15]D. Gray, V. Mohindra and H. Sawin, J. Vac. Sci. Technol. A **12**, 354 (1994).

[6.16]K. Takahashi and K. Tachibana, J. Vac. Sci. Technol. A **19**, 2055 (2001).

[6.17]S. Samukawa, Jpn. J. Appl. Phys., Part 1 **33**, 2133 (1994).

[6.18]K. Kubota, H. Matsumoto, S. Shingubara, H. Shindo, and Y. Horiike, Jpn. J. Appl. Phys., Part 1 **34**, 13 (1995).

[6.19]K. Takahashi, M. Hori, M. Inayoshi, and T. Goto, Jpn. J. Appl. Phys., Part 1 **35**, 3635 (1996).

[6.20]G. Cunge and J. P. Booth, J. Appl. Phys., **85**, 3952 (1999).

[6.21]M. Nakamura, M. Hori, T. Goto, M. Ito, and N. Ishii, J. Vac. Sci. Technol. B **19**, 2134 (2001).

[6.22]M. Kitamura, H. Akiya and T. Urisu, J. Vac. Sci. Technol. B **7**, 14 (1989).

[6.23]P. Favia, G. Cicala, A. Milella, F. Palumbo, P. Rossini, and R. D'Agostino, Surf. Coat. Technol. **169**, 609 (2003).

[6.24]G. Cicala, A. Milella, F. Palumbo, P. Favia, and R. D'Agostino, Diamond Relat. Mater. **12**, 2020 (2003).

[6.25]A. Milella, F. Palumbo, P. Favia, C. Cicala, and R. D'Agostino, Pure Appl. Chem. **77**, 399 (2005).

[6.26]L. Zheng, L. Ling, X. Hua, and G. S. Oehrlein, J. Vac. Sci. Technol. **23**, 634 (2005).

[6.27]Li Ling, X. Hua, L. Zheng, G.S. Oehrlein, E. A. Hudson, and P. Jiang, manuscript in preparation, J. Vac. Sci. Technol. (2006).

[6.28]T. E. F. M. Standaert, M. scharpkens, N. R. Rueger, P. Sebel, G. S. Oehrlein, and J. M. Cook, J. Vac. Sci. Technol. A **16**, 239 (1998).

[6.29]J. H. Keller, J. C. Forster and M. S. Barnes, J. Vac. Sci. Technol. A **11**, 2487 (1993).

[6.30]X. Li, X. Hua, L. Ling, G. S. Oehrlein, M. Barela, and H. M. Anderson, J. Vac. Sci. Technol. A **20**, 2052 (2002).

[6.31]X. Li, L. Ling, X. Hua, M. Fukasawa, G. S. Oehrlein, M. Barela, and H. M. Anderson, J. Vac. Sci. Technol. A **21**, 284 (2003).

[6.32]X. Li, L. Ling, X. Hua, G. S. Oehrlein, Y. Wang, and H. M. Anderson, J. Vac. Sci. Technol. A **21**, 1955 (2003).

[6.33]A. Vasenkov, X. Li, G. S. Oehrlein, and M. J. Kushner, J. Vac. Sci. Technol. A **22**, 511 (2004).

[6.34]S. Agraharam, D. Hess, P. Kohl, and S. Allen, J. Vac. Sci. Technol. A **17**, 3265 (1999).

[6.35]C. B. Labelle, K. K. S. Lau, and K. K. Gleason, Mater. Res. Soc. Symp. Proc. **511**, 75 (1998).

[6.36]R. d'Agostino, F. Cramarossa, F. Fracassi, and F. Illuzzi, *Plasma Deposition, Treatment and Etching of Polymers,* (Academic, San Diego, 1990).

[6.37]A. Keudell and W. Moller, J. Appl. Phys. **75**, 7718 (1994).

[6.38]A. Keudell, Thin Solid Films**75** , 7718 (1994).